Vol. 45, No. 9
September 2023

ISSN 1024-1809

METALLOPHYSICS and ADVANCED TECHNOLOGIES

МЕТАЛОФІЗИКА ТА НОВІТНІ ТЕХНОЛОГІЇ

METALLOFIZIKA I NOVEISHIE TEKHNOLOGII

Том 45, № 9 (2023)

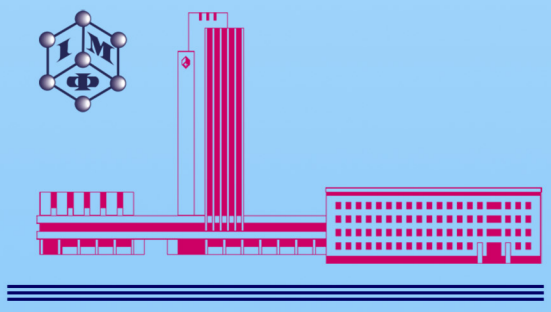

G.V. Kurdyumov Institute for Metal Physics
National Academy of Sciences of Ukraine
https://mfint.imp.kiev.ua

Засновник: Національна академія наук України, Інститут металофізики ім. Г. В. Курдюмова НАН України
Видавець: ВД «Академперіодика» НАН України

«Металофізика та новітні технології» ● 'Metallophysics and Advanced Technologies'

Щомісячний науковий журнал ● A Monthly Research Journal

NATIONAL ACADEMY OF SCIENCES OF UKRAINE ● G. V. KURDYUMOV INSTITUTE FOR METAL PHYSICS

AN INTERNATIONAL RESEARCH JOURNAL

METALLOPHYSICS AND ADVANCED TECHNOLOGIES

(Metallofizika i Noveishie Tekhnologii)

FOUNDED IN SEPTEMBER, 1979

Volume 45, No. 9; September 2023

CONTENTS

Scientific Editors of Issue—*O. S. Gatsenko, V. A. Tatarenko*
Executive Managing Editor—*O. S. Gatsenko*
Editors—*L. I. Makarenko, M. V. Manilo, I. V. Zagorulko*
The artwork for direct reproduction is made by computer group of EPD of the G. V. Kurdyumov Institute for Metal Physics, N.A.S. of Ukraine

Editorial Office Address:
G. V. Kurdyumov Institute for Metal Physics, N.A.S. of Ukraine, EPD—'MNT',
36 Academician Vernadsky Boulevard, UA-03142 Kyiv, Ukraine
Telephone: +380 44 4249042. Fax: +380 44 4242561. E-mail: mfint@imp.kiev.ua

Registration Certificate of the Publishing Subject: ДК № 5875 on 13.12.2017
State Registration Certificate of the Printed Mass Medium: КВ № 23232-13072 ПР on 23.02.2018.

Approved for publication by the Academic Council of the G. V. Kurdyumov Institute for Metal Physics of the National Academy of Sciences of Ukraine
Published in English or Ukrainian languages according to resolution of Editorial Board of the journal

Printed by Publishing House 'Akademperiodyka', of the NAS of Ukraine
4 Tereshchenkivs'ka Str., UA-01024 Kyiv, Ukraine
Registration Certificate of Publishing Subject: ДК № 544 on 27.07.2001

Journal website: http://mfint.imp.kiev.ua
Journal DOI: https://doi.org/10.15407/mfint

Issue DOI: https://doi.org/10.15407/mfint.45.09

НАЦІОНАЛЬНА АКАДЕМІЯ НАУК УКРАЇНИ ● ІНСТИТУТ МЕТАЛОФІЗИКИ ім. Г. В. Курдюмова

МЕТАЛОФІЗИКА ТА НОВІТНІ ТЕХНОЛОГІЇ

МІЖНАРОДНИЙ НАУКОВИЙ ЖУРНАЛ
ЗАСНОВАНИЙ У ВЕРЕСНІ 1979 р.

Том 45, № 9; вересень, 2023

ЗМІСТ

Наукові редактори випуску: *О. С. Гаценко, В. А. Татаренко*
Відповідальний секретар редакційної колегії *О. С. Гаценко*
Редактор-коректор *О. С. Гаценко*
Технічні редактори *І. В. Загорулько, Л. І. Макаренко, М. В. Маніло*
Художні редактори *І. В. Загорулько, Л. І. Макаренко, М. В. Маніло*
Оригінал-макет для прямого репродукування виготовлено комп'ютерною групою РВВ Інституту металофізики ім. Г. В. Курдюмова НАН України

Адреса редакції:
Інститут металофізики ім. Г. В. Курдюмова НАН України, РВВ—Редакція «МНТ»
бульв. Акад. Вернадського, 36; 03142 Київ, Україна
Тел.: +380 44 4249042; факс: +380 44 4242561
Ел. пошта: mfint@imp.kiev.ua

Свідоцтво суб'єкта видавничої справи: ДК № 5875 від 13.12.2017 р.
Свідоцтво про державну реєстрацію друкованого засобу масової інформації: КВ № 23232-13072 ПР від 23.02.2018 р.

Затверджено до друку вченою радою Інституту металофізики ім. Г. В. Курдюмова НАН України
Друкується за постановою редакційної колегії журналу англійською, або українською мовами

Підписано до друку 28.09.2023 р. Формат 70 × 100/16.
Ум. друк. арк. 8,78. Обл.-вид. арк. 8,07.
Тираж 61 пр. Зам. № 7143 від 20.12.2023 р.

Віддруковано ВД «Академперіодика» НАН України
вул. Терещенківська, 4; 01024 Київ, Україна
Свідоцтво суб'єкта видавничої справи ДК № 544 від 27.07.2001 р.

Сайт журналу: http://mfint.imp.kiev.ua
DOI (журналу): https://doi.org/10.15407/mfint
DOI (випуску): https://doi.org/10.15407/mfint.45.09

INFORMATION (GUIDELINES) FOR CONTRIBUTORS

Submission of Manuscripts: Manuscripts should be sent by e-mail (mfint@imp.kiev.ua). Additionally, they can be sent by regular mail to Executive Managing Editor, Editorial Office, G. V. Kurdyumov Institute for Metal Physics, N.A.S. of Ukraine, 36 Academician Vernadsky Boulevard, UA-03142 Kyiv, Ukraine. Manuscripts may also be submitted to a member of the Editorial Advisory Board or to the appropriate Regional Editor who is familiar with the research presented.
Submission of a paper to '*Metallophysics and Advanced Technologies*' (transliteration: '*Metallofizika i Noveishie Tekhnologii*', *i.e.*, '*MfNT*') will be taken to imply that it represents original work not previously published, that it is not being considered for publication elsewhere, and that, if accepted for publication, it will not be republished without the consent of the Editors and Publisher. It is a condition of acceptance by the Editor of a manuscript for publication that the Publishers acquire automatically the copyright in the manuscript throughout the world. Journal '*MfNT*' supports the generally accepted principles described in documents on publication ethics and unacceptable practices, which are presented on the journal website.
Scope of the Journal: *Electronic Structure and Properties, Crystal-Lattice Defects, Phase Transformations, Physics of Strength and Plasticity, Metallic Surfaces and Films, Structure and Properties of Nanoscale and Mesoscopic Materials, Amorphous and Liquid States, Interactions of Radiation and Particles with Condensed Matter, Materials in Extremal Conditions, Reactor and Aerospace Metals Science, Medical Metals Science, New Metallic Materials and Synthetic Metals, Metal-Containing Smart Materials, Physical and Technical Basis of Experiment and Diagnostics, Articles under Discussion*.
Language: The language of publication may be English (preferably) or Ukrainian.
Abstract: Each paper requires an abstract of 200–250 words summarizing the significant coverage and findings (the use of mathematical symbols and expressions in abstract is not recommended).
Keywords and PACS numbers: 5–7 keywords and PACS numbers reflecting the content of the contribution should be supplied (see 'Physics and Astronomy Classification Scheme 2010').
Manuscript Preparation: Papers should be formatted according to the template, which can be downloaded from the Journal's website. The length of **research papers** should not in general exceed 5000 words and 10 figures; **review articles** should not exceed 10000 words and 30 figures, including tables and diagrams. Authors are urged to arrange the subject matter clearly under headings such as: 1. Introduction, 2. Experimental/Theoretical Details, 3. Results, 4. Discussion, 5. Conclusion, References. Subsections should be identified with section and subsection numbers (such as 6.1. Second-Value Subheading).
References and Notes: Notes are indicated in the text by consecutive superior Arabic numbers (without parentheses). References should be numbered consecutively (in square brackets) throughout the text. The full list should be collected and typed at the end of the paper in numerical order. Listed references should be completed in all details including **DOI** (if available) but excluding article titles in journals. **All authors'** initials should precede their names. Examples of references preparation:

1. S. O. Firstov and T. G. Rogul, *Metallofiz. Noveishie Tekhnol.*, **44**, No. 1: 127 (2022) (in Ukrainian). https://doi.org/10.15407/mfint.44.01.0127
2. V. B. Tarelnyk, O. P. Gaponova, and Ye. V. Konoplianchenko, *Prog. Phys. Met.*, **23**, No. 1: 27 (2022). https://doi.org/10.15407/ufm.23.01.027
3. A. Meisel, G. Leonhardt, and R. Szargan, *Röntgenspektren und Chemische Bindung* [X-Ray Spectra and Chemical Bond] (Leipzig: Akademische Verlagsgesellschaft Geest & Portig K.-G.: 1977) (in German).
4. J. M. Ziman, *Printsipy Teorii Tverdogo Tela* [Principles of the Theory of Solids] (Moscow: Mir: 1974) (Russian translation).
5. M. A. Stucke, D. M. Dimiduk, and D. M. Hazzledine, *High Temperature Ordered Intermetallic Alloys. V* (Eds. I. Baker and R. Darolia) (Pittsburgh, PA, USA: MRS: 1993), p. 471.
6. *Handbook of Mathematical Functions with Formulas, Graphs and Mathematical Tables* (Eds. M. Abramowitz and I. A. Stegun), Nat'l Bureau of Standards. Appl. Math. Ser. Vol. **55** (Washington, D.C.: U.S. Govt. Printing Office: 1964).
7. B. B. Karpovych and O. B. Borovkoff, *Proc. of Symp. 'Micromaterials Engineering' (Dec. 25–31, 1999)* (Kyiv: RVV IMF: 2000), vol. **2**, p. 113 (in Russian).
8. A. E. Krug, *Abstr. Int. Conf. Phys. Phenomena (Dec. 25–31, 1991, Alushta)* (Kharkiv: 1991), p. 12.
9. T. M. Radchenko, *Vplyv Uporyadkuvannya Defektnoyi Struktury на Transportni Vlastyvosti Zmishanykh Krystaliv* [Influence of Ordering of the Defect Structure on Transport Properties of the Mixed Crystals] (Thesis of Disser. for the Degree of Dr. Phys.-Math. Sci.) (Kyiv: G. V. Kurdyumov Institute for Metal Physics, N.A.S.U.: 2015) (in Ukrainian). https://doi.org/10.13140/RG.2.2.35430.22089

10. E. M. Gololobov, V. B. Shipilo, N. I. Sedrenok, and A. I. Dudyak, *Sposob Polucheniya Karbonitridov Metallov* [Production Method of Metal Carbonitrides], Authors' Certificate 722341 SSSR (Publ. November 21, 1979) (in Russian).
11. V. G. Trubachev, K. V. Chuistov, V. N. Gorshkov, and A. E. Perekos, *Sposob Polucheniya Metallicheskikh Poroshkov* [The Technology of Metallic Powder Production]: Patent 1639892 SU. MKI, B22 F9/02, 9/14 (Otkrytiya i Izobreteniya, **34**, No. 13: 11) (1991) (in Russian).
12. Yu. M. Koval' and V. V. Nemoshkalenko, *O Prirode Martensitnykh Prevrashcheniy* [On the Nature of Martensitic Transformations] (Kyiv: 1998) (Prepr./N.A.S. of Ukraine. Inst. for Metal Physics. No. 1, 1998) (in Russian).

Journal title abbreviations should conform to generally accepted styles:
https://www.cas.org/support/documentation/references/corejournals;
https://cdn.journals.aps.org/files/rmpguapb.pdf;
https://images.webofknowledge.com/WOK46P9/help/WOS/A_abrvjt.html;
https://mathscinet.ams.org/msnhtml/serials.pdf.

Equations and Formulae: Formulas in the text should be inserted by **MathType**, fully compatible with MS Office. Vectors should be typed in bold without arrows above. Note that complicated formulae, mathematical expressions or (de)notations are not recommended in the title, abstract, and keywords.

Tables: Number tables consecutively with Arabic numerals and give a clear descriptive caption at the top.

Figures: All figures should be numbered with consecutive Arabic numbers, have descriptive captions and be mentioned in the text. Keep figures separate at the end of the text and clearly label each figure with author's name and figure number. The labels at axis should contain the designation (or notation) of quantities and their units.

Preparation: Figures submitted must be of a high enough standard for reproduction with 300–600 dpi resolution (including half-tone illustrations). Redrawing or retouching of unusable figures will be charged to the authors.

Colour Plates: Whenever, the use of colour is an integral part of the research, or where the work is generated in colour, the Journal will publish (in paper version) the colour illustrations with charge to the author. Reprints in colour will carry a surcharge. Please write to the Publisher for details.

Submission of Electronic Text: Authors should submit the electronic version of their paper by e-mail to the Editorial Office. The text file should be saved in the native formats of the MS Word with a name consisting the name of the first author, for example, Hotovchenko.docx. The electronic form of figures (in TIF, EPS, JPG, PNG formats preferably and with name consisting the name of the first author also, for example, Hotovchenko_fig2a.jpg) should be planned so that they reduce to 12.7 cm column width (or less), and keep them separated from the text file. It is desirable to submit additionally all the **figures** within the format of the program, in which they were created.

Proofs: Contributors will receive page proofs for correction by e-mail as a PDF document. These must be returned to Kyiv office (mfint@imp.kiev.ua with subject beginning by word 'mfint') within 5 days of receipt.

Page Charges: There are no page charges to individuals or institutions.

Reprints: Authors can freely download a PDF version of their published article from journal website: https://mfint.imp.kiev.ua. The printed issues may be ordered by completing the appropriate form sent with proofs and prepaid by authors under the terms as for subscription.

Further Information: All questions arising during the **peer review** or after acceptance of manuscripts, especially those relating to reprints, should be directed to G. V. Kurdyumov Institute for Metal Physics, N.A.S. of Ukraine, Executive Managing Editor, Editorial Office, 36 Academician Vernadsky Blvd., UA-03142 Kyiv, Ukraine;
Fax: +380 44 4242561, e-mail: mfint@imp.kiev.ua (with subject beginning by word 'mfint').

We ask the authors to apply with their manuscript Copyright Transfer Agreement form.

Copyright Transfer Agreement

We, the undersigned authors of the manuscript '_____', transfer to the Founders, Publisher, and Editorial Board of the Journal 'Metallophysics and Advanced Technologies' (according to agreements between them) the right to publish this manuscript in original language or in translation to the other languages. We confirm that publication of this manuscript **will not** infringe a copyright of other persons or organizations and publication ethics.

Author(s):_____
(Last Name, First Name, Affiliation)

Correspondence Address:_____

Phone and e-mail: _____

_____ _____
(Signature) *(Date)*

ІНФОРМАЦІЯ (ПРАВИЛА) ДЛЯ АВТОРІВ

Науковий журнал «Металофізика та новітні технології» (МфНТ) щомісяця публікує статті, які раніше ще не публікувалися та не перебувають на розгляді для опублікування в інших виданнях. Статті мають містити результати експериментальних і теоретичних досліджень в області фізики та технологій металів, стопів і сполук з металічними властивостями; рецензії на монографії; інформацію про конференції, семінари; відомості з історії металофізики; рекламу нових технологій, матеріялів, приладів. Журнал дотримується загальноприйнятих принципів, зазначених на його сайті в документах з публікаційної етики та щодо неприйнятних практик.

Тематика журналу: *Електронні структура та властивості, Дефекти кристалічної ґратниці, Фазові перетворення, Фізика міцности та пластичности, Металічні поверхні та плівки, Будова та властивості наномасштабних і мезоскопічних матеріялів, Аморфний і рідкий стани, Взаємодії випромінення та частинок із конденсованою речовиною, Матеріяли в екстремальних умовах, Реакторне й авіакосмічне металознавство, Медичне металознавство, Нові металеві матеріяли та синтетичні метали, Металовмісні смарт-матеріяли, Фізико-технічні основи експерименту та діягностики, Дискусійні повідомлення*.

Статті публікуються однією з двох мов: англійською (віддається перевага) або українською.

Статті, в оформленні яких не дотримано наступних правил для опублікування в МфНТ, повертаються авторам без розгляду по суті. (Датою надходження вважається день повторного надання статті після дотримання зазначених нижче правил.)

1. Стаття має бути підписаною всіма авторами (із зазначенням їхніх адрес електронної пошти); слід вказати прізвище, ім'я та по батькові автора, з яким редакція буде вести листування, його поштову адресу, номери телефону та факсу й адресу електронної пошти.

2. Виклад матеріялу має бути чітким, **структурованим** (розділами, наприклад, «1. Вступ», «2. Експериментальна/Теоретична методика», «3. Результати та їх обговорення», «4. Висновки», «Цитована література»), стислим, без довгих преамбул, відхилень і повторів, а також без дублювання в тексті даних таблиць, рисунків і підписів до них. Анотація та розділ «Висновки» мають не дублювати один одного. Числові дані слід наводити в загальноприйнятих одиницях.

3. Об'єм оригінальної (неоглядової) статті має бути не більше 5000 слів (з урахуванням основного тексту, таблиць, підписів до рисунків, списку використаних джерел) і 10 рисунків. **Об'єм оглядової статті** — до 10000 слів та 30 рисунків.

4. За потреби до редакції може надаватися друкований (А4, подвійний інтервал) примірник рукопису з ілюстраціями.

5. До редакції обов'язково надається (по **e-mail**) файл статті, набраний у текстовому редакторі Microsoft Word, з назвою, що складається з прізвища першого автора (латиницею), наприклад, Hotovchenko.docx.

6. Електронна версія рукопису та його друкований варіянт (в разі його надання) мають бути ідентичними. Вони мають оформлюватися за шаблоном, який можна завантажити з сайту журналу, і містити 5–7 **індексів PACS** в редакції 'Physics and Astronomy Classification Scheme 2010'. Тексти статей мають також містити **назву статті**, **список авторів**, **повні назви** та **поштові адреси установ**, в яких вони працюють, **анотацію статті** (200–250 слів), **5–7 ключових слів** двома мовами (**англійською** та **українською**), а заголовки таблиць і підписи до рисунків мають подаватися **як мовою рукопису, так і англійською мовою**; англомовна анотація може бути представленою в більш розгорнутому варіянті (до 500 слів). Назва статті, її анотація та ключові слова мають не містити складні формули, математичні вирази чи позначення.

7. Електронні версії рисунків мають бути представленими у вигляді окремих файлів (у форматах TIF, EPS, JPG, PNG з розріжненням у 300–600 dpi) з назвами, що складаються з прізвища першого автора (латиницею) та номера рисунка, наприклад, Hotovchenko_fig2a.jpg. Додатково рисунки надаються у форматі програми, в якій вони створювалися.

8. Написи на рисунках (особливо на півтонових) слід по можливості замінити літерними позначеннями (набраними на контрастному фоні), а криві позначити цифрами або різними типами ліній/маркерів, які мають бути роз'ясненими в підписах до рисунків або в тексті. На графіках усі лінії/маркери мають бути достатньої товщини/розміру для якісного відтворення їх у зменшеному в 2–3 рази вигляді (рекомендована початкова ширина рисунка — 12,7 см). Світлини мають бути чіткими та контрастними, а написи та позначення мають не закривати істотні деталі (для чого можна використовувати стрілки). Замість зазначення в підтекстовці збільшення під час зйомки бажано проставити масштаб (на контрастному фоні) на одній з ідентичних світлин. На графіках підписи до осей, **виконані мовою статті**, мають містити позначення (або найменування) величин, що відкладаються вздовж осей, і відділені комою їхні одиниці вимірювання.

9. Формули в текст треба вставляти за допомогою редактора формул **MathType**, сумісного з MS Office. **Вектори** слід набирати напівтовстим шрифтом без стрілок зверху.

10. Рисунки, таблиці, формули, а також підрядкові **примітки (виноски)** мають нумеруватися поспіль по всій статті.

11. Посилання на літературні джерела слід давати у вигляді порядкового номера, надрукованого в рядок у квадратних дужках. Список цитованої літератури складається почергово за першою згадкою джерела. Приклади оформлення посилань наведено нижче (просимо звернути увагу на порядок розташування ініціалів і прізвищ авторів, бібліографічних відомостей і на розділові знаки, а також на необхідність зазначення **всіх** співавторів цитованої роботи та її ідентифікатора **DOI**, якщо він є):

1. S. O. Firstov and T. G. Rogul, *Metallofiz. Noveishie Tekhnol.*, **44**, No. 1: 127 (2022) (in Ukrainian). https://doi.org/10.15407/mfint.44.01.0127
2. V. B. Tarelnyk, O. P. Gaponova, and Ye. V. Konoplianchenko, *Prog. Phys. Met.*, **23**, No. 1: 27 (2022). https://doi.org/10.15407/ufm.23.01.027
3. A. Meisel, G. Leonhardt, and R. Szargan, *Röntgenspektren und Chemische Bindung* [X-Ray Spectra and Chemical Bond] (Leipzig: Akademische Verlagsgesellschaft Geest & Portig K.-G.: 1977) (in German).
4. J. M. Ziman, *Printsipy Teorii Tverdogo Tela* [Principles of the Theory of Solids] (Moscow: Mir: 1974) (Russian translation).
5. M. A. Stucke, D. M. Dimiduk, and D. M. Hazzledine, *High Temperature Ordered Intermetallic Alloys. V* (Eds. I. Baker and R. Darolia) (Pittsburgh, PA, USA: MRS: 1993), p. 471.
6. *Handbook of Mathematical Functions with Formulas, Graphs and Mathematical Tables* (Eds. M. Abramowitz and I. A. Stegun), Nat'l Bureau of Standards. Appl. Math. Ser. Vol. **55** (Washington, D.C.: U.S. Govt. Printing Office: 1964).
7. B. B. Karpovych and O. B. Borovkoff, *Proc. of Symp. 'Micromaterials Engineering' (Dec. 25–31, 1999)* (Kyiv: RVV IMF: 2000), vol. **2**, p. 113 (in Russian).
8. A. Eh. Krug, *Abstr. Int. Conf. Phys. Phenomena (Dec. 25–31, 1991, Alushta)* (Kharkiv: 1991), p. 12.
9. T. M. Radchenko, *Vplyv Uporyadkuvannya Defektnoyi Struktury na Transportni Vlastyvosti Zmishanykh Krystaliv* [Influence of Ordering of the Defect Structure on Transport Properties of the Mixed Crystals] (Thesis of Disser. for the Degree of Dr. Phys.-Math. Sci.) (Kyiv: G. V. Kurdyumov Institute for Metal Physics, N.A.S.U.: 2015) (in Ukrainian). https://doi.org/10.13140/RG.2.2.35430.22089
10. E. M. Gololobov, V. B. Shipilo, N. I. Sedrenok, and A. I. Dudyak, *Sposob Polucheniya Karbonitridov Metallov* [Production Method of Metal Carbonitrides], Authors' Certificate 722341 SSSR (Publ. November 21, 1979) (in Russian).
11. V. G. Trubachev, K. V. Chuistov, V. N. Gorshkov, and A. E. Perekos, *Sposob Polucheniya Metallicheskikh Poroshkov* [The Technology of Metallic Powder Production]: Patent 1639892 SU. MKI, B22 F9/02, 9/14 (Otkrytiya i Izobreteniya, **34**, No. 13: 11) (1991) (in Russian).
12. Yu. M. Koval' and V. V. Nemoshkalenko, *O Prirode Martensitnykh Prevrashcheniy* [On the Nature of Martensitic Transformations] (Kyiv: 1998) (Prepr./N.A.S. of Ukraine. Inst. for Metal Physics. No. 1, 1998) (in Russian).

Слід використовувати загальноприйняті скорочення назв журналів:
https://www.cas.org/support/documentation/references/corejournals;
https://cdn.journals.aps.org/files/rmpguapb.pdf;
https://images.webofknowledge.com/WOK46P9/help/WOS/A_abrvjt.html;
https://mathscinet.ams.org/msnhtml/serials.pdf.

Необхідною вимогою є також надання авторами додаткового списку цитованої літератури (**References**) в **латинській транслітерації** (система **BGN/PCGN**; рекомендовані транслітератори: http://www.slovnyk.ua/services/translit.php; http://ru.translit.net/?account=bgn).

Після транслітерованих назв книг, дисертацій, патентів та ін. слід у квадратних дужках наводити їхній англомовний переклад (див. приклади вище). При транслітерації статей з МфНТ слід використовувати написання П.І.Б. авторів, наведені **лише** в англомовному змісті відповідного випуску, і **офіційну** транслітеровану назву журналу (див. також першу сторінку кожної статті та сайт).

12. Коректура авторам надсилається електронною поштою у вигляді pdf-файлу після завершення етапу **рецензування**. На перевірку коректури авторам відводяться 5 робочих днів. Після закінчення зазначеного терміну стаття автоматично направляється до друку. Виправлення слід відмітити та прокоментувати в самому pdf-файлі або оформити у вигляді переліку виправлень (підписаного уповноваженим представником колективу авторів) і переслати електронною поштою на адресу редакції.

Електронний варіянт статті надсилається на e-mail: mfint@imp.kiev.ua (з темою, що починається словом 'mfint'). Друкована версія рукопису (якщо у ній є потреба) надсилається за адресою: **Інститут металофізики ім. Г. В. Курдюмова НАН України, редакція МфНТ; бульвар Акад. Вернадського, 36; 03142 Київ, Україна** або відповідному реґіональному редактору (див. сайт).

Автори можуть вільно завантажити pdf-файли опублікованих статей з сайту журналу (https://mfint.imp.kiev.ua), а також замовити друковані примірники випуску журналу зі своєю статтею, надіславши до редакції журналу **разом з коректурою відповідну заявку та квитанцію про оплату** друку необхідної кількості примірників випуску на умовах, аналогічних передплатним.

Відповідно до угод між редакцією МфНТ, засновниками та видавцем журналу, редакція вважає, що автори, надсилаючи їй рукопис статті, передають засновникам, видавцю та редколеґії право опублікувати цей рукопис мовою ориґіналу та в перекладі іншими мовами, і просить авторів відразу прикладати до рукопису «Угоду про передачу авторського права».

Угода про передачу авторського права

Ми, що нижче підписалися, автори рукопису «_____», передаємо засновникам, видавцю та редколеґії журналу «Металофізика та новітні технології» (згідно з угодами між ними) право опублікувати цей рукопис мовою ориґіналу та в перекладі іншими мовами. Ми підтверджуємо, що ця публікація **не** порушує авторського права інших осіб або організацій і принципів наукової етики. При цьому за авторами зберігаються всі інші права як власників цього рукопису.

Підписи авторів: _____ (П.І.Б., дата, адреса, тел., e-mail)

Metallophysics and Advanced Technologies
Металофіз. новітні технол.
Metallofiz. Noveishie Tekhnol.
2023, vol. 45, No. 9, pp. 1041–1066
https://doi.org/10.15407/mfint.45.09.1041
Reprints available directly from the publisher

PACS numbers: 72.80.Tm, 73.30.+y, 73.40.-c, 79.60.Jv, 79.70.+q, 81.05.U-, 81.40.Rs

Structure and Electronic Properties of Composite Hydrogenated Titanium–Thermally Expanded Graphite Before and After Vacuum Furnace Annealing

M. M. Yakymchuk[*], H. Yu. Mykhailova[*], I. Ye. Galstian[*,**], O. Yu. Gerasymov[*], T. D. Shatnii[*], M. O. Rud[*], E. G. Len[*,***]

[*]*G. V. Kurdyumov Institute for Metal Physics, N.A.S. of Ukraine, 36 Academician Vernadsky Blvd., UA-03142 Kyiv, Ukraine*
[**]*Institute for Solid State Research, Leibniz IFW Dresden, 20, Helmholtz Str. 01069 Dresden, Germany*
[***]*Kyiv Academic University, N.A.S. and M.E.S. of Ukraine, 36 Academician Vernadsky Blvd., UA-03142 Kyiv, Ukraine*

Previous studies have shown that mixture of hydrogenated Ti and thermally expanded graphite (TEG) can be used as a material for cathodes of thermo-photoemission energy converters and allows reducing significantly the temperature of the start of electron emission. In the present work, the changes in the structural state and electronic properties of nanostructured material based on hydrogenated Ti with 0.53 wt.% TEG during the vacuum annealings of it at different temperatures in a furnace are studied. By comparing the experimental and theoretical values of electrical conductivity for different densities of the powder material, it is shown that the hydrogenated Ti–TEG mixture can form a composite. The reason for this is the important role of interfaces between the components of the composite as well as the charge transfer through these interfaces. As found, the short-term increase of temperature changes significantly and irreversibly the structure of each component of the composite and its electrical conductivity, but the composite does

Corresponding author: Mykola Mykolayovych Yakymchuk
E-mail: yakimchuk_nikolai@ukr.net

Citation: M. M. Yakymchuk, H. Yu. Mykhailova, I. Ye. Galstian, O. Yu. Gerasymov, T. D. Shatnii, M. O. Rud, and E. G. Len, Structure and Electronic Properties of Composite Hydrogenated Titanium–Thermally Expanded Graphite Before and After Vacuum Furnace Annealing, *Metallofiz. Noveishie Tekhnol.*, **45**, No. 9: 1041–1066 (2023).
DOI: 10.15407/mfint.45.09.1041

not show significant irreversible changes during such heating. As shown, the long-term (1.5 h) annealing of the material in a vacuum furnace at ≅ 700 K and 900 K leads to the loss of above-mentioned thermal stability of composite. As established, the specific electroconductivity of the composite is increased after long-term vacuum annealing at a temperature of 700 K, and, when the annealing temperature is near 900 K, it is decreased compared to the previous case. According to the results of the specific electroconductivity temperature dependences' analysis, activation energies of electrokinetic phenomena in the studied material are established and, for the first time, the important role of electronic subsystem in investigated composite formation and in changes of its properties under various thermal influences is proved experimentally that is important to create 'cold' emitters of electrons.

Key words: composite material, thermally expanded graphite, hydrogenated titanium, electrical conductivity, thermal treatment, thermophotoemission energy conversion.

Попередні дослідження показали, що суміш гідроґенізованого Ti та терморозширеного графіту (ТРГ) як матеріял для катод термофотоемісійних перетворювачів енергії уможливлює істотно понизити температуру початку емісії електронів. В даній роботі досліджено зміну структурного стану й електронних властивостей наноструктурного матеріялу на основі гідроґенізованого титану з 0,53 ваг.% ТРГ за його відпалів за різних температур у вакуумній печі. Шляхом порівняння експериментальних і теоретичних значень електропровідности за різних густин порошкового матеріялу показано, що суміш гідроґенізований Ti–ТРГ може утворювати композит. Причиною цього є вагома роль інтерфейсів між складовими частинами композиту, а також перенесення заряду крізь ці інтерфейси. Встановлено, що короткочасне підвищення температури істотно та необоротньо змінює структуру кожної окремої складової композиту та її електропровідність; проте композит під час такого нагрівання не демонструє значних необоротніх змін, оскільки його структура й електрофізичні властивості є результатом одночасної дії багатьох стимульованих підвищеною температурою процесів. Показано, що тривалий відпал (упродовж 1,5 год.) матеріялу у вакуумній печі за ≅ 700 К і 900 К позбавляє даний композит вищеописаної термічної стабільности. Встановлено, що питома електропровідність композиту зростає після тривалого відпалу у вакуумі за температури у 700 К, а зі збільшенням температури відпалу до 900 К зменшується порівняно з попереднім випадком. За результатами аналізи температурних залежностей питомої електропровідности встановлено енергії активації електрокінетичних явищ у досліджуваному матеріялі та вперше експериментально доведено важливу роль електронної підсистеми в утворенні композиту та зміні його властивостей за різних термічних впливів, що важливо для створення «холодних» емітерів електронів.

Ключові слова: композитний матеріял, терморозширений графіт, гідроґенізований титан, електропровідність, термооброблення, термофотоемісійний перетворювач енергії.

(Received 11 October, 2022; in final version, 21 September, 2023)

1. INTRODUCTION

Today, the problem of alternative renewable and mobile energy sources is very acute. New challenges arising from the change of the next economic setup (already on the 6th), as well as large-scale plans for the development of space far beyond the limits of the Earth's orbits, require the development of ecological, easy-to-use and efficient energy sources. One of the ways to reduce losses and pollution in power generation is the use of direct energy converters, especially, of solar energy. Among such converters, thermionic converters (TECs), which use the thermo- and photo-stimulated effects of electron emission from cathode material (into the vacuum gap between the cathode and the anode), are still the most powerful. Less powerful thermo- and photovoltaic devices are based on the similar but internal (in the absence of a vacuum gap) effects. Until now, the main disadvantage of TECs is still the high temperature of electron emission, which entailed many technical problems that have gained prospects for solving due to the development of nanomaterials and nanotechnologies only [1–4].

The use of metal–nanocarbon composite materials for the fabrication of cathodes of thermophotoemission converters (TPECs) of radiation and thermal energy has made it possible to the significantly lower temperature, at which electron emission begins. The use of a mixture of hydrogenated titanium powder and thermally expanded graphite (TEG) for these purposes showed that under the influence of concentrated solar radiation, the TPEC becomes a source of direct current when its cathode is heated up to 170°C [5]. Similar effects have also been observed in composites of $LaNi_5$ + carbon nanotubes (CNTs) [6], in which laser-stimulated emission was realized at laser pulse energies much lower than for other types of materials.

The study of the initial mixtures of metal powders with carbon nanostructures (CNS) made it possible to establish that, for example, at low concentrations of CNTs in the hydrogenated titanium matrix, composites are formed. It has mechanical and electrical properties different from similar properties of the origin materials and their simple mixtures [7, 8]. Similar composites are also formed when thermally expanded graphite is added to hydrogenated titanium powder, but over a wider range of filler concentrations [9]. The nature of such composites is associated with the transfer of charges between their components, which can significantly affect the emission properties of the materials [3].

However, it would be incorrect to explain the decrease of the emission's start temperature by the properties of the composites in their initial state only, because, as shown by electron-microscopy studies [5, 6], under the action of concentrated solar and laser radiation, the surface of the cathodes changes significantly—mainly the carbon component of

the composite is restructured. Thus, a thin transparent carbon layers with numerous bubble-like overgrowths were formed on the surface of the metal particles of the Ti–TEG composite in the sunlight concentrator. This means that in addition to the changes in the concentrations of free electrons in the components of the composite, the 'hot' electrons in the metal particles (excited by light and heat fluxes) and the near-zero electron affinity of the mainly sp^3-hibridized carbon thin film can also contribute to the decrease of emission temperature. All of the above-mentioned factors, as well as the presence on the surface of small elements of relief with significant aspect ratio, are important for creating electron emitters with a structure and properties that will change the contributions from different emission mechanisms, for example, increase the contribution from autoelectronic emission. It should also be considered that, as the temperature increases in hydrogenated titanium, hydrogen diffusion processes are activated and the reduction of oxide film on the surface of the metal particles is began, and, on the other hand, the rate of the rate of oxidation of titanium increases in the presence of oxygen in the residual atmosphere. The emission of electrons may also depend on the number and density of contacts between the components of the composite of the same and different types, which are determined by the concentration of CNS and the degree of homogeneity and compaction of powder samples. The influence of the peculiarities of carrier transfer through numerous interfaces, both between individual components of the composite and through a thin carbon layer formed on the surface of metal particles under the influence of light and/or temperature, may also be significant.

It should be noted that the study of the influence of elevated temperatures on hydrogenated titanium powders has a separate importance for metal science, since on the air the particles of titanium powder are very quickly covered by oxide shells, which significantly change the electrophysical properties of the material. The studies of both the mentioned changes and the process of partial recovery of metal particles' properties due to thermal activation of hydrogen diffusion in the material are an important physical metallurgy task as well as the study of the addition of different types of nanostructured carbon influence on the properties of corresponding composite systems.

The diversity and competitive complexity of the processes described above require additional research, in particular, the study of changes in the structural and electronic properties of this type of composite under the influence of thermal energy fluxes. For this purpose, two series of hydrogenated Ti–TEG samples have been prepared with a concentration of 0.53 wt.% TEG, which corresponds to the filler concentration that demonstrated a low emission temperature in experiments on a solar energy concentrator [5]. The samples were annealed in a vacuum furnace at two fixed temperatures. Part of the samples was pre-compressed be-

fore annealing in the furnace, and the rest remained in the powder state. The electron-microscopy and resistometric studies were carried out on the initial and annealed samples, as well as the dependences of their specific electrical conductivity on temperature are measured.

2. OBJECTS AND EXPERIMENTAL METHODS

The composite Ti+0.53 wt.% TEG was obtained by mechanically mixing powders of hydrogenated Ti (with a hydrogen content of 2.74 wt.% (1.32 at.%)) and TEG in a 'drunk barrel' type mixer for 8 hours. A portion of the material was pressed at room temperature under a pressure of approximately 0.8 tonne/cm^2 into steel cuvettes, in which the annealing of the material took place. Powder and pressed samples were subjected to vacuum annealing in a furnace for about 1.5 h at temperatures of ≅700 K and 900 K.

Resistometric studies of powder materials were performed using the following setup. The powder sample was placed in a cylindrical capsule with the dielectric side face and compressed with a copper piston. The copper bottom of the capsule and the piston played the role of electrical contacts through which current was applied to the powder materials under study. The dependences of the electrical conductivity (σ) on the sample density (ρ) were obtained during the powder compressing by piston (loading) and further unloading.

The study of the temperature dependence of the specific electrical conductivity was carried out with the same equipment, but the powder was placed in a ceramic capsule surrounded by a heating element.

Electron microscopic studies of compacted samples were performed on a JEOL JSM-6700F SEM electron microscope with a JED-2300 energy dispersive analyser.

3. RESULTS AND DISCUSSION

3.1. Resistometric studies

The results of resistometric studies of the initial (before heat treatment) pure components and the composite based on them are presented in Fig. 1. It can be seen (Fig. 1, *a*) that the initial density of TEG is very small—$\rho = 0.198$ g/cm^3 ($\sigma = 5.1 \cdot 10^{-6}$ $(\Omega \cdot \text{cm})^{-1}$), and, even after reaching the maximum of compression achievable on this equipment, it remains smaller ($\rho = 2.041$ g/cm^3, $\sigma = 0.895$ $(\Omega \cdot \text{cm})^{-1}$) than for the initial hydrogenated Ti powder ($\rho = 2.872$ g/cm^3; Fig. 1, *b*). After reaching the maximum value of the specific electrical conductivity $\sigma = 0.950$ $(\Omega \cdot \text{cm})^{-1}$ at $\rho = 0.955$ g/cm^3, the values of the σ reach saturation (≅ 0.90 $(\Omega \cdot \text{cm})^{-1}$) and almost do not change even when the density is increased by two

times (from 0.955 to 2.041 g/cm³). At the unloading stage, there is almost no relaxation of the compressed TEG body. Subsequent loading–unloading cycles are practically not accompanied by changes in the material density and conductivity: the values of the corresponding quantities fluctuate slightly around the values recorded in the saturation region. Note that the growth of the function σ(ρ) in the compression stage is due to an increase in the total area of contacts between particles and the number of conductive channels during the compaction of the powder material. Usually, as the piston is raised and the volume filled with the powder sample increases, a relaxation of the composite occurs, which continues up to a certain density value, at which the rapid decrease in the number and area of contacts between particles ends and a sharp drop in σ occurs due to the breakdown of the electrical circuit. In the case of pure TEG, the material is compressed and remains in this state.

The initial hydrogenated titanium (below often simply denoted as Ti) powder during the first loading (Fig. 1, *b*) is significantly compacted—from $\rho = 2.161$ g/cm³ to $\rho = 3.535$ g/cm³, and its specific electrical conductivity changes from the value $\sigma = 9.38 \cdot 10^{-3}$ $(\Omega \cdot \text{cm})^{-1}$ to the maximum of 3.58 $(\Omega \cdot \text{cm})^{-1}$ at $\rho = 3.122$ g/cm³, and then reaches saturation at the level of ≅ 3.03 $(\Omega \cdot \text{cm})^{-1}$ at the maximum value of $\rho = 3.535$ g/cm³. The stress relaxation range during unloading of Ti powder is very narrow. Subsequent load–unload cycles leave the Ti powder density almost unchanged (≅ 3.68 g/cm³), but lead to a slight decrease in conductivity (to ≅ 2.2 $(\Omega \cdot \text{cm})^{-1}$). The decrease in conductivity in the saturation region and during cycling can be explained by the deformation of Ti particles and an increase in the number of defects (dislocations) in them. The obtained maximum values of specific conductivity are in full agreement with the corresponding literature values for titanium hydride powder with an oxide film on its particles [10].

For the composite sample (Fig. 1, *c*) with 0.53 wt.% TEG (33 vol.%

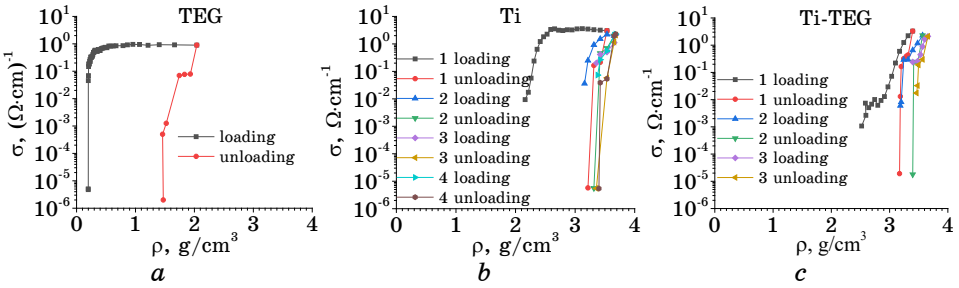

Fig. 1. Dependences of the specific electrical conductivity of pure components (*a*, *b*) and composite Ti+0.53 wt.% TEG (*c*) on the materials' density before heat treatment (for several load–unload cycles).

TEG), the density of the material before compression was $\rho = 2.521$ g/cm^3, and the specific electrical conductivity was $\sigma = 1.07 \cdot 10^{-3}$ $(\Omega \cdot \text{cm})^{-1}$. The composite conductivity reaches the level of non-compacted Ti powder ($\cong 1 \cdot 10^{-2}$ $(\Omega \cdot \text{cm})^{-1}$) at composite density value of $\cong$ 2.8 g/cm^3. Further compression of the sample leads to an increase in electrical conductivity by 2 orders of magnitude, while the maximum value of conductivity $\sigma = 3.28$ $(\Omega \cdot \text{cm})^{-1}$ is observed at the maximum value of density $\rho = 3.397$ g/cm^3 obtained in this experiment. Starting from the second load–unload cycles, the behaviour of the composite during deformation is similar to that of pure hydrogenated Ti (Fig. 1, *b*), and the value of the specific electrical conductivity after several such cycles approaches the value $\sigma = 2.11$ $(\Omega \cdot \text{cm})^{-1}$ at maximum compression, when $\rho = 3.66$ g/cm^3.

Note that the calculated average values of the density of the mixture $\rho = \rho_{TEG}\vartheta_{TEG} + \rho_{Ti}\vartheta_{Ti}$ (ϑ is the volume fraction of a given component of the mixture), both before ($\cong 1.51$ g/cm^3) and after ($\cong 3.04$ g/cm^3) partial densification that takes place during the resistometric studies, are smaller than the corresponding experimental values of the density: 2.521 and 3.397 g/cm^3. On the other hand, the conductivity of the mixture at maximum compression is greater than the corresponding conductivity values of the two pure components. This indicates both the significant influence of long-term mechanical processing (mixing) on the structure of the composite material and certain changes in the electronic structure of the composite. As a result of such processing, a decrease in the volume fraction of the carbon component of the composite is observed in the initial state, while its mass fraction remains constant (the TEG becomes less crumbly and more homogeneous). As shown the estimations based on the mass fraction of each component of the mixture unchanged during the mixing process and assumed that the density of Ti particles does not change during mixing, at the maximum compaction of the composite the density of TEG in it reaches a value of 0.41 g/cm^3, which is only $\cong 2$ times exceeds the density of pure TEG without compaction (and mixing). Thus, after compaction of the composite, TEG remains in a state far from the maximum compaction obtained during resistometric studies of pure TEG.

The above analysis of the mixing density is not enough to make any assumptions about the mixing model that would explain the electrophysical properties of the material. Next, we will limit ourselves to comparing the specific electrical conductivity data of only the first load–unload cycles of powder materials. Since the maximum conductivity of the composite is $\cong 10\%$ higher than the maximum conductivity of titanium powder, and more than 3.6 times higher than the electrical conductivity of TEG at its maximum compaction, and 5.75 times higher than the conductivity of TEG at a density of 0.41 g/cm^3, which it has in composites, it can be concluded that the material studied is

really a composite, whose properties differ both from the properties of the pure components and from the values of the corresponding values averaged for the mixture.

For further analysis, let us decide on the model of the heterogeneous system we are studying. Its natural model (see Fig. 2) is one, in which the space between Ti particles, which are compacted and provide a relatively deformation-resistant conductive skeleton of the composite, is filled by the partially compacted and conductive TEG powder, which was modified during mechanical processing. Within the framework of such a model, the decrease in the maximum value of the specific electrical conductivity of the composite during the second and subsequent load–unload cycles can be explained not only by the decrease in the conductivity of the titanium particles themselves due to the deformation-stimulated increase in the number of defects in them, but also by the additional effect of the decrease in the number of direct contacts

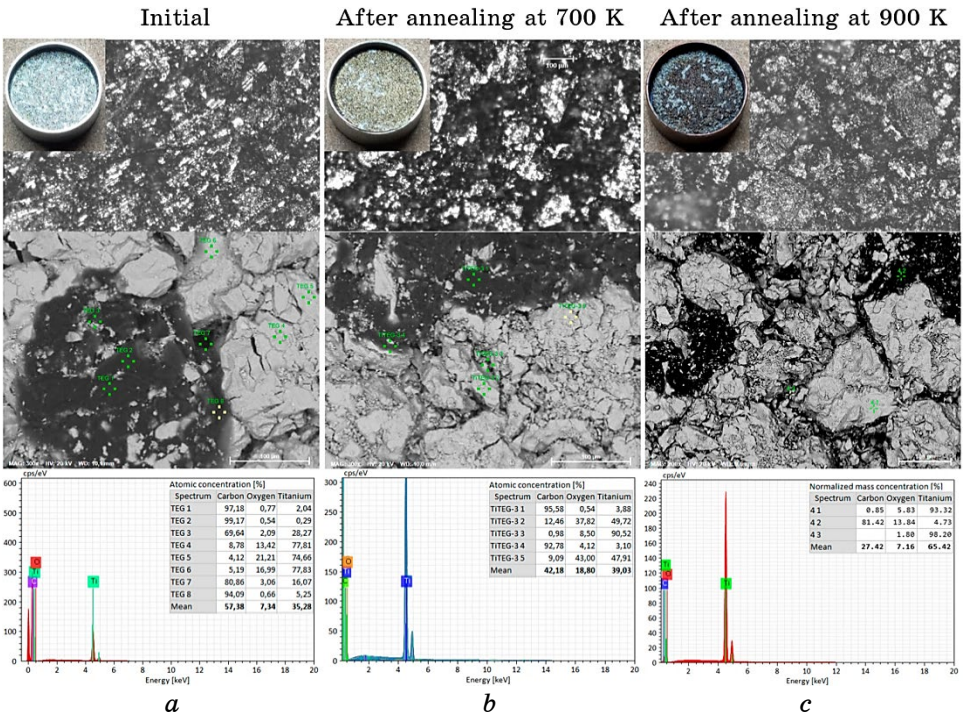

Fig. 2. Optical (top row) and SEM (middle row) images of the surface of the composite Ti+0.53 wt. % TEG after pressing under a pressure of about 0.8 tonne/cm^2 in the initial state (*a*) and after annealing at 700 K (*b*) and 900 K (*c*) for 1.5 h, as well as the corresponding results of EDX analysis (see the tables in the bottom row, the EDX spectra are shown for the points with the largest numbers).

between metal particles during cycling, which is accompanied by the destruction of some current flow channels through the relatively highly conductive titanium skeleton, as well as by the decrease in the conductivity of this channel due to the flow of free charge carriers between metal particles and carbon component of the composite.

Therefore, the material obtained is a weakly porous heterosystem, one part of whose volume is occupied by the matrix component and the other by isolated from each other particles of the second component, which, in a certain approximation, can be considered as equidistant inclusions. Since the volume fractions of the components of the mixture are comparable in values and Fig. 2 shows only the surface of the sample, from which most of the TEG was removed by the press mould during pressing, it remain undefined which material plays the role of matrix and which inclusions. Let us consider both possible options: if in the bulk of the sample, inclusions in the form of hydrogenated titanium particles (with oxide shells) are surrounded by TEG layers, and, *vice versa*, if areas filled with TEG are surrounded by a metal matrix.

In any case, within the framework of used theoretical model [11], we will replace the real approximately equidistant inclusions with different shapes by similar inclusions of cubic shape with corresponding effective mean sizes, whose centres form a simple cubic lattice in a continuous matrix phase. The work [11] also substantiates the legality of replacing a wide range of real matrix systems by the idealized one described above. Such replacing is correct if the 'piecewise-homogeneous' electrical field approximation within structural parts of the composite is satisfied. This supposition is equivalent to the Lorentz's assumption concerning the approximate compensation of reactive fields acting on the selected particle of inclusion from other particles from the Lorentz's sphere, when the dielectric permeability of the composite is calculated as one of the type of generalized conductivity of the heterogeneous environment. Then, for such material, it is possible to calculate the generalized conductivity (in our case specific electrical conductivity) according to the formulas of the work [11]. In the case of a three-dimensional isotropic matrix heterostructure, we have:

$$\sigma = \sigma_0 \left(1 + \frac{\vartheta_1}{\vartheta_0 / 3 + \sigma_0 / (\sigma_1 - \sigma_0)} \right), \qquad (1)$$

where $\vartheta_0 = 1 - \vartheta_1$ is the volume fraction of the matrix, ϑ_1 is the volume concentration of the inclusions, σ is the specific electrical conductivity of the system, the index 0 denotes the properties of the matrix material and the index 1 denotes the properties of the inclusions' material.

Since formula (1) is only suitable for materials with negligible porosity, in our case, it can only be used for samples that have already been subjected to maximum densification during resistometric stud-

ies. If TEG is chosen as the matrix, three calculation options are possible: 1—$\vartheta_0 = 0.33$ (initial value) and, as values of $\sigma_{0,1}$, the values for the maximally compacted pure components of the composite are taken from Figs. 1, *a* and *b*, respectively; 2—$\vartheta_0 = 0.041$ (estimate of TEG volume fraction after mixing) and $\sigma_{0,1}$ remain the same; 3—$\vartheta_0 = 0.041$, but the value of σ_1 for the most compacted pure Ti powder is taken from Fig. 1, *b*, and $\sigma_0 = 0.57$ $(\Omega\cdot\text{cm})^{-1}$ is taken from Fig. 1, *a* and for the value of density of TEG (0.408 g/cm^3), which corresponds to the selected value of ϑ_0. In the case, when the role of the matrix is played by titanium, the indices 0 and 1 in the given values are changed places.

The specific electrical conductivity of the composite under maximum compression is, as noted earlier, 3.28 $(\Omega\cdot\text{cm})^{-1}$. In the three cases mentioned above, the values of σ more closest to this value are given by calculations with a matrix of titanium particles: 1—2.2, 2—2.91, 3—2.88 $(\Omega\cdot\text{cm})^{-1}$ (for comparison, for a matrix with TEG: 1—2.02, 2—2.87, 3—2.78 $(\Omega\cdot\text{cm})^{-1}$). Firstly, this indicates that the matrix material in such heterosystem is most likely to be hydrogenated Ti and the TEG particles play a role of inclusions (which is also correlated with Fig. 2). Secondly, the assumptions [11], which underpin Eq. (1), regarding the insignificance of the influence of contact phenomena and linear and point defects on the specific electrical conductivity of the heterosystem, are violated in the case of the studied mixture, and therefore, it does not fall under the definition of a simple mixture. Thus, this is another argument in favour of the fact that the studied material is a composite.

In the studied heterosystem, the effects caused by the interfaces between particles of the same and different components of the composite, the deformation of these particles (their defect state), as well as the sizes of conducting clusters form particles of the same and different types, which determine the paths of current flow through such systems, become governing. If we assume that the dominant effect is the flow of free charge carriers across the interfaces between components with different chemical potentials, then, using formula (1), it is possible to estimate what conductivity, for example, the carbon component of the composite would have, assuming that the conductivity of the metal component would not change: $\sigma_1 \cong 17$ $(\Omega\cdot\text{cm})^{-1}$. Depending on value of σ_1, which is being compared—cases 3 or 1, 2—the flow of charges between the components corresponds to an increase in the conductivity of TEG (at $\vartheta_1 = 0.041$) of 19 or 30 times. Of course, in a real system, there is more than one factor. However, the tens-fold change in the conductivity of TEG mechanically processed to the state of multilayer graphene (see Fig. 2, *c*) can be easily explained within the framework of a simplified model. It is known that, in such quasi-two-dimensional system, the Fermi level lies in the region of the quasi-gap on the density of electronic states, and even a small change in the electron concentration can lead to a significant change in the density of

electronic states at the Fermi level, which also determines the electrical conductivity of the system. In addition, the high mobility due to the Dirac-like character of such carriers also contributes to the rapid growth of the electrical conductivity of the graphene-like system.

It should be noted that a change in the electrical conductivity of the composite due to its metal component can be significant, for which a decrease in the electron concentration (due to the flow of charges on the TEG) can be accompanied by a significant shift of the Fermi level in the energy spectrum of electrons. The latter can lead to a change in the value of the density of electronic states at the Fermi level, and thus to a change in the electrical conductivity of the metal component and the composite as a whole. This problem is also discussed in the Ref. [14].

The previous studies [5] have shown that the effect of low-temperature thermophotoelectronic emission is observed on a sample of hydrogenated Ti with 0.53 wt.% TEG previously treated during a long-term annealing in a solar energy concentrator. Therefore, one of the goals of this study was to investigate the changes in the structure and electronic properties of the same composite material during different heat treatments, in our case, in a vacuum furnace.

The studied material was annealed in a vacuum furnace at temperatures of ≅ 700 K and 900 K for 1.5 hours. After annealing at ≅ 700 K in the first load–unload cycle, a decrease in the density of the transition to the conductive state is observed (Fig. 3, *a*): at $\rho = 1.68$ g/cm^3 with the value of the specific electrical conductivity $\sigma = 1.44 \cdot 10^{-2}$ $(\Omega \cdot \text{cm})^{-1}$, which is almost 15 times higher than that of the unannealed sample (Fig. 1, *c*). During further densification (up to $\rho = 2.732$ g/cm^3), a relatively smooth increase in electrical conductivity is observed up to the maximum value of $\sigma = 13.35$ $(\Omega \cdot \text{cm})^{-1}$, which is 4 times greater than

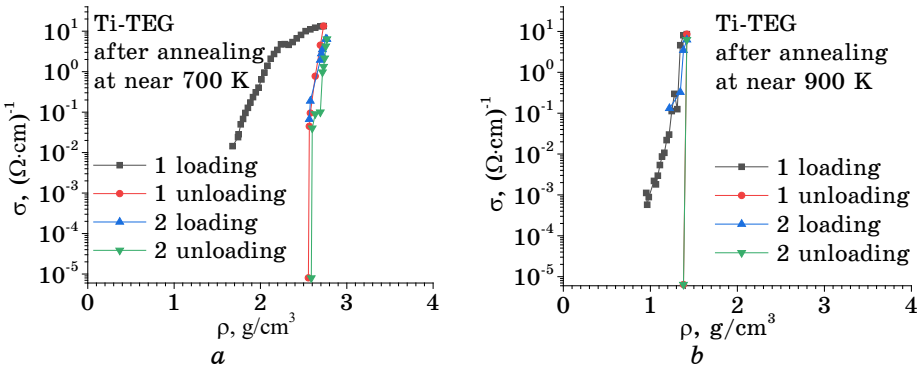

Fig. 3. Dependences of the specific electrical conductivity of the Ti+0.53 wt.% TEG composite on the density after annealing in a vacuum furnace for 1.5 h at temperatures around 700 K (*a*) and 900 K (*b*) for two loading–unloading cycles.

that of the initial sample.

After annealing at ≅ 900 K (Fig. 3, *b*), the density of the transition to the conductive state also decreases: to 0.96 g/cm^3 with the value of the specific electrical conductivity $\sigma = 5.75 \cdot 10^{-4}$ $(\Omega \cdot \text{cm})^{-1}$. Subsequent loading (up to $\rho = 1.42$ g/cm^3) leads to a sharp increase in electrical conductivity to a maximum value of $\sigma = 8.56$ $(\Omega \cdot \text{cm})^{-1}$, which is 2.6 times higher than that of the initial sample, but 36% lower than that of the sample annealed in a vacuum furnace at ≅ 700 K. The last indicates some degradation of the composite material during long-term high temperature vacuum annealing (higher than the temperature at which TEG destruction begins). In addition, as can be seen in Fig. 2, as the vacuum annealing temperature increases, sintering of the hydrogenated titanium particles occurs, but without a significant change in the morphology of the surface of the sample, as happened during concentrated sunlight annealing, when a thin carbon layer with icicle-like growths formed on the surface of the titanium particles [5]. Therefore, vacuum annealing does not provide the surface properties of the composite necessary for use in TECs, but it does allow a better understanding of the processes that occur during the formation of the composite and under various thermal influences on it.

For the annealed samples in powder state, as for the initial sample, starting from the first loading–unloading cycle, the almost complete absence of the elastic component in the dependence of the specific electrical conductivity on the density is characteristic (see Fig. 1, *c* and Fig. 3), *i.e.*, after the first compaction of the powder material, the shape of the sample is practically not restored. The resulting weakly compressed material begins to behave during the next load–unload cycle as an elastic, almost incompressible medium, which reaches slightly lower maximum values of specific electrical conductivity: for annealing at 700 K, 6.36 $(\Omega \cdot \text{cm})^{-1}$, and for annealing at 900 K, 6.26 $(\Omega \cdot \text{cm})^{-1}$. For a case of annealing at 700 K, corresponding value is obtained at a slightly higher density of 2.77 g/cm^3 compared to the first cycle of loading–unloading, and for a case of annealing at 900 K—with the same density value of 1.42 g/cm^3 as on the first cycle. As the annealing temperature increases from room temperature (no annealing) to 900 K, the same values of electrical conductivity are obtained at lower densities of the powder composite and in a smaller range of ρ values. The decrease in the density of the composites after annealing (Table 1) and the range of its change in Fig. 3 can be explained by the processes of destruction of TEG, sintering of metal particles, as well as partial stratification of the powder material during the vacuum annealing, which leads to an increase in the volume fraction of TEG (due to its loosening) in the composite. The decrease in the maximum values of the specific electrical conductivity of the annealed powder samples during the second loading–unloading cycle can be explained by a better

TABLE 1. Electrophysical characteristics of composite samples Ti+0.53 wt.% TEG before and after annealing for 1.5 h at different temperatures in a vacuum furnace (resistometric data are given for the first load–unload cycle).

Annealing temperature, K	ρ_{cr}, g/cm^3	$\sigma_{\rho_{cr}}$, $(\Omega\cdot cm)^{-1}$	$\rho_{\sigma_{max}}$, g/cm^3	σ_{max}, $(\Omega\cdot cm)^{-1}$
Without annealing	2.52	0.001	3.39	3.28
700	1.67	0.014	2.73	13.35
900	0.95	0.001	1.41	8.56

filling of the cavities between the titanium particles with thermally expanded graphite during the material compaction at both loading–unloading cycles, *i.e.*, by a decrease in the number of contacts between the metal particles.

The higher, in comparison with the initial (unannealed) state, values of σ in Fig. 3 (see also the values of σ_{max} in Table 1) are, probably, due to the annealing of gas impurities and a change in the chemical composition of the surface of the metal particles. The last changes in hydrogenated titanium during long-term vacuum annealing are associated with the release of hydrogen to the metal particles' surface and partial reduction of titanium oxide in the oxide shells of the metal particles. A decrease in the thickness of the oxide layer is reflected in the EDX analysis data as a decrease in the oxygen concentration on the surface of the metal particles with increasing annealing temperature (see the tables in Fig. 2 for the points of maximum titanium content). It should be noted that, for a more wide range of annealing temperatures, resistometric studies also could provide information on the thickness of the oxide layer and the diffusion coefficient of impurities in metal particles [12]. In addition, it can be seen from Table 1 that, at annealing temperature of 900 K, the value of σ_{max} decreases compared to the case of annealing at 700 K, which is also caused by the additional destruction of the TEG and the composite material in whole. The decrease in its density associated with the destruction of the composite is also confirmed by the changes depending on the vacuum annealing temperature in the values of the density ρ_{cr} of the powder material and the electrical conductivity $\sigma_{\rho_{cr}}$ (Table 1), which correspond to the points of beginning of the current flow through the composite. The transfer of charge between TEG and metal particles can also lead to additional loosening of the TEG due to Coulomb repulsion between similarly charged particles.

3.2. Temperature Dependence of Specific Electrical Conductivity

Additional information about the composite material can be obtained

by analysing the temperature dependence of the specific electrical conductivity of the composite itself and its pure components. The previously unannealed samples were heated and cooled twice; the range of temperatures investigated was approximately 280–835 K. It can be seen in Fig. 4 that all the dependences presented show an increase in the specific electrical conductivity with increasing temperature in almost all parts of corresponding curves. Thus, both the pure components and the composite itself mainly exhibit the semiconductor temperature dependence of the specific electrical conductivity, which has an activation character (see also Ref. [13]). There may be several types of charge carriers simultaneously in the material, which can be activated during the temperature growing. Each of them is characterized by its own activation energy E_g. For each temperature range, where $k_B T \cong E_g$, the activation energy determines the exponential dependence of the specific electrical conductivity:

$$\sigma(T) = \sigma_0 \exp(-E_g/(k_B T)). \qquad (2)$$

For a semiconductor $E_g = E_b/2$, where E_b is the width of the energy gap separating the corresponding electronic (hole) states from the conduction (valence) band. In particular, this type of $\sigma(T)$ dependence confirms the oxide shell model of hydrogenated titanium particles (see also [14]) and the semi-metallic character of the carbon component.

From the dependences of the specific electrical conductivity in a logarithmic scale on the inverse temperature for the unannealed composite in a vacuum furnace, one can see (Fig. 5) that the processes of thermal activation of each type of charge carriers correspond to their own linear section of the function $\sigma(1/T)$. The tangent of the inclination angle of this function is directly proportional to the activation energy E_g. At the same time, at relatively low temperatures, small slopes of the linear sections of the function $\sigma(1/T)$ are observed in all dependences, and at higher temperatures the slopes increase, which indicates

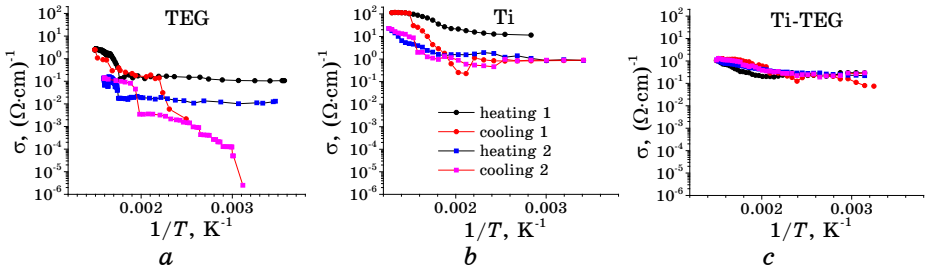

Fig. 4. Temperature dependences of the specific electrical conductivity of the initial powders of the pure components (*a*, *b*) and their mixture (*c*) during two heating–cooling cycles.

the thermal excitation firstly of carriers from low energy levels, and then of carriers that have to overcome some higher energy barriers (see Table 2). With a further increase in temperature, carriers from most of the impurity energy levels are excited and replenish the population of band ones. For the last, the role of thermal dissipation of charge carriers begins to grow, which determines the output of specific electrical conductivity values at saturation with a tendency to transition to metallic temperature dependence.

In the initial components, charge carriers with low (< 0.1 eV) activation energy are most likely associated with their excitation from impurity levels in the oxide shell of titanium particles (for example, oxygen vacancies can be donors [15]) and from the lower part of the π zone of the graphene layers of TEG to the upper one (*i.e.*, in the energy region above the Fermi level, the position of which in TEG particles is determined by the thickness and degree of deformation of their graphene layers, the type and number of adsorbates on them, *etc.*). The nature of these carriers remains the same in the composite. Although, due to the differences in the processes taking place in the composite during heating and cooling, for both heating–cooling cycles, in the cooling sections at low temperatures, a transition from the semiconductor type of temperature dependence of the specific electrical conductivity of the composite to the metallic one is observed when the temperature decreases. Moreover, at higher temperatures, the rather larger activation energy values (up to 0.19 eV) are observed, which probably correspond to the excitation of low-energy polaron states in the oxide shells of titanium particles [15]. There is practically no activation of the intrinsic carriers in titanium oxide, since the band gap for them is in-

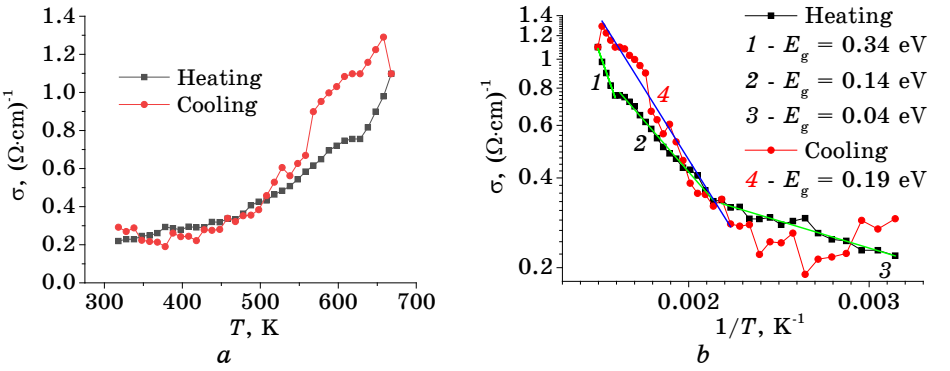

Fig. 5. Temperature dependences of the specific electrical conductivity of the initial composite Ti+0.53 wt.% TEG on the second heating–cooling cycle in linear (as a function of T) (*a*) and logarithmic (as a function of $1/T$) (*b*) scales. The activation energies of the charge carriers are given for the numbered parts of the temperature dependences.

TABLE 2. Activation energies E_g of charge carriers in the initial samples (before vacuum annealing) of the pure powder components and the Ti+0.53 wt.% composite itself. % TEG, determined from the temperature dependence of the specific electrical conductivity on two heating–cooling cycles (see Fig. 5).

Material		Activation energy, eV								
		TEG			Ti			Ti–TEG		
Type of carriers		1	2	3	1	2	3	1	2	3
Cycle 1	Heating	0.44	–	0.04	0.47	–	0.08	0.32	–	0.06
	Cooling	0.42	0.28	–	0.64	–	0.09	–	0.19	–
Cycle 2	Heating	0.4	–	0.03	0.57	–	0.04	0.34	0.14	0.04
	Cooling	–	0.23	–	0.41	–	0.07	–	0.19	–

surmountable (3.05 eV).

Mechanical processing of the mixture increases the number of defects and leads to a decrease in the activation energy. It should be noted that the α-phase of titanium is characterized by features of the electronic structure, thanks to which this metal is included in the list of potential topological materials [16]. At even higher temperatures, even 'pure' titanium can exhibit an increase in electrical conductivity with increasing temperature, which is explained in [13] by the presence in it, as a transition metal, of several energy zones with significantly different effective masses (s–p and d) of electrons and the possibility of their band-to-band transitions. At the same time, for strongly localized d-electrons, the semiconducting temperature dependence of their concentration near the Fermi level with a certain value of the activation energy ($E_g \cong 0.2$–0.5 eV) of electron transitions from d-band states to s–p-band states (in terms of Ref. [13] from the states of the second Brillouin zone to the conduction band) (Table 2).

In Figure 4, all graphs are on the same scale, and one can directly see the differences in the absolute values of the specific electrical conductivity of the pure components and of the composite before their vacuum annealing. The characteristic slopes of individual parts of the dependence $\sigma(1/T)$ can be seen in Fig. 5, *b* on a logarithmic scale. In Figure 5, it is also given the activation energies of certain charge carriers connected with the widths of the corresponding band gaps or the energies of the interband transitions.

A significant decrease in the absolute values of the electrical conductivity of the pure initial components of the composite during the second heating–cooling cycle, compared to the first cycle, draws attention. It can be explained by the rather high temperatures of our research and the changes in the chemical composition and defects of the materials at these temperatures. Thus, during the first heating–cooling cycle, a significant amount of adsorbed gases is removed from

the TEG, which decreases the number of free charge carriers and shifts the Fermi level closer to the minimum value of the energy dependence of the density of electronic states of graphite, leading to a decrease in the number of electrons around the Fermi level and, therefore, in the electrical conductivity. Even the presence of such quasi-gap in the energy spectrum of graphite is the reason for its relatively low conductivity in the temperature range from room temperature to 1300 K. The first heating of hydrogenated titanium powder in air to temperatures of about 500 K leads to the beginning of decomposition of titanium hydride and partial recovery of the oxide shells of metal particles by hydrogen (due to hydrogen diffusion from bulk to surface). This is manifested in a faster growth of electrical conductivity at the corresponding temperatures. However, with the oxide reduction process, the reverse process—oxidation—also accelerates with increasing temperature. When they compensate each other at temperatures $\geq$ 700 K, the dependence $\sigma(1/T)$ almost reaches saturation.

When the powder is cooled to temperatures $\leq$ 700 K, the release of hydrogen in the sample slows down significantly, and the oxidation process remains quite intense (the concentration of oxygen in the air does not decrease with time), so, the thickness of the oxide shell of the metal particles increases, and the conductivity of the sample decreases to values at which the second heating–cooling cycle begins. At the same time, the hydrogen-depleted sample does not return to the previous high values of electrical conductivity—the new maximum value of its conductivity will be several times lower. During the second cycle, hydrogen atoms do not have time to reach the surface and leave the particle through a thicker oxide shell (taking oxygen atoms with them) during a relatively short stay at high temperatures, and therefore, no sharp change in conductivity is observed during cooling.

At the same time, the nature of both impurity and 'band' free carriers remains unchanged in the pure materials considered. Therefore, the slopes of the dependences $\sigma(1/T)$ for different heating–cooling cycles remain unchanged, as well as the values of the activation energies. From heating–cooling cycle to next one, only the occupation of impurity levels decreases and/or the thickness of the semiconductor layer increases, which leads to the shifting of the $\sigma(1/T)$ curves to the region of lower values of electrical conductivity.

The dependences of the specific electrical conductivity of the initial powder of the hydrogenated Ti+0.53 wt.% TEG composite on the inverse temperature (Fig. 4, *c*) demonstrate mainly an increase in $\sigma(1/T)$ with increasing T, except the first heating and the second cooling, when at low temperatures a decrease in electrical conductivity is observed with increasing of values of T. Note that, for samples annealed in a vacuum furnace, a metallic type of conductivity can be observed even at low temperatures (Figs. 7 and 9). In such parts of the $\sigma(1/T)$

dependence, the determination of the activation energy E_g values loses a sense. The samples were heated from room temperature to ≤ 670 K.

Compared to the similar dependences of $\sigma(1/T)$ (on a logarithmic scale) for the initial pure components, the dependence of $\sigma(1/T)$ for the unannealed composite sample is almost independent of the number of cycles and the heating or cooling stages. This can to mean that in the composite, the processes that determined the behaviour of its pure components at different heating and cooling stages are either suppressed or compensated. One probably scenario is that TEG degassing begins in the composite upon heating, but the Fermi level shift due to the change in electron concentration leads to the flow of free charge carriers across the interfaces between TEG and Ti. If, at the same time, the electron concentration changes in hydrogenated Ti, then, this can complicate the process of hydrogen reduction of the oxide shells of metal particles.

Thus, the change of electron concentration in TEG because of desorption of gases compensates due to charges' transfer from the titanium particles, which blocks significant changes in the chemical composition of surface of the grains of powder. Therefore, when the studied composite is heated and cooled, the structural changes of the interfaces between its individual components and changes in the electronic structure of last will not be sharply effect on composites' kinetic properties. Such thermal stability of the composite (before annealing in a vacuum furnace) allows tracing the mechanisms of activation of charge carriers in it in a more or less pure form based on the dependences of $\sigma(1/T)$.

During heating and cooling of the initial composite Ti+0.53 wt.% TEG, the temperature dependence of the specific electrical conductivity in the range of its semiconducting behaviour has an exponential character with a break at 620 K (see Fig. 4, *c* and Fig. 5). At the same time, the $\sigma(1/T)$ curves show a slight difference between the heating and cooling regions compared to similar curves for pure components: at high temperatures, the dependence of $\sigma(1/T)$ is some higher in the cooling region than in the heating one. In addition, it can be seen that during the second heating, $\sigma(1/T)$ is mostly some higher than during the first one, and the opposite behaviour is observed during the cooling.

In Figure 5, *a*, the dependences of $\sigma(T)$ of the composite on the second heating–cooling cycle are shown, and Fig. 5, *b* shows the corresponding plots of the $\sigma(1/T)$ dependences. The activation of new excitation processes of charge-carrying quasi-particles is indicated by breaks in the $\sigma(1/T)$ dependence. It can be seen that the thermal energy k_BT in section *3* is sufficient to activate only charge carriers with a small energy $E_g = 0.04$ eV, which can correspond to the excitation of electrons into free states of the π zone of the TEG through a point (or

an energy quasi-gap of very small width) with almost zero density of electronic states in the energy spectrum of electrons of the semi metallic TEG. At higher temperatures (sections *2* and *4*), the quasi-particles from impurity levels with $E_g = 0.14–0.19$ eV start to be excited (for example, the binding energy of the donor electron is $E = 13.6(m^*/m_0)/\varepsilon^2 \cong$ $\cong 0.02–0.09$ eV, effective electron mass $m^* = 1.1–4.3m_0$, relative permittivity $\varepsilon \cong 80$, m_0 is electron rest mass [15, 17, 18]). Higher temperatures involve 'intrinsic' charge carriers in the kinetic phenomena. However, their energy, which is of $\cong 0.34$ eV (section *1*), corresponds only to the excitation of *d*-electrons in Ti [13], and for the activation of the intrinsic electronic states of Ti oxide, it would be necessary to overcome an order of magnitude higher energy gap.

The temperature dependences of the specific electrical conductivity was also studied for the composite Ti+0.53 wt.% TEG with initial hydrogen content in titanium of 2.74 wt.%, when the sample was previously annealed for 1.5 h in a vacuum furnace at temperatures of $\cong$ 700 K and 900 K. Plots of the electrical conductivity versus temperature are presented in Figs. 6–9 and Table 3 for 3 degrees of compression of each of the powder samples.

As for the unannealed Ti+0.53 wt.% TEG composite, the temperature dependences of the specific electrical conductivity during heating and cooling for samples annealed at $\cong$ 700 K and 900 K are mainly semiconducting (exponential) in nature with the breaks of the curves around 500 K (Fig. 7) and 550 K (Fig. 9), respectively. At the same time, the $\sigma(T)$ curves (Fig. 6) show a certain difference between the heating and cooling stages, namely, the $\sigma(T)$ dependences in the cooling stages are mostly higher than in the heating ones, but their slope (see Fig. 7, *a*) changes very little. It can also be seen that with each consecutive (second and third) heating–cooling cycle, which is also accompanied by subsequent compression of the material, the $\sigma(T)$ dependencies pass higher and higher.

The effects described above are similar to those observed on the unannealed composite sample, but now they are significantly enhanced by both the additional compression and the previous annealing. The last removed more impurities from the carbon component and a certain amount of hydrogen from the titanium particles. During the Ti-particles' dehydration, the average thickness of their oxide layers is decreased. Thus, in the annealed sample, the effect of compensating the change in conductivity of different components of the composite is much less pronounced. At the same time, the least compacted powder after annealing in a vacuum furnace (this is the first heating when taking $\sigma(T)$ dependence) showed conductivity values $\cong$ 2 times lower than that of the unannealed sample, and the most compact powder (this is the third heating, when obtaining $\sigma(T)$) showed conductivity values $\cong$ 2 times higher than that of the unannealed sample.

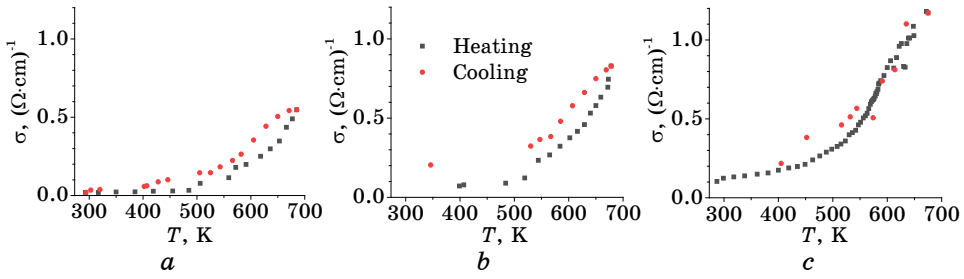

Fig. 6. Temperature dependences of the specific electrical conductivity of the composite material Ti+0.53 wt.% TEG after pre-annealing in vacuum at a temperature of ≅ 700 K for different compressions determined by the material density ρ: 1.60 g/cm^3 (*a*), 1.63 g/cm^3 (*b*), 1.65 g/cm^3 (*c*).

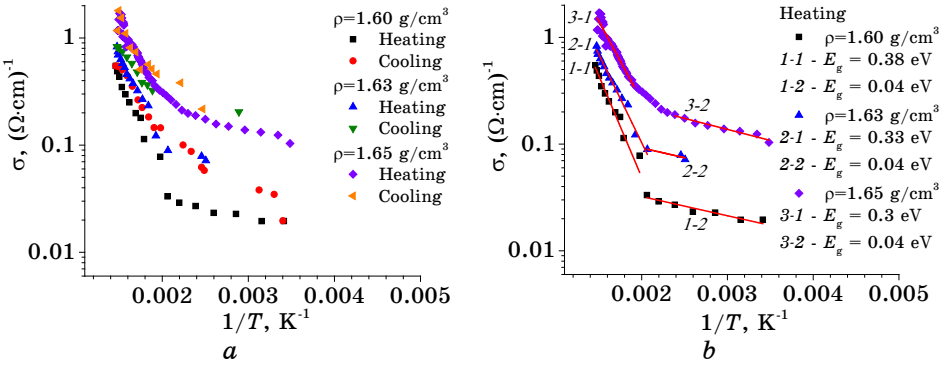

Fig. 7. Temperature dependences of the specific electrical conductivity of the composite material Ti+0.53 wt.% TEG after pre-annealing in vacuum at a temperature of ≅ 700 K in the logarithmic scale and as a function of $1/T$ for different densities: *a*—heating and cooling stages, *b*—activation energies of the free charge carriers during the heating stage.

The electronic properties of the composite material of the sample annealed in a vacuum furnace, which are determined by the temperature dependence of the electrical conductivity, remain the same as for the unannealed sample. Thus, the values of the activation energies of the free carriers are practically the same in both cases, as shown by the fitting of the curves of the dependences of the electrical conductivity on the temperature (see Figs. 5 and 7). However, Figure 7 also allows us to follow the growth patterns of the specific electrical conductivity with increasing material density at all the temperatures studied, which is in full agreement with the resistometric studies described above (Figs. 1 and 3).

At the same time, a decrease in the activation energy of the interband transitions in titanium is clearly observed during densification

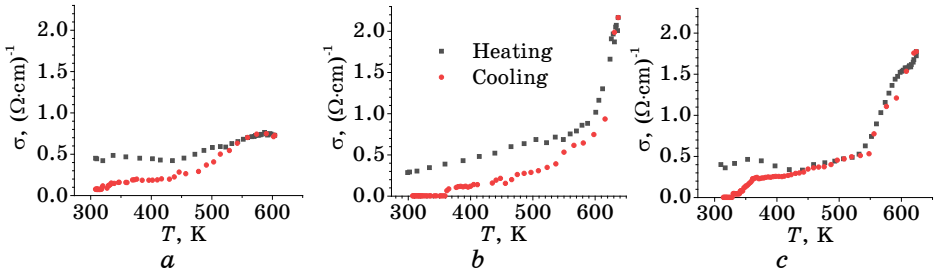

Fig. 8. Temperature dependences of the specific electrical conductivity of the composite material Ti+0.53 wt.% TEG after pre-annealing in vacuum at a temperature of ≅ 900 K for different compressions determined by the material density ρ: 1.47 g/cm^3 (*a*), 1.50 g/cm^3 (*b*), 1.58 g/cm^3 (*c*).

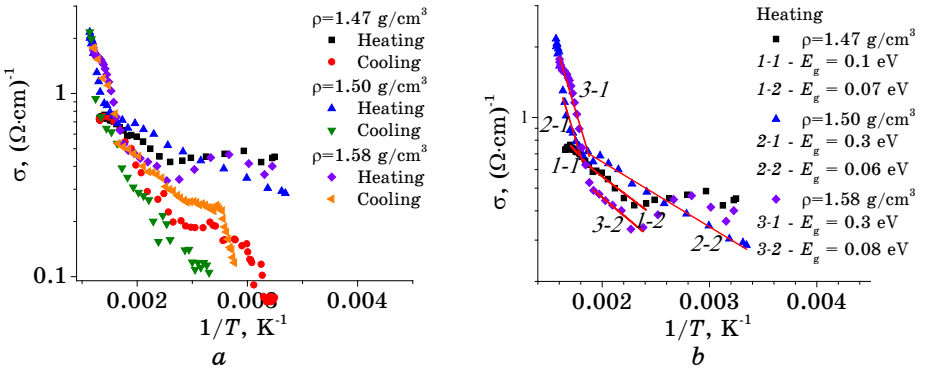

Fig. 9. Temperature dependences of the specific electrical conductivity of the composite material Ti+0.53 wt.% TEG after pre-annealing in vacuum at a temperature of ≅ 900 K in the logarithmic scale and as a function of $1/T$ for different degrees of compression: *a*—heating and cooling stages, *b*—activation energies of the free charge carriers during the heating stage.

(see the value of E_g for the sections *1–1*, *2–1*, *3–1* of the dependences $\sigma(1/T)$ in Fig. 7, *b*) and the practical invariance of the energy gaps for impurity levels (see the value of E_g for the sections *1–2*, *2–2*, *3–2* of the dependences $\sigma(1/T)$). This indicates, on the one hand, the different nature of the corresponding activation energies and, on the other hand, it proves that when the composite is compressed, not only its structural properties (which we tried to consider with Eq. (1)) but also its electronic structure (mainly the filling of different zones of both components of the composite) change. Therefore, the above-described mechanisms of influence of the corresponding interfaces between the components of the composite material, in particular, the charge transfer through them, receive experimental confirmation.

The electron microscopy and EDX studies of samples before and af-

TABLE 3. Activation energies E_g of charge carriers in composite samples Ti+0.53 wt.% TEG after annealing in vacuum for 1.5 h at different temperatures, determined from the temperature dependences of the specific electrical conductivity (Figs. 7 and 9) for three heating–cooling cycles at three different densities.

Ti–TEG		Activation energy, eV			
		Annealing at 700 K		Annealing at 900 K	
Type of carriers		1	2	1	2
Cycle 1	Heating	0.38	0.04	0.1	0.07
	Cooling	0.25	0.06	0.2	0.04
Cycle 2	Heating	0.33	0.04	0.3	0.06
	Cooling	0.21	0.04	0.26	0.11
Cycle 3	Heating	0.3	0.04	0.3	0.08
	Cooling	0.27	0.1	0.39	0.09

ter annealing at 700 K and 900 K show (Fig. 2) that annealing in a vacuum furnace leads to a change in both the surface morphology and its chemical composition. Unfortunately, annealing in a vacuum furnace does not provide the formation of the nanostructures necessary to reduce the temperature of emission onset [5]. However, it allows a better understanding of the behaviour of composite systems under conditions of elevated temperature and a determination of the upper limit of the last. Since during vacuum annealing at 700 K, the electrophysical properties (*i.e.*, specific conductivity) of the composite are improved, but, when the annealing temperature is increased to 900 K, they are deteriorated (see Table 1).

Significant changes in the structure and electronic properties of both components of the composite during annealing at 900 K are also confirmed by the data on the activation energies of band-to-band transitions in titanium and energy gaps for impurity levels (Table 3). The both mentioned characteristics begin to increase when the powder is compressed, in contrast with the annealing at 700 K, when the first characteristic is significantly larger and decreases during compression, and the second one is smaller and remains almost unchanged during compression. The reason for this is not only the destruction of the carbon component at 900 K, but also the desorption of hydrogen from hydrogenated titanium and a change in the conditions for the transfer of charge carriers between the components of the composite.

4. CONCLUSIONS

The comparison of experimental (resistometric) and theoretical values

of electrical conductivity shows that the mixture of powders of hydrogenated Ti +0.53 wt.% TEG, in which low-temperature thermophotoelectronic emission was previously observed, is a composite whose electrophysical properties differ significantly from those of an ordinary mixture and its pure components.

For the first time, it was experimentally confirmed that the reason for the formation of a composite is the significant role of the interfaces between its components. The probable mechanism of their influence through the redistribution of free charge carriers between the components was proposed.

1. It has been found that preliminary mechanical processing of the Ti–TEG mixture significantly changes the structural state of the carbon component of the composite, which becomes more homogeneous and less crumbly compared to pure TEG. It is shown that, at the maximum compression of the composite used in the experiment, its carbon component is compacted only 2 times compared to the initial (before mechanical processing) state of TEG, while pure TEG can be compacted more than 10 times.

2. It is shown that such a composite can be represented as a heterogeneous matrix system in which the particles of hydrogenated Ti plays the role of matrix and TEG particles play the role of inclusions. At the same time, it was found that for an adequate description of the experimental data, one should go beyond the limits of the used theory of the generalized conductivity of such systems and assume an increase of the specific electrical conductivity of the carbon component of the composite by 19–30 times as compared to pure TEG, which can occur due to the transfer of charges between the components and the peculiarities of the electronic structures of graphene-like materials.

3. It is shown that short-term heating in the range of 280–835 K leads to significant and irreversible changes in the structure and electronic properties of each individual component of the composite. However, in the composite, these properties do not show significant irreversible changes during such heating, since the structure and electrophysical properties of the composite are the result of the simultaneous action of many processes stimulated by elevated temperature, namely, desorption of impurities from TEG, decomposition of Ti hydride, diffusion of hydrogen throws metal particles to the surface with reduction of their oxide shells, those rapid oxidation during experiments in air, transfer of charges between components of the composite, *etc*. The result of their joint action is the stabilization of the electrophysical properties of the composite material under the influence of temperature.

4. It was found that the preliminary annealing of the composite material for 1.5 hours in a vacuum furnace at a temperature of about 700 K leads to the removal of impurities from the TEG and the release of hydrogen from the Ti particles, due to which the thickness of the oxide

layer in the last is decreased. All this disrupts the balance of the above-mentioned processes and leads to the loss of thermal stability of the composite electrophysical properties. A similar annealing at ≅ 900 K leads to the degradation of the composite material due to the onset of destruction of TEG, which is reflected in a decrease in the specific electrical conductivity of the sample. In addition, as the vacuum annealing temperature increases, sintering of the hydrogenated titanium particles occurs, but without a significant change in the surface morphology of the sample, as was the case during concentrated sunlight annealing, when a thin layer of carbon with icicle-like growths formed on the surface of the titanium particles. Therefore, vacuum annealing does not provide the surface properties of the composite required for use in TPECs, but it does provide a better understanding of the processes that occur during composite formation and under various thermal influences on it.

5. Based on the results of the analysis of the temperature dependence of the specific electrical conductivity, its semiconducting nature was established, as well as the activation energy of electrokinetic phenomena in the studied material before and after its long-term annealing in vacuum at temperatures around 700 K, which have a dual nature: at low temperatures, the excitation of free charge carriers from impurity levels prevails, and at higher temperatures, band-to-band transitions in the titanium are activated.

6. Analysis of the dependence of the activation energies on the degree of compression of the material under study after long-term annealing in vacuum at a temperature of about 700 K demonstrated, for the first time, the electronic nature of the formation of the composite and provided indirect experimental confirmation of the importance of the role of the interfaces between the different components of the composite and the transfer of charges through them, which is important for the creation of electrons' emitters with a structure and electronic properties that can change the contributions from different emission mechanisms, for example, increase the contribution from autoelectronic emission.

7. It was found that the electrophysical properties of the composite improve after annealing in vacuum at a temperature of about 700 K, and, when the annealing temperature is increased to 900 K, they deteriorate compared to the case of annealing at 700 K due to the degradation and removal of the carbon component at a higher annealing temperature, dehydration of hydrogenated titanium and changes in the conditions of transfer of charge carriers between the components of the composite.

8. It is shown that the Ti–TEG mechanical mixture demonstrates a significant transformation of the electronic structure during the formation of the composite material and its following thermal treat-

ments, which opens the way to lower the operating temperature of thermal emission devices and expand their scope of application.

ACKNOWLEDGMENTS

This work was supported by projects Nos. 0118U000416 and 0123U102275 of the National Academy of Sciences of Ukraine, and partially by UKRAPRO scholarship program for Ukrainian researchers (Volkswagen Foundation).

REFERENCES

1. K. A. Abdul Khalid, T. J. Leong, and K. Mohamed, *IEEE Transactions on Electron Devices*, **63**, No. 6: 2231 (2016).
2. M. F. Campbell, T. J. Celenza, F. Schmitt, J. W. Schwede, and I. Bargatin, *Advanced Science*, **8**, No. 9: 2003812 (2021).
3. O. C. Olawole, D. K. De, S. O. Oyedepo, O. F. Olawole, and E. S. Joel, *Current Science*, **118**, No. 4: 543 (2020).
4. M. C. James, F. Fogarty, R. Zulkharnay, N. A. Fox, and P. W. May, *Carbon*, **171**: 532 (2021).
5. I. Ye. Galstian, E. G. Len, E. A. Tsapko, H. Yu. Mykhaylova, V. Yu. Koda, M. O. Rud, M. Ya. Shevchenko, V. I. Patoka, M. M. Yakymchuk, G. O. Frolov, *Metallofiz. Noveishie Tekhnol.*, **42**, No. 4: 451 (2020).
6. I. M. Sydorchenko, N. A. Shevchenko, Ye. A. Tsapko, I. Ye. Galstan, H. Yu. Mykhaylova, and E. G. Len, *Metallofiz. Noveishie Tekhnol.*, **43**, No. 12: 1707 (2021).
7. H. Yu. Mykhaylova, E. G. Len, I. Ye. Galstyan, E. A. Tsapko, O. Yu. Gerasymov, V. I. Patoka, I. M. Sidorchenko, and M. M. Yakymchuk, *Metallofiz. Noveishie Tekhnol.*, **42**, No. 4: 575 (2020).
8. H. Yu. Mykhailova, *Visn. Nac. Akad. Nauk Ukr.*, No. 5: 54 (2021).
9. H. Yu. Mykhailova, E. G. Len, M. M. Yakymchuk, V. A. Dekhtyarenko, I. Ye. Galstian, M. Ya. Shevchenko, O. Yu. Gerasymov, E. A. Tsapko, V. I. Patoka, and M. O. Rud, *Metallofiz. Noveishie Tekhnol.*, **44**, No. 11: 1523 (2022).
10. M. V. Tsarev, V. V. Mokrushin, A. V. Stengach, I. K. Kremzukov, D. G. Ivanov, Issledovaniye Protsessa Okisleniya Poroshka Gidrida Titana Metodom Kontrolya Yego Elektricheskogo Soprotivleniya, *Materialy Konferentsii 'Vzaimodeystvie Izotopov Vodoroda s Konstruktsionnymi Materialami—HISM 08'* (2008), p. 197–201.
11. V. I. Odelevskiy, *Zhurnal Tekhnicheskoy Fiziki*, **21**, Iss. 6: 667 (1951).
12. V. V. Mokrushin and M. V. Tsarev, *International Journal of Self-Propagating High-Temperature Synthesis*, **16**, No. 2: 96 (2007).
13. Eh. A. Bel'skaya and Ye. Yu. Kulyamina, *Teplofizika Vysokikh Temperatur*, **45**, No. 6: 862 (2007).
14. I. Galstian, H. Yu. Mykhailova, and E. G. Len, *The Effect of Hydrogen Content on Electrophysical Properties of Hydrogenated Titanium–Thermally Expanded Graphite Composites, 06 July 2023, PREPRINT*.

15. V. P. Zhukov and E. V. Chulkov, *Physics of the Solid State*, **56**: 1302 (2014).
16. M. G. Vergniory, L. Elcoro, C. Felser, N. Regnault, B. A. Bernevig, and Z. Wang, *Nature*, **566**: 480 (2019).
17. C. Persson and A. Ferreira da Silva, *Appl. Phys. Lett.*, **86**: 231912 (2005).
18. D. V. Gritsenko, S. S. Shaĭmeev, V. V. Atuchin, T. I. Grigor'eva, L. D. Pokrovskiĭ, O. P. Pchelyakov, V. A. Gritsenko, A. L. Aseev, and V. G. Lifshits, *Physics of the Solid State*, **48**: 224 (2006).

Metallophysics and Advanced Technologies
Металофіз. новітні технол.
Metallofiz. Noveishie Tekhnol.
2023, vol. 45, No. 9, pp. 1067–1082
https://doi.org/10.15407/mfint.45.09.1067
Reprints available directly from the publisher

PACS numbers: 71.15.Mb, 71.20.Ps, 75.50.Ee, 78.20.Fm, 78.20.Ls, 78.70.Dm, 81.05.Zx

Electronic Structure and X-Ray Magnetic Circular Dichroism in *A*-Site Ordered Perovskite $CaCo_3V_4O_{12}$

D. V. Mazur*, L. V. Bekenov*, B. Kh. Zhuravlov*, S. V. Mokliak*, Yu. M. Kucherenko*, and V. M. Antonov*,**

**G. V. Kurdyumov Institute for Metal Physics, NAS of Ukraine,*
36 Academician Vernadsky Blvd.,
UA-03142 Kyiv, Ukraine
***Max-Planck-Institut für Festkörperforschung,*
1 Heisenbergstr.,
D-70569 Stuttgart, Germany

We are studied the electronic and magnetic properties of the *A*-site ordered perovskite $CaCo_3V_4O_{12}$ within the density-functional theory using the generalized gradient approximation (GGA) with the consideration of strong Coulomb correlations (GGA + *U*) in the framework of the fully relativistic spin-polarized Dirac linear muffin-tin orbital method of band-structure calculation. The x-ray absorption spectra and x-ray magnetic circular dichroism at the Ca, Co, and V *K*-edges are investigated theoretically. The effect of the electric quadrupole E_2 transitions and magnetic dipole M_1 transitions are analysed. The calculated results are in good agreement with experimental data.

Key words: electronic band structure, magnetic moment, GGA, x-ray absorption spectra, x-ray magnetic circular dichroism, double perovskites.

Електронні та магнетні властивості впорядкованого за *A*-позицією перовськіту $CaCo_3V_4O_{12}$ досліджено в рамках теорії функціоналу густини з використанням узагальненого ґрадієнтного наближення з урахуванням сильних Кулонових кореляцій (GGA + *U*) у рамках повністю релятивістського спін-поляризованого Діракового ЛМТО-методу розрахунку зонної структури. Теоретично досліджено Рентґенові спектри поглинання та Рентґенів магнетний циркулярний дихроїзм на Ca-, Co- та V-*K*-краях.

Corresponding author: Dmytro Viktorovych Mazur
E-mail: mazur.dm.v@gmail.com

Citation: D. V. Mazur, L. V. Bekenov, B. Kh. Zhuravlov, S. V. Mokliak, Yu. M. Kucherenko, and V. M. Antonov, Electronic Structure and X-Ray Magnetic Circular Dichroism in *A*-Site Ordered Perovskite $CaCo_3V_4O_{12}$, *Metallofiz. Noveishie Tekhnol.*, **45**, No. 9: 1067–1082 (2023). DOI: 10.15407/mfint.45.09.1067

Проаналізовано вплив електричних квадрупольних E_2-переходів і магнетних дипольних M_1-переходів. Результати розрахунків добре узгоджуються з експериментальними даними.

Ключові слова: електронна зонна структура, магнетний момент, узагальнена ґрадієнтна апроксимація, спектри поглинання Рентґенових променів, Рентґенів магнетний циркулярний дихроїзм, подвійні перовськіти.

(Received 1 September, 2023; in final version, 22 September, 2023)

1. INTRODUCTION

Transition-metal perovskites have been studied for half a century, and most intensively during the last decade, for their fascinating electronic and magnetic properties arising from narrow 3*d* bands and strong Coulomb correlations [1–5]. Perovskite-structure oxides with the general formula ABO_3 display a large variety of intriguing properties and raise lots of important fundamental issues in solid-state physics and chemistry. The structure can be described as a framework of corner-sharing BO_6 octahedra that has an *A*-site cavity formed by twelve coordinated oxygen ions. The smaller *B*-site cations have octahedral coordination by the O anions. The octahedra share corners to form a three-dimensional network, while the larger *A*-site cations sit in the 12-co-ordinate cubooctahedral cavities within this network. Perovskites display a wide range of properties including superconductivity (*e.g.*, $Ba_{1-x}K_xBiO_3$), colossal magnetoresistance (*e.g.*, $La_{1-x}Ca_xMnO_3$), itinerant electron ferromagnetism (*e.g.*, $SrRuO_3$), multiferroic behaviour (*e.g.*, $TbMnO_3$), ferroelectricity (*e.g.*, $BaTiO_3$), piezoelectricity (*e.g.*, $PbZr_{1-x}Ti_xO_3$), and ionic conductivity (*e.g.*, $La_{0.67-x}Li_{3-x}TiO_3$, $BaCeO_{3-x}$). Perovskites arguably represent the most important family of complex oxides. Distortions from the ideal perovskite structure can significantly influence the physical properties. Octahedral tilting distortions, which are present in 80–90% of all perovskites, occur when the *A*-site cation is too small for the cubooctahedral cavities [6, 7]. The octahedral tilting distortions alter the conduction bandwidth [8] and the strength of the magnetic super-exchange interactions [9]. As such, they provide a mechanism for fine-tuning the electrical, magnetic and optical properties.

More sophisticated double perovskites, *e.g.*, those that are called '*A*-site ordered' with the general formula $A(A')_3B_4O_{12}$, comprise one more site (*A*′) for cations with unusual two-dimensional square oxygen coordination. The *A*-site ordered perovskite-structure oxides $A(A')_3B_4O_{12}$ can be obtained by filling 3/4 of the *A*-sites with small transition-metal cations and the other 1/4 with larger alkali, alkaline earth, or rare earth cations. They have a $2a\times2a\times2a$ structure stabilized by heavy tilted BO_6 octahedra and consequently forming $A'O_4$ square-planar units. Cu and Mn are typical transition-metal cations readily accommodated

by the A' site. Compounds with this structure type were synthesized in the 1960s and 1970s [10, 11], and recently lots of fascinating functional properties have been discovered in this class of compounds. Among them are a large dielectric constant in $CaCu_3Ti_4O_{12}$ [12], a large negative thermal-expansion-like volume change due to interstitial charge transfer in $LaCu_3Fe_4O_{12}$ [13], and multiferroism in $CaMn_3Mn_4O_{12}$ [14]. New A-site ordered perovskites with novel properties have been attracted much attention recently [15]. These perovskites not only have the B–B interaction (or B–O–B interaction *via* oxygen ions) largely responsible for the properties of simple perovskites but also have interactions between the transition-metal ions at the A' sites (A'–A' interaction) and between those at the A' and B sites (A'–B interaction).

Among different families of the A-site ordered $A(A')_3B_4O_{12}$ double perovskites, the most studied to date are compounds with B = Fe because of their nontrivial magnetic properties and charge disproportionation reactions, which can lead to spectacular phenomena [13]. Members of other double-perovskite families, for instance, those of V-based perovskites, $A(A')_3V_4O_{12}$, also find various applications, but they are less systematically studied to date [16, 17]. Recent investigations of some vanadium compounds show that V-based perovskites may reveal rather spectacular and novel physical properties [17, 18].

$CaCo_3V_4O_{12}$ was synthesized by Ovsyannikov *et al.* [19]. It was shown that this new double perovskite possesses high-spin Co^{2+} ions in the $Im\bar{3}$ cubic symmetry. The magnetic susceptibility measured on bulk polycrystalline samples of $CaCo_3V_4O_{12}$ shows a sharp maximum around 98 K, which is a characteristic of an antiferromagnetic (AFM) ordering transition. The authors established that the Co^{2+} ions in $CaCo_3V_4O_{12}$ are in the high-spin state with a sizable orbital moment. Electrical resistivity data suggest semiconducting behaviour in the temperature range of 1.6–370 K. The chemical formula of this perovskite can be written as $Ca^{2+}Co_3^{2+}V_4^{4+}O_{12}^{2-}$. Later Ovsyannikov *et al.* investigated the structural, vibrational, magnetic, and electronic properties of the $CaCo_3V_4O_{12}$ perovskite at low temperatures and high pressure [17]. They found no apparent signatures of metallization of this perovskite up to 60 GPa. From the high-pressure thermoelectric power measurements, its electrical conduction may be described as semi-metallic and strongly compensated. By means of ambient-pressure neutron powder diffraction, the authors established that, below 100 K, $CaCo_3V_4O_{12}$ transforms into an AFM phase, in which all the magnetic moments of the Co^{2+} ions are aligned along the c-axis, and the magnetic structure has a 2-fold periodicity along this axis. They also measured the XAS at the Ca, Co, and V K-edges at 70 and 298 K.

The aim of this paper is the theoretical study from the first principles of the electronic and magnetic structures and x-ray magnetic cir-

cular dichroism in the double perovskite $CaCo_3V_4O_{12}$. The energy band structure of $CaCo_3V_4O_{12}$ is calculated within the *ab initio* approach taking into account strong electron correlations by applying a local spin-density approximation to the density functional theory supplemented by a Hubbard U term (GGA + U) [20].

The paper is organized as follows. The computational details are presented in Sec. 2. Section 3.1 presents the electronic and magnetic structures of $CaCo_3V_4O_{12}$. Section 3.2 presents the theoretically calculated XA and XMCD spectra at the Ca, Co, and V K-edges calculated in the GGA + U approximation. The theoretical results are compared with experimental measurements. Finally, the results are summarized in Sec. 4.

2. CRYSTAL STRUCTURE AND COMPUTATIONAL DETAILS

2.1. X-Ray Magnetic Circular Dichroism

Magnetooptical (MO) effects refer to various changes in the polarization state of light upon interaction with materials possessing a net magnetic moment, including rotation of the plane of linearly polarized light (Faraday or Kerr rotations), and the complementary differential absorption of left and right circularly polarized light (circular dichroism). In the near visible spectral range, these effects result from excitation of electrons in the conduction band. Near x-ray absorption edges, or resonances, the magnetooptical effects can be enhanced by transitions from well-defined atomic core levels to empty valence or conduction states.

Within the one-particle approximation, the absorption coefficient $\mu_{j\lambda}(\omega)$ for incident x-ray polarization λ and photon energy $\hbar\omega$ can be determined as the probability of electronic transitions from initial core states with the total angular momentum j to final unoccupied Bloch states:

$$\mu_{j\lambda}(\omega) = \sum_{mn\mathbf{k}} \left| \left\langle \Psi_{n\mathbf{k}} \left| \hat{\Pi}_\lambda \right| \Psi_{jm} \right\rangle \right|^2 \delta(E_{n\mathbf{k}} - E_{jm} - \hbar\omega)\theta(E_{n\mathbf{k}} - E_F)\,, \qquad (1)$$

where Ψ_{jm} and E_{jm} are the wave function and the energy of a core state with the projection of the total angular momentum m, Ψ_{nk} and E_{nk} are the wave function and the energy of a valence state in the n-th band with the wave vector $\mathbf{k}$, E_F is the Fermi energy. $\hat{\Pi}_\lambda$ is the electron–photon interaction operator in the dipole approximation:

$$\hat{\Pi}_\lambda = -e\boldsymbol{\alpha}\mathbf{a}_\lambda\,; \qquad (2)$$

here, α are the Dirac matrices and $\mathbf{a}_\lambda$ is the λ polarization unit vector of the photon vector potential with $\mathbf{a}_\perp = (1/\sqrt{2}, \pm i/\sqrt{2}, 0)$ $\mathbf{a}_\parallel = (0, 0, 1)$. Here, '+' and '–' denote, respectively, left and right circular photon polarizations with respect to the magnetization direction in the solid.

Then, x-ray magnetic circular and linear dichroism are given by $\mu_+ - \mu_-$ and $\mu_{\|} - (\mu_+ + \mu_-)/2$, respectively. More detailed expressions for the matrix elements within the electric-dipole approximation may be found in Refs. [21–23]. The matrix elements due to magnetic dipole and electric quadrupole corrections are presented in Ref. [23].

2.2. Crystal Structure

The crystal structure of $CaCo_3V_4O_{12}$ shown in Fig. 1 can be considered as a variant of the cubic perovskite oxide ABO_3. The superstructure $A(A')_3B_4O_{12}$, with space group $Im\bar{3}$ (No. 204), is formed by quadrupling the parent unit cell and replacing 3/4 of the element A with A'. Due to the introduction of A', the symmetry of the structure is lowered by a large rotation of the BO_6 octahedra, which brings four oxygen ions closer to the A'(Co) site to form a seemingly nearly square-planar environment. This particular quadruple perovskite house VO_6 octahedra, which are virtually regular: all V–O distances are identical, and the O–V–O angles deviate from 90° by only 0.04° [19]. The CoO_4 plaquettes are not so regular, with the O–Co–O angles being 93.6° and 86.4°. The V ions separated by $a/2$ lie on a simple cubic sublattice, while the Co ions lie on a b.c.c. sublattice with the same nearest-neighbour Co–Co distance. The two perovskite A and B sublattices form a CsCl configuration, making it likely that nearest-neighbour Co–V exchange interactions (*versus* Co–Co or V–V) are the driving force for the magnetic order [24]. The crystal parameters of $CaCo_3V_4O_{12}$, which are used in our

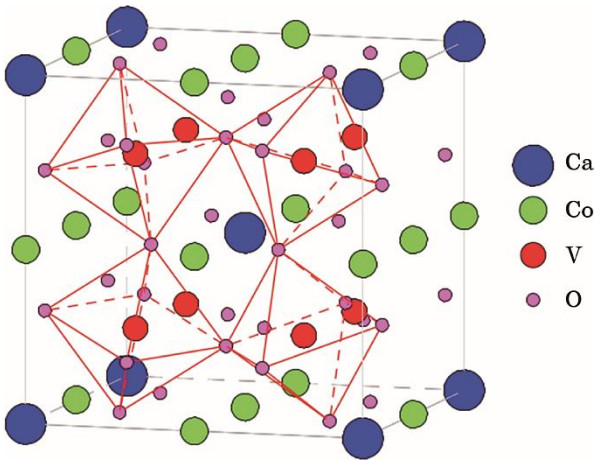

Fig. 1. The crystal structure of $CaCo_3V_4O_{12}$. There is square-planar oxygen coordination of the Co^{2+} ions occupying the A' sites and the octahedral network of V^{4+} ions. The solid lines are the unit cell boundaries.

TABLE 1. Atomic positions of $CaCo_3V_4O_{12}$ at room temperature (lattice constant $a = 7.3428$ Å [19].).

Atom	Site	x	y	z
Ca	2a	0	0	0
Co	6b	0	1/2	1/2
V	8c	1/4	1/4	1/4
O	24g	0	0.2990	0.8115

band structure calculations, are presented in Table 1.

2.3. Calculation Details

The details of the computational method are described in our previous papers [25–28], and here, we only mention several aspects. The band-structure calculations were performed using the fully relativistic linear muffin-tin orbital (LMTO) method [22, 29], which uses four-component basis functions constructed by solving the Dirac equation inside an atomic sphere [30].

The exchange-correlation functional of a GGA-type was used in the version of Perdew, Burke and Ernzerhof (PBE) [31]. The Brillouin zone (BZ) integration was performed using the improved tetrahedron method [32] and the self-consistent charge density was obtained with 1728 **k**-points in the BZ. The basis consisted of Ca, Co, and V s, p, d, and f and O s, p, and d LMTO's.

We found that the agreement between the theoretically calculated and experimentally measured XA and XMCD spectra becomes much better with taking into account strong Coulomb correlations. To include the electron–electron correlations into the consideration we used the 'relativistic' generalization of the rotationally invariant version of the LSDA + U method [33], which takes into account the spin–orbit coupling (SOC) so that the occupation matrix of localized electrons becomes non-diagonal in spin indexes.

This method is described in detail in our previous paper [33] including the procedure to calculate the screened Coulomb U and exchange J integrals, as well as the Slater integrals F^2, F^4, and F^6. In our calculations the intrashell Coulomb repulsion U and interorbital Hund's magnetic coupling J were applied to both Co and V sites: $U_{Co} = 5$ eV, $J_{Co} = 1$ eV, $U_V = 3.4$ eV, $J_V = 0.7$ eV. Similar parameters were used by Rhee and Pickett [24].

The x-ray absorption and dichroism spectra were calculated taking into account the exchange splitting of core levels. The finite lifetime of a core hole was accounted for by folding the spectra with a Lorentzian.

The widths of core levels Γ_K for Ca, Co, and V were taken from [34]. The finite experimental resolution of the spectrometer was accounted for by a Gaussian of 0.6 eV.

3. RESULTS AND DISCUSSION

3.1. Electronic Structure

Since the experimental evidence suggests the AFM order in $CaCo_3V_4O_{12}$ [19], we provide the energy band structure of this double perovskite in the AFM state with and without taking into account the SOC. The results are presented in Fig. 2. The collinear AFM $CaCo_3V_4O_{12}$ ground state within GGA (Fig. 2, *a*, *b*) as well as GGA + SOC (Fig. 2, *c*) is metallic. It is in contradiction to the electrical resistivity data, which suggest semi-conducting behaviour in the temperature range of 1.6–370 K [19].

Adding an on-site Coulomb repulsion on each of the Co and V ions

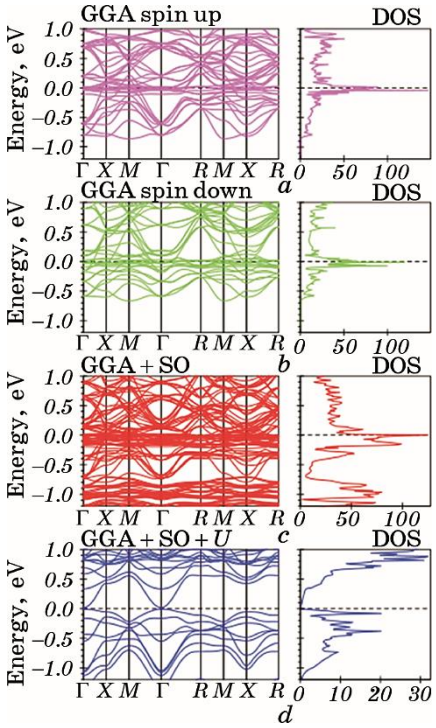

Fig. 2. The energy band structure and total density of states, in states/(cell·eV), of AFM $CaCo_3V_4O_{12}$ calculated in GGA (*a*, *b*), GGA + SOC (*c*), and GGA + SOC + *U* (*d*).

results in a Mott-isolator-type electronic structure of $CaCo_3V_4O_{12}$ (the lower panel of Fig. 2). The energy band gap is rather small and equal to 0.109 eV at the Γ symmetry point.

The crystal field at the Co sites (D_{2h} point symmetry) causes the splitting of Co 3*d* orbitals into five singlets (d_{xz}, d_{xy}, d_{yz}, d_{3z^2-1}, and $d_{x^2-y^2}$). The V site possesses the C_3 point symmetry and V 3*d* states split into one singlet *a* (the combination of d_{xz}, d_{xy}, d_{yz} orbitals) and two doublets d_{3z^2-1}, $d_{x^2-y^2}$ and the combinations of d_{xz}, d_{xy}, d_{yz}.

Both the Co^{2+} and V^{4+} ions in $CaCo_3V_4O_{12}$ are expected to be magnetic and Mott insulating, and carry a substantial orbital moment to account for the observed Curie–Weiss moments. Our calculations reveal that the Mott insulating character of the open-shell Co ions arises mostly through the d_{3z^2-1} orbital with a small amount of $d_{x^2-y^2}$ (see Fig. 3). The partial density of states (PDOS) of V ions is relatively small at the Fermi level.

The Co^{2+} ions are situated in the rectangular CoO_4 plaquettes with the electronic configuration $t_{2g}^5 e_g^2$; therefore, one would expect a large Co orbital moment. From magnetic susceptibility [19] and neutron diffraction measurements of $CaCo_3V_4O_{12}$, the authors of Ref. [17] suggest that the orbital moment at the Co site has to exceed $1\mu_B$. Our band structure calculations confirm this suggestion. We have found that the spin and orbital magnetic moments for the Co_1 ion are $m_s = 2.6062\mu_B$, $m_l = 1.2268\mu_B$, and for the Co_2 ion, they are

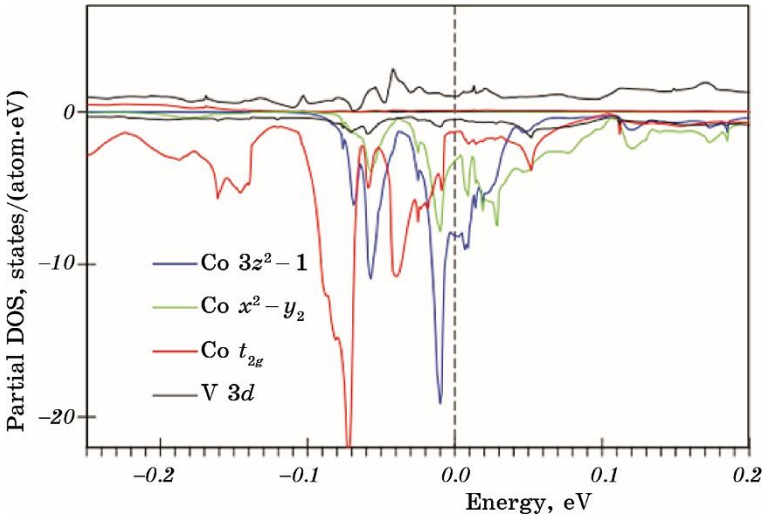

Fig. 3. The symmetry resolved partial density of states, in states/(atom·eV), of AFM $CaCo_3V_4O_{12}$ calculated in GGA.

TABLE 2. The theoretically calculated (in μ_B) spin m_s, orbital m_l, and total m_{total} magnetic moments in $CaCo_3V_4O_{12}$.

Atom	m_s	m_l	m_{total}
Ca_1	0.0086	0.0182	0.0268
Ca_2	0.0040	0.0210	0.0250
Co_1	2.6062	1.2268	3.8330
Co_2	–2.5239	–1.1888	–3.7130
V	1.0360	–0.3082	0.7278
O_1	0.0100	–0.0067	0.0033
O_2	–0.0648	–0.0082	–0.0729

$m_s = -2.5239\mu_B$ and $m_l = -1.1888\mu_B$. The spin and orbital magnetic moments at the V site are equal to $m_s = 1.0360\mu_B$ and $m_l = -0.3082\mu_B$. The Co spin and orbital moments are parallel and the ones at V are antiparallel in $CaCo_3V_4O_{12}$ in accordance with Hund's third rule.

The induced spin magnetic moments at the O_1 and O_2 sites are equal to $0.0100\mu_B$ and $-0.0648\mu_B$, respectively. The orbital magnetic moments are found to be equal to $-0.0067\mu_B$ and $-0.0082\mu_B$ for the O_1 and O_2 sites, respectively. The Ca spin and orbital magnetic moments are rather small for both sites (see Table 2).

Figure 4 presents the partial density of states for $CaCo_3V_4O_{12}$. The O 2*s* states are located mostly between –19.6 eV and –17.8 eV below E_F. The O 2*p* states are situated from –7.9 eV to –1.9 eV, however, a small amount of them appears between –1.9 eV and –1.1 eV as well as from –1.0 eV to 0 eV due to their hybridization with the Co and V 3*d* valence states, respectively. The spin splitting of the oxygen 2*p* states is quite small (around 0.2 eV). The V 3*d* states are situated from –1.2 eV to 0 eV below E_F and from 0.1 eV to 5.4 eV above E_F in the majority spin channel. The spin-down V states are mostly empty and occupy the energy interval from 0.9 eV up to 6.3 eV. There are some V 3*d* occupied states from –7.8 eV to –1.2 eV due to their hybridization with the oxygen 2*p* valence states. The spin-up Co 3*d* states are situated between –7.8 eV and –1.2 eV below E_F. There is a small peak in the close vicinity of E_F in the Co 3*d* states due to their hybridization with V 3*d* states. The Co 3*d* spin-down states occupy the energy interval from –7 eV to –1.5 eV and from 0.8 eV up to 3 eV. The Ca 3*d* empty states occupy the 6.2–8.9 eV energy interval.

3.2. X-Ray Absorption and XMCD Spectra

X-ray absorption and XMCD spectra in metals and alloys at the *K*-

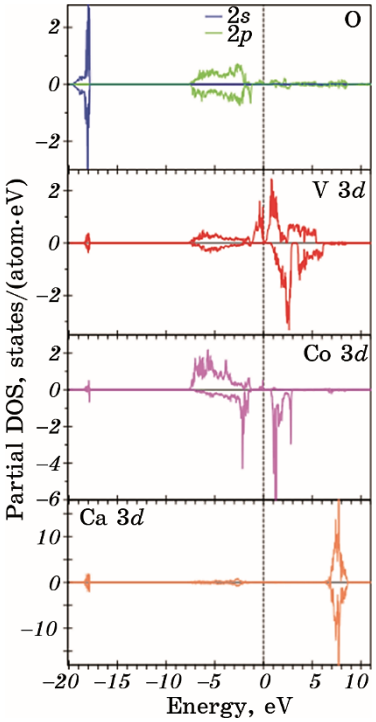

Fig. 4. The partial density of states, in states/(atom·eV), of AFM $CaCo_3V_4O_{12}$ calculated in GGA + SOC + U.

edge, when the 1s core electrons are excited to empty p states through the dipole transitions, are quite important. They are sensitive to the electronic states at neighbouring sites because of the delocalized nature of p states.

Figure 5 presents the partial 4p density of states of Ca, Co, and V ions in $CaCo_3V_4O_{12}$ above E_F calculated in the GGA + SOC + U approximation for the AFM ordering. The 4p DOS in the close vicinity of the Fermi level are quite small. The first peak of 4p DOS starts at 6.8 eV, 10.2 eV, and 12.5 eV for Co, Ca, and V, respectively. The V 4p DOS is the smallest and the one for Ca 4p is the largest. All the PDOSs are extended far above the Fermi level.

The upper panels of Figs. 6, 7 and 8 show the x-ray absorption spectra (open circles) at the Co, V, and Ca K-edges in $CaCo_3V_4O_{12}$ measured at 70 K [17] in comparison with the theoretically calculated ones (full blue lines) in the GGA + SOC + U approximation. The Co K-x-ray-absorption spectrum possesses a major peak at 7726 eV with a low energy shoulder at 7721 eV, two small high-energy shoulders at 7735 eV and 7742 eV, and a high-energy fine structure at 7778 eV (Fig. 6). The theory reproduces the energy position of the major peak and the low

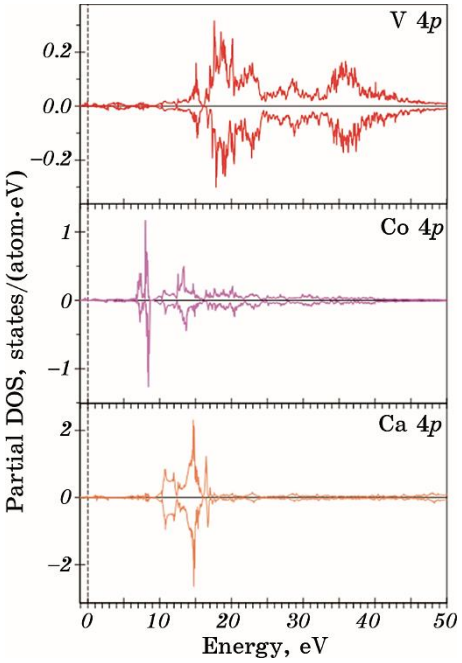

Fig. 5. The partial 4*p* density of states, in states/(atom·eV), of AFM $CaCo_3V_4O_{12}$ calculated in GGA + SOC + *U*.

and high energy shoulders quite well but fails to describe correctly the position of the high energy peak at 7778 eV. The Co *K*-XAS is extended over a very large interval up to 75 eV above the edge, and it is difficult to expect that a linear energy band structure method can describe the spectrum in such a large interval.

The V *K*-x-ray-absorption spectrum possesses two major peaks at 5485 eV and 5502 eV besides a low energy pre-peak at 5470 eV which we discuss later (Fig. 7). The theory reproduces well the energy position of two major peaks. Like in the case of Co *K*-XAS, the theory does not reproduce the energy position of the highest fine structure above 5530 eV.

The Ca *K*-x-ray-absorption spectrum possesses a two-peak fine structure at around 4049 eV and several small peaks between 4060 eV and 4120 eV (Fig. 8). The theory reproduces well the energy position of this two-peak structure, however, with inverse intensities of the peaks. Our calculations give the larger intensity for the high-energy peak but the experiment shows the larger intensity for the low energy peak. The structure of Ca *K*-XAS reflects the energy distribution of the corresponding Ca 4*p* partial DOS (see the lower panel of Fig. 5). The partial DOS has two peaks at 12 eV and 15 eV above the Fermi level, which produce the major two-peak structure in Ca *K*-XAS.

We investigate also the effect of the electric quadrupole E_2 transi-

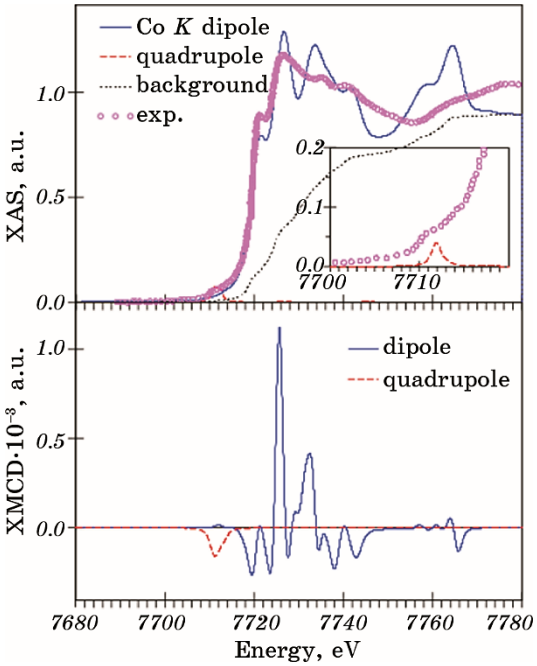

Fig. 6. Top panel: the experimental x-ray absorption spectrum (open circles) at the Co K-edge in $CaCo_3V_4O_{12}$ measured at 70 K [17] in comparison with the theoretically calculated one. The dotted black curve shows the background spectrum. Lower panel: the theoretically calculated XMCD of $CaCo_3V_4O_{12}$ at the Co K-edge. The dashed red curves show the quadrupole contributions to the spectra.

tions and magnetic dipole M_1 transitions on the XA and XMCD spectra at the transition metal K-edges. We found that the M_1 transitions are extremely small in comparison with the E_2 transitions and can be neglected. The E_2 transitions indeed contribute to the low energy XA spectra. Such transitions are responsible for the pre-peak structures of all three K-XA spectra shown in the inserts of Figs. 6, 7 and 8. The smallest E_2 contribution is found for the Co K-XA spectrum and the largest one for V K-XAS. The pre-peak in the Ca K-XA spectrum has a two-peak structure with the lower energy peak due to the dipole E_1 transitions and the higher energy one due to the quadrupole E_2 transitions (see the insert of Fig. 8).

The lower panels of Figures 6, 7 and 8 show the XMCD spectra at the Co, V, and Ca K-edges, respectively. The exchange splitting of the initial 1s core state is extremely small [35]; therefore, only the exchange and spin-orbit splitting of the final 2p states is responsible for the observed dichroism at the transition metal K-edge. For this reason, the dichroism is found to be very small, at least three orders of magnitude smaller than the XAS. The Co, V, and Ca K-XMCD spectra possess

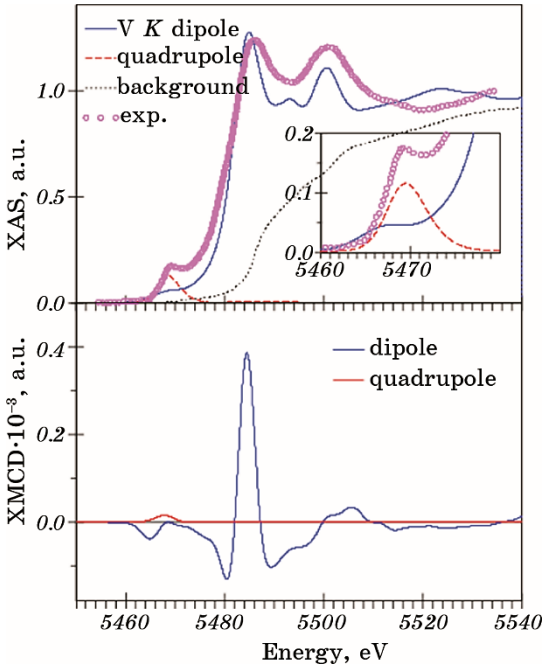

Fig. 7. Top panel: the experimental x-ray absorption spectrum (open circles) at the V K-edge in $CaCo_3V_4O_{12}$ measured at 70 K [17] in comparison with the theoretically calculated one. The dotted black curve shows the background spectrum. Lower panel: the theoretically calculated XMCD of $CaCo_3V_4O_{12}$ at the V K-edge. The dashed red curves show the quadrupole contributions to the spectra.

quite complicated structures with several minima and maxima. The largest contributions are found to come from the energy regions of the corresponding $3d$ states. The contributions of the quadrupole E_2 transitions to the XMCD spectra are one order of magnitude smaller than the dipole E_1 transitions and, hence, four orders of magnitude smaller than the intensity of the corresponding K-XAS. Therefore, the detection of the quadrupole transitions in the XMCD spectra of these $3d$ K-spectra is very close to impossible.

4. CONCLUSION

The electronic and magnetic structures as well as the XAS and x-ray magnetic circular dichroism of the A-site ordered perovskite $CaCo_3V_4O_{12}$ have been investigated theoretically within the DFT–GGA + U approach in the framework of the fully relativistic spin-polarized Dirac LMTO band-structure method.

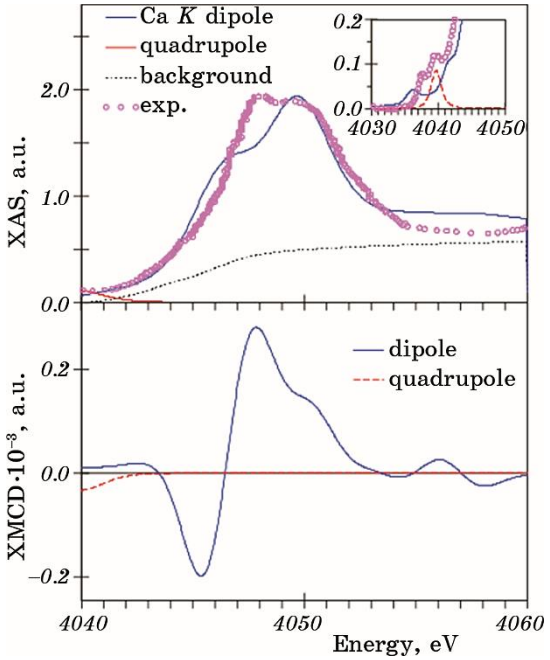

Fig. 8. Top panel: the experimental x-ray absorption spectrum (open circles) at the Ca K-edge in $CaCo_3V_4O_{12}$ measured at 70 K [17] in comparison with the theoretically calculated one. The dotted black curve shows the background spectrum. Lower panel: the theoretically calculated XMCD of $CaCo_3V_4O_{12}$ at the Ca K-edge. The dashed red curves show the quadrupole contributions to the spectra.

According to magnetic susceptibility and electrical resistivity measurements $CaCo_3V_4O_{12}$ possesses the AFM ordering and semiconducting behaviour at low temperature [19]. The collinear AFM $CaCo_3V_4O_{12}$ ground state calculated within the GGA and GGA + SOC approaches is metallic in contradiction to the experiment. Adding an on-site Coulomb repulsion on each of the Co and V ions results in a Mott-isolator-type electronic structure of $CaCo_3V_4O_{12}$. The energy band gap is rather small and equal to 0.109 eV at the Γ symmetry point. Both the Co^{2+} and V^{4+} ions are magnetic in Mott insulating $CaCo_3V_4O_{12}$. There is a substantial orbital moment over $1\mu_B$ at the Co site. Such a big orbital magnetic moment is due to a specific crystal structure of this double perovskite. The Co ion possesses the D_{2h} local symmetry in the rectangular CoO_4 plaquettes that leads to strong local anisotropy. Our calculations reveal that the Mott insulating character of the open-shell Co ions arises mostly through the d_{3z^2-1} orbital with a small amount of $d_{x^2-y^2}$. The 3d partial DOS of V ions is relatively small at the Fermi level.

We have studied the XAS and XMCD at the Co, V, and Ca K-edges.

The calculations show good agreement with the experimental measurements of the x-ray absorption spectra.

We have investigated the effect of the electric quadrupole E_2 and magnetic dipole M_1 transitions on the XA and XMCD spectra at the transition metal K-edges. We have found that the M_1 transitions are extremely small in comparison with the E_2 transitions and can be neglected. The E_2 transitions indeed contribute to the low energy part of XAS. Such transitions are responsible for the pre-peak structures of all three XA K-spectra. The smallest quadrupole contribution has been found for the Co K-XA spectrum and the largest for V K-XAS. The exchange splitting of the initial $1s$ core state is extremely small, therefore only the exchange and spin–orbit splitting of the final $2p$ states is responsible for the observed dichroism at the transition metal K-edge. For this reason, the dichroism has been found to be very small, at least three orders of magnitude smaller than the XA spectra. We have found that the largest quadrupole contributions come from the energy regions of the corresponding $3d$ states.

V. M. Antonov gratefully acknowledges the Max-Planck-Institut für Festkörperforschung in Stuttgart for the hospitality during his stay there.

REFERENCES

1. G. H. Jonker and J. H. van Santen, *Physica*, **16**, Iss. 3: 337 (1950).
2. E. O. Wollan and W. C. Koehler, *Phys. Rev.*, **100**: 545 (1955).
3. J. B. Goodenough, *Phys. Rev.*, **100**, 564 (1955).
4. M. Mochizuki and M. Imada, *New J. Phys.*, **6**: 154 (2004).
5. M. Imada, A. Fujimori, and Y. Tokura, *Rev. Mod. Phys.*, **70**: 1039 (1998).
6. A. M. Glazer, *Acta Cryst. B*, **28**: 3384 (1972).
7. C. J. Howard and H. T. Stokes, *Acta Cryst. B*, **54**: 782 (1998).
8. H. W. Eng, P. W. Barnes, B. M. Auer, and P. M. Woodward, *J. Solid State Chem.*, **175**: 94 (2003).
9. Beom Hyun Kim and B. I. Min, *Phys. Rev. B*, **80**: 064416 (2009).
10. A. Deschanvres, B. Raveau, and F. Tollemer, *Bull. Soc. Chim. Fr.*, **11**: 4077 (1967) (in French).
11. M. Marezio, P. D. Dernier, J. Chenavas, and J. C. Joubert, *J. Solid State Chem.*, **6**: 16 (1973).
12. C. C. Homes, T. Vogt, S. M. Shapiro, S. Wakimoto, and A. P. Ramirez, *Science*, **293**: 673 (2001).
13. Y. W. Long, N. Hayashi, T. Saito, M. Azuma, S. Muranaka, and Y. Shimakawa, *Nature*, **458**: 60 (2009).
14. R. D. Johnson, L. C. Chapon, D. D. Khalyavin, P. Manuel, P. G. Radaelli, and C. Martin, *Phys. Rev. Lett.*, **108**: 067201 (2012).
15. Y Shimakawa, *Inorg. Chem.*, **47**: 8562 (2008).
16. H. Shiraki, T. Saito, M. Azuma, and Y. Shimakawa, *J. Phys. Soc. Jpn.*, **77**: 064705 (2008).

17. S. V. Ovsyannikov, E. Bykova, A. Pakhomova, D. P. Kozlenko, M. Bykov, S. E. Kichanov, N. V. Morozova, I. V. Korobeinikov, F. Wilhelm, A. Rogalev, A. A. Tsirlin, A. V. Kurnosov, Y. G. Zainulin, N. I. Kadyrova, A. P. Tyutyunnik, and L. Dubrovinsky, *Inorg. Chem.*, **56**: 6251 (2017).
18. C. T. G. Petit, R. Lan, P. I. Cowin, J. T. S. Irvine, and S. Tao, *J. Mater. Chem.*, **21**: 525 (2011).
19. S. V. Ovsyannikov, Y. G. Zainulin, N. I. Kadyrova, A. P. Tyutyunnik, A. S. Semenova, D. Kasinathan, A. A. Tsirlin, N. Miyajima, and A. E. Karkin, *Inorg. Chem.*, **52**: 11703 (2013).
20. V. I. Anisimov, J. Zaanen, and O. K. Andersen, *Phys. Rev. B*, **44**: 943 (1991).
21. G. Y. Guo, H. Ebert, W. M. Temmerman, and P. J. Durham, *Phys. Rev. B*, **50**: 3861 (1994).
22. V. Antonov, B. Harmon, and A. Yaresko, *Electronic Structure and Magneto-Optical Properties of Solids* (Dordrecht: Springer: 2004).
23. E. Arola, M. Horne, P. Strange, H. Winter, Z. Szotek, and W. M. Temmerman, *Phys. Rev. B*, **70**: 235127 (2004).
24. H. B. Rhee and W. E. Pickett, *Phys. Rev. B*, **90**: 205119 (2014).
25. I. Leonov, A. N. Yaresko, V. N. Antonov, U. Schwingenschlögl, V. Eyert, and V. I. Anisimov, *J. Phys.: Condens. Matter*, **18**: 10955 (2006).
26. V. N. Antonov, B. N. Harmon, A. N. Yaresko, and A. P. Shpak, *Phys. Rev. B*, **75**: 184422 (2007).
27. V. N. Antonov, A. N. Yaresko, and O. Jepsen, *Phys. Rev. B*, **81**: 075209 (2010).
28. B. J. Ruck, H. J. Trodahl, J. H. Richter, J. C. Cezar, F. Wilhelm, A. Rogalev, V. N. Antonov, Binh Do Le, and C. Meyer, *Phys. Rev. B*, **83**: 174404 (2011).
29. O. Krogh Andersen, *Phys. Rev. B*, **12**: 3060 (1975).
30. V. V. Nemoshkalenko, A. E. Krasovskii, V. N. Antonov, Vl. N. Antonov, U. Fleck, H. Wonn, and P. Ziesche, *Phys. status solidi (b)*, **120**: 283 (1983).
31. J. P. Perdew, K. Burke, and M. Ernzerhof, *Phys. Rev. Lett.*, **77**: 3865 (1996).
32. P. E. Blöchl, O. Jepsen, and O. K. Andersen, *Phys. Rev. B*, **49**: 16223 (1994).
33. A. N. Yaresko, V. N. Antonov, and P. Fulde, *Phys. Rev. B*, **67**: 155103 (2003).
34. J. L. Campbell and Tibor Papp, *At. Data Nucl. Data Tables*, **77**: 1 (2001).
35. H. Ebert, *J. Phys.: Condens. Matter*, **1**: 9111 (1989).

Metallophysics and Advanced Technologies
Металофіз. новітні технол.
Metallofiz. Noveishie Tekhnol.
2023, vol. 45, No. 9, pp. 1083–1097
https://doi.org/10.15407/mfint.45.09.1083
Reprints available directly from the publisher

PACS numbers: 68.49.Jk, 68.49.Sf, 71.45.Gm, 73.20.Mf, 79.20.Uv, 79.40.+z, 82.80.Pv

Effect of Deformation on the Electronic Properties of the W(110) Single Crystals Surface Before and After Different Types of Surface Treatment

S. V. Smolnik[*], I. M. Makeieva[*], V. M. Kolesnyk[*], M. O. Vasylyev[*], M. Ya. Shevchenko[*], I. Ye. Galstian[*,**], E. G. Len[*,***]

[*]*G. V. Kurdyumov Institute for Metal Physics, N.A.S. of Ukraine, 36 Academician Vernadsky Blvd., UA-03142 Kyiv, Ukraine*
[**]*Institute for Solid State Research, Leibniz IFW Dresden, 20, Helmholtz Str., 01069 Dresden, Germany*
[***]*Kyiv Academic University, N.A.S. and M.E.S. of Ukraine, 36 Academician Vernadsky Blvd., UA-03142 Kyiv, Ukraine*

The electronic states' changes on the surface of the W(110) single crystal strained due to plastic bending are studied by the method of plasmon spectroscopy after thermal, thermochemical and ion treatments in comparison with those of analogous unstrained tungsten single crystal. The relative changes of the interplanar spaces, the concentration of the conduction electrons involved in plasma oscillations, as well as work function for electrons are calculated based on the plasmons' energy shifts. As established, the macroscopic bending of the W(110) single crystal leads to a decrease in the work function from its convex surface, which undergoes tensile deformation. The maximal difference in the work functions for unstrained and strained single crystals is observed after all sequentially used thermal, thermochemical and ion treatments and is of 0.2 eV. The obtained results are important for the practical application of thermionic energy converters with nonplanar electrodes.

Corresponding author: Sviatoslav Viktorovych Smolnik
E-mail: sviatsmol@gmail.com

Citation: S. V. Smolnik, I. M. Makeieva, V. M. Kolesnyk, M. O. Vasylyev, M. Ya. Shevchenko, I. Ye. Galstian, and E. G. Len, Effect of Deformation on the Electronic Properties of the W(110) Single Crystals Surface Before and After Different Types of Surface Treatment, *Metallofiz. Noveishie Tekhnol.*, **45**, No. 9: 1083–1097 (2023). DOI: 10.15407/mfint.45.09.1083

Key words: surface of tungsten single crystal, plastic deformation, plasmon spectroscopy, work function, thermionic energy converter.

Методою плазмонної спектроскопії досліджено зміни електронних станів поверхні деформованого за рахунок пластичного вигину монокристалу W(110) після термічного, термохемічного та йонного оброблень у порівнянні з аналогічним недеформованим монокристалом вольфраму. За зсувами енергії плазмонів розраховано відносну зміну міжплощинних віддалей, концентрацію електронів провідности, що беруть участь у плазмових коливаннях, а також роботу виходу електронів. Встановлено, що макроскопічний вигин монокристалу W(110) приводить до зменшення роботи виходу з його опуклої поверхні, яка зазнає деформації розтягнення. Максимальна ріжниця в роботах виходу недеформованого та деформованого монокристалів спостерігається після всіх послідовно реалізованих термічного, термохемічного та йонного оброблень і складає 0,2 еВ. Одержані результати є важливими для практичного застосування термоемісійних перетворювачів енергії з непласкими електродами.

Ключові слова: поверхня монокристалу вольфраму, пластична деформація, плазмонна спектроскопія, робота виходу електронів, термоемісійний перетворювач енергії.

(Received 11 June, 2023; in final version, 20 September, 2023)

1. INTRODUCTION

Currently, the practically single way to convert directly the heat of the high-temperature combustion cycle of nuclear (in the future, thermonuclear) or organic fuel into electricity is the embedding of thermionic converters (TICs) directly into the shells of both the furnaces and the hot zones of reactors [1, 2]. Tungsten single crystals are a promising material for use as cathodes in high-temperature TICs due to their low sublimation rate combined with high emission properties [3]. In order to struggle with the effect of evaporation of the cathode material without deteriorating the technical characteristics of the TIC during all its operation time, it is possible to use two different crystal faces of the same refractory metal single crystal: with larger work function of electron for the cathode manufacturing and with smaller one for the anode manufacturing. In the case of tungsten single crystals, the maximum electron work function is observed for the (110) crystal face [3], which determines the production of TIC cathodes from W(110) single crystals.

It is well known that many important electronic properties of single crystals, including the work function for electrons, are determined by the structure and physicochemical state of their surface layers. Impurities and adsorbates have a significant effect on the value of the work function. Their content on the surface and in the near-surface layers can be controlled by various thermal, thermochemical and radiation

treatments of the samples. Changes in the electronic state of the surface of refractory metals as a result of various types of processing can be studied by the method of plasmon spectroscopy (PS) [4–6]. Based on the determined excitation energies of plasmons (collective vibrations of conduction electrons), it is possible to calculate the concentration of conduction electrons, their work function, as well as the relative change of interplanar spaces depending on external influences on the state of the metal surface.

It is important that, in many cases, especially in compact and mobile nuclear energy sources or power-generating protective shells of future thermonuclear reactors, the TIC electrodes should not be flat, but have a rather complex geometry [7], when the emitter and collector are, for example, coaxial cylinders or tori with a small interelectrode gap. It is known that the adsorption capacity and high-temperature strength of cylindrical electrodes can be significantly increased if, instead of cylinders machined from a single crystal rod, the used cylinders are obtained by plastic deformation of crystallographically oriented plate with subsequent electron beam welding of the joints after it wrapping onto the surface of a given geometry [7]. The increase in high-temperature strength is due to the formation during plastic deformation of a high (up to 10^9 cm^{-2}) redundant density of dislocations of the same sign and its preservation up to pre-melting temperatures during stabilizing annealing [8]. Therefore, it is topical to study the electronic properties (especially the work function) of the working surfaces of TIC electrodes made from real deformed single crystals of refractory metals in comparison with unstrained ones, as well as the effect of various types of physicochemical treatments on them.

In connection with the above, the goal of this work is a comparative study using the method of plasmon spectroscopy of changes in the electronic state of strained by plastic deformation and unstrained single crystals of W(110) fabricated from the same single crystal rod, which subjected to thermal, thermochemical, and ion treatments at the same conditions.

2. RESEARCH OBJECTS AND METHODOLOGY

The plasmon excitation features in the secondary electron emission spectra has been studied for two samples of tungsten single crystal. Both samples were prepared from a single crystal strip of W(110) cutting with an accuracy of $\pm 20'$ from a single crystal rod grown by the electron beam crucibleless zone recrystallization method.

An unstrained sample of W(110) with a diameter of 10 mm and a thickness of 2 mm was cut from a single crystal by the electrospark method and subjected to further mechanical grinding and electropolishing from the side of the investigated surface. The deformed

W(110)-*D* sample has a form of plastically strained single crystal strip of 2 mm thick wrapped around a cylindrical surface with a radius of 14 mm. A detailed description of the preparation of this sample is given in Ref. [9]. The convex side of this sample, which was subjected to tensile stress during bending, was investigated. That is the convex side, which is used for electrons emitting in the case of the placement of nuclear fuel inside cylindrical capsules. Such devices can to supply for a long time with electricity the spaceships, submarines, and other objects, which have a problem with access to sunlight and organic fuels. In the case of a thermonuclear reactor, the inside torus of the protective shell (which can be immediately made double-layered) can use as a TIC cathode with emitting external convex side.

Preliminary, the W(110) and W(110)-*D* samples were subjected to step heating in the temperature range of 900–2400°C in a vacuum not lower than $5 \cdot 10^{-7}$ Pa. The determination of the content of impurities in single crystals of tungsten was carried out by the method of secondary ion mass spectrometry (SIMS) [10] in an ultrahigh vacuum facility using a liquid metal ion source [11]. The working substance for obtaining the initial ion current was liquid gallium. The diameter of Ga^+ ion beam was $\cong$ 10 μm, and the energy and density of the initial current were 9 keV and $1 \cdot 10^{-2}$ A·cm^{-2}, respectively. After heating at a certain temperature, the samples were cooled down during 15–20 minutes. Then, within 30 minutes, the surface of the samples was cleaned by the scanning beam of gallium ions. As a result of cyclic annealing and ion beam cleaning of the unstrained sample and after 30 minutes of heating at a temperature of 2400°C, all impurities were removed from the near-surface region, except carbon, the content of which, according to chemical analysis, did not exceed $1 \cdot 10^{-3}$ mass.% (Fig. 1, *a*). For the deformed sample, after a similar heat treatment, small peaks of carbon and oxygen impurities were observed near the sensitivity limit of the mass analyser, but an abnormally high amount of ionized water molecules was detected, which had been observed up to extremely high temperatures (2400°C) (Fig. 1, *b*).

The presence of adsorbed water in the surface layers and in the volume of heated metal samples is well known, but it is easily desorbed at a temperature of 530°C [9]. The formation and preservation of ionized water up to high temperatures in the volume of plastically deformed tungsten single crystal is probably related to the presence of a high density of dislocations of the same sign, stable up to the pre-melting temperature [8]. The probable cause of water entering into the volume of the single crystal is an insufficiently high vacuum ($7 \cdot 10^{-3}$ Pa) in the electron beam-welding chamber. When a single crystal plate is heated by an electron beam, water molecules can easily ionize and in this state enter into dislocation cores of the tungsten lattice, which are potential wells for these impurities [9]. The presence of O^+ and WO^+ peaks in the

secondary ion mass spectrum indicates an increased content of oxygen in dislocations at the surface of the deformed single crystal, which persists at least up to temperature of 2400°C.

The presence of ionized molecules of water in the surface layer of a deformed tungsten sample after high temperature annealing and ion etching is unusual, since it is known from studies of flat samples that all impurities, except carbon, are removed at high temperatures [12]. Subsequently, it is the heat-stimulated segregation of impurity carbon atoms from the volume to the surface of a flat tungsten single crystal that determines the sublimation and electronic properties of its surface. It is also worth noting the following. The C atoms are practically absent in the surface of deformed tungsten (Fig. 1, *b*). This may be due to the blocking of C atoms by ionized water molecules in a dislocation core. The formation of additional dislocations during the plastic deformation of a tungsten single crystal with the trapping of ionized molecules of water by them, can probably become a new effective method of obtaining surfaces of tungsten single crystals that would not contain carbon impurities.

All measurements by the method of plasmon spectroscopy were performed in ultra-high vacuum using a low-energy electron spectrometer at an operating pressure of residual gases not worse than $1 \cdot 10^{-7}$ Pa. The spectrometer is equipped with a four-grid hemispherical energy analyser, as well as electron and ion guns [13]. For peaks' separation in the spectrum of secondary electrons, the method of one-shot differentiation of the secondary current delay curve was used by recording the signal of the first harmonic of the collector current when the delay potential is modulated by a sinusoidal voltage [14]. The error in measurement of intensity and energy of surface and volume plasmons did

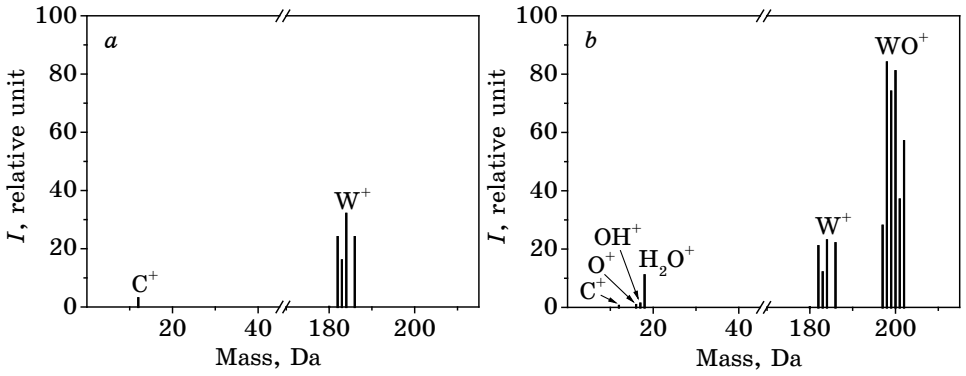

Fig. 1. Mass spectra of secondary ions of W(110) single crystals after cleaning with an ion beam and heating at a temperature of 2400°C for 30 min: *a*—undeformed plate; *b*—the convex side of a plastically deformed plate [9] (masses are measured in daltons (unified atomic mass unit)).

not exceed 5% .

During the experimental studies directly in the chamber of the electron spectrometer, the surfaces of the W(110) and W(110)-*D* samples were sequentially subjected to the following treatments: 1—annealing at a temperature of 1750°C for 540 min; 2—exposure in atomic oxygen at its pressure $P_{O_2} = 8 \cdot 10^{-4}$ Pa at a temperature of 1700°C for 180 min; 3—cleaning of the surface with argon ions with an energy of 800 eV and a current density of 5 μA·cm^{-2}; 4—annealing at a temperature of 1750°C for 200 min.

To obtain atomically pure oxygen, the copper oxide was pressed into a thin-walled platinum tube, and pure oxygen was released during it heating [15].

To study the effect of ion bombardment on the electronic properties of single crystals, an ion gun with ionization of the working gas by electron impact was used. Spectrally pure argon was used as the working gas.

After each type of surface treatment of the samples, the spectra of electrons' energy characteristic losses were recorded, the subsequent analysis of which provided data on the electronic properties of the surface.

3. RESULTS AND DISCUSSION

For experimental determination of the excitation losses because of surface and bulk plasmons, the electrons' energy loss spectra were recorded in the energy range of the primary electrons E_0 from 50 to 650 eV. In this case, the thickness of the investigated layer is 1.0–5.0 nm [16].

The Table 1 shows the averaged experimental energy values of surface $E_s = \hbar\omega_s$ and bulk $E_b = \hbar\omega_b$ plasmons (ω_s and ω_b are the oscillation frequencies of surface and bulk plasmons, respectively) after different types of step-by-step surface treatments of unstrained and deformed W(110) single crystals.

It is known that the bulk plasmon energy can be estimated within the free electron gas model according to the formula [17]

$$E_b = \hbar \sqrt{\frac{e^2 n}{m^* \varepsilon_0}}, \qquad (1)$$

where n is the density of valence electrons, e is the charge of an electron, m^* is the effective mass of electron, and ε_0 is the dielectric constant of vacuum.

If we assume that all valence electrons in the b.c.c. tungsten crystal (electronic configuration [Xe]$5d^4 6s^2$) are free and participate in plasmon oscillations, then, according to Eq. (1), we can obtain an estimation of $E_{b1} \cong 22.85$ eV. In the initial state, the bulk plasmon energy E_b

of the unstrained W(110) single crystal is close to the value of E_{b1} (see Table 1). The treatment of the surface of the W(110) single crystal at different regimes significantly increases the value of E_b compared to E_{b0}. The increase of the E_b values is a consequence of the increase of the electron concentration for b.c.c. tungsten at all processing modes used in the work compared to the initial state.

After annealing at a temperature of 1750°C for 540 min, the value of E_b increases by 0.4 eV (Table 1). Since all impurities, except carbon, are removed from the tungsten single crystal under such annealing conditions [12], the reason for this behaviour of E_b can only be the thermally stimulated segregation of impurity carbon atoms from the volume to the surface of the tungsten single crystal. The increase in electron density and the increase in E_b values should also be caused by the compressive microdeformation caused by defects (compared to the initial sample) in the near-surface layer of the macroscopically unstrained W(110) single crystal (Fig. 1). Tensile deformation has an inverse effect on E_b, which can be observed in the example of a macroscopically deformed W(110)-*D* single crystal (the convex side of the sample was studied).

The holding in atomically pure oxygen at a temperature of 1700°C does not significantly change the value of the bulk plasmon energy compared to the data obtained after the previous annealing stage. On the other hand, the bombardment of the surface with low energy Ar^+ ions leads to a certain decrease of the E_b values compared to the previous state, probably due to the formation of vacancy-type radiation defects and the removal of carbon from the near-surface layer and the processes of crystal lattice relaxation in it [18]. After the final annealing at a temperature of 1750°C for 200 minutes, the maximal effect of increasing the bulk plasmon energy of the unstrained W(110) single

TABLE 1. The average values of the surface (E_s) and bulk (E_b) plasmon energy (eV) for strained and unstrained W(110) single crystals.

Plasmon energy	Sample	Surface treatment modes				
		0	1	2	3	4
		Initial state	Annealing at 1750°C for 540 min	Exposure in O_2 at 1700°C for 180 min	Ion etching (Ar^+)	Annealing at 1750°C for 200 min
E_s, eV	W(110)	9.18	8.12	8.65	7.90	7.10
	W(110)-*D*	12.70	13.10	11.50	11.60	12.20
E_b, eV	W(110)	22.80	23.20	23.25	23.11	23.90
	W(110)-*D*	23.10	22.20	22.50	22.40	22.10

crystal is observed.

For the W(110)-*D* sample deformed by plastic bending in the initial state, a shift of the bulk plasmon energy by 0.3 eV towards higher energies is observed compared to the unstrained W(110). The presence of a distorted crystal lattice, ionized water in the dislocation core, and the presence of adsorbed particles on the surface lead to an increase in E_b value. After the first heat treatment of the W(110)-*D* surface, the value of E_b decreases significantly and then practically does not change after all successive modes of sample treatment.

The surface plasmon energy for all surface states of a deformed tungsten single crystal exceeds the surface plasmon energy of an unstrained sample. The case of a deformed crystal after the first heat treatment (with $E_b/E_s = 1.69$) is closest to the theoretical estimation of the ratio of bulk and surface plasmon energies ($E_s \approx E_b/\sqrt{2}$) [17]. However, it, as well as other cases, for which $E_b/E_s = 1.81–3.37$, is quite far from the estimated value of $\sqrt{2}$. This indicates the significant influence of effects not considered in the gas model of free electrons, such as impurities, microscopic and macroscopic deformations, and the chosen crystallographic direction, on the real energy values of both types of plasmons and on the relationship between them.

It is worth noting that the use of free electron gas approximation in the analysis of experimental data for metal, obtained within the framework of the method of electron energy characteristic losses, leads to the description of the dielectric permittivity of the medium by the Drude's formula: $\varepsilon(\omega) = 1 + \omega_b^2/\omega^2$. This approximation works well at high frequencies ($\omega >> \tau^{-1}$, τ is the relaxation time of the free electron gas, which at room temperature is of the order of 10^{-14} s), when the attenuation is small ($\mathrm{Im}\varepsilon \cong 0$). For elementary metals, the last condition is fulfilled, but for transition metals, due to the overlap of the *s*–*p* and *d* bands and the corresponding interband transitions, the condition $\mathrm{Im}\varepsilon \cong 0$ does not hold, which leads to the shifting and broadening of plasmon lines for the *s*–*p* electron subsystem, as well as to the 'joining' of the branches of the dispersion curve for bulk and surface plasmons (the energy gap disappears), but with a certain preservation of other characteristic features of separate areas that would correspond to two types of plasmons in the absence of significant attenuation. In the case of sufficiently low frequencies ($\omega << \tau^{-1}$), the approximation of the free electron gas (Drude's model) can be used until the condition $\lambda << \delta = c(2\pi\sigma\omega)^{-1/2}$ is fulfilled [19]. Here, λ is the average length of the electron free path, δ is the thickness of the skin layer, *c* is the speed of light in a vacuum, $\sigma = ne^2\tau/m^* = \omega_b^2\tau/(4\pi)$ is the specific electrical conductivity. At the same time, the energy transferred from primary electrons to metal electrons should correspond to the excitation of bulk plasmon oscillations (with $\mathrm{Im}\varepsilon \cong 0$): $E \cong 20–30$ eV [17]. Note that, for $E \cong 2–3$ eV, the contribution to the spectrum of energy characteristic

losses is mainly made by interband electron transitions. Above, we were talking about transverse plasmons. However, the consideration of longitudinal plasmons does not change the general picture, since according to experimentally determined not very large transmitted pulses they are also excited in the first approximation in the vicinity of the frequency ω_b [19]. The given considerations substantiate the applicability of Drude's formula not only for bulk but also for surface plasmons, the frequency of oscillations of which at not very small wavelengths are in the vicinity of the frequency $\omega_s \approx \omega_b/\sqrt{2}$ [17, 19]. In the same approximation, for sufficiently large values of the longitudinal wave number and for the macroscopic dimensions of the sample, it becomes possible to use the same formulas as for a flat surface in the case of a cylindrical surface of the (deformed) sample [19]. In the experiment for tungsten, the peaks of bulk and surface plasmons are clearly defined. Their relatively small width indicates that in this case the plasmons are well-defined quasiparticles. The deviations of the peaks' energy position from the estimated values (E_{b1} and $E_{b1}/\sqrt{2}$) are related not so much to the dispersion dependence $\omega(\mathbf{k})$ (this issue requires additional research, as well as the issue of deviation from the Drude's model), but to a change in the chemical composition, defect structure in the near-surface layer, and macroscopic deformation of the sample. Moreover, since different methods give significantly different absolute values of the work function, we are mainly interested in the magnitude of changes in the plasmon energy and the corresponding work function due to various types of processing and deformation. Therefore, in the framework of such consideration, all effects associated with deformation, defects, and other deviations from perfection (and isotropy; see work [4] for the W(100) surface) are reduced only to a certain change in interatomic distances and, accordingly, in electron concentration n.

Based on the principles outlined above and in Ref. [17], *i.e.*, assuming that the change in plasmon energy is related only to the change in electron concentration caused by the deformation of the crystal lattice, it is possible to calculate the relative changes in interplanar distances $\Delta d/d$ through the plasmon energy shifts using the formula:

$$\Delta d/d = -2\Delta E/E_b, \tag{2}$$

where $\Delta E = E_b - E_{b0}$ is the plasmon energy shift of the initial sample (E_{b0}) as a result of thermal, chemical and/or ion treatment of the latter, E_b is the averaged bulk plasmon energy after the corresponding impact on the sample.

As can be seen from Fig. 2, for the W(110)-*D* sample, positive values of the relative change in interplanar distances are observed for all processing modes compared to the initial state of the deformed sample.

The maximum increase in interplanar distances for the W(110)-*D* sample is observed after the final annealing at a temperature of 1750°C for 200 minutes (Fig. 2). For the unstrained sample, contrariwise, the effect of crystal lattice compression due to the diffusion of carbon atoms to the single crystal surface is observed after each surface treatment (Fig. 2). In this case, the relative deformations of the near-surface atomic layers of the W(110) sample for each treatment mode are several times larger by modulus than for the W(110)-*D* sample under the same treatment. The maximum reduction in interplanar distances is observed after cleaning the surface of the unstrained W(110) sample with low-energy Ar^+ ions, which is probably associated with perturbations in the atomic structure due to the formation of radiation defects and the implantation of Ar^+ ions in a single crystal.

As the interplanar distance d increases, the concentration of free electrons in the near-surface layer should decrease, and thus, the energy of the plasma oscillations should decrease too that is observed in the experiment for bulk plasmons of the W(110)-*D* sample (Fig. 2, Table 1). In contrast, for the unstrained W(110) sample, the interplanar distance decreases in all processing modes (Fig. 2) and the energy of bulk plasmons increases compared to the initial state of the sample (Table 1). The presence of plastic deformation in the W(110)-*D* sample leads to an additional increase in interplanar distances on its convex surface compared to the unstrained sample, resulting in lower E_b values for the W(110)-*D* single crystal than for W(110). This regularity occurs for all

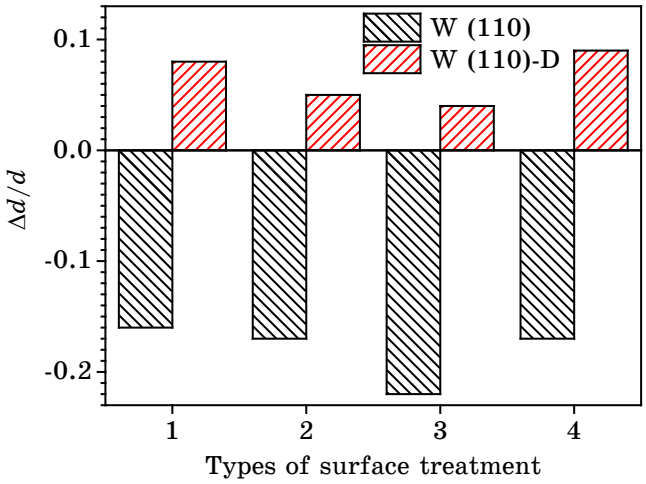

Fig. 2. Changes of interplanar spacing after various modes of the surfaces treatment; 1—annealing at 1750°C for 540 min; 2—exposure in oxygen at 1700°C for 180 minutes; 3—bombardment by Ar^+ ions; 4—annealing at 1750°C for 200 min.

treatment modes of the W(110)-*D* and W(110) samples (see Table 1), but it does not extend to these samples in the initial non-equilibrium state.

From Eq. (1), one can obtain an expression to calculate the concentration of conduction electrons n_p participating in surface and bulk plasma oscillations:

$$n_p = 0.724 \cdot E_p^2 \cdot 10^{21} \text{ cm}^{-3}, \quad (3)$$

where E_p is the surface (p = s) and bulk (p = b) plasmon energy, respectively. The concentrations of conduction electrons n_p (p = s, b) near the surface of the W(110) and W(110)-*D* samples are calculated from both the surface and bulk plasmon energies and shown in the Table. 2.

The concentration of conduction electrons according to the surface plasmon data decreases significantly for both samples, which is associated with the features of surface relaxation and the presence of defects in the surface structure. It should also be noted that n_s for W(110)-*D* is 2–3 times higher than the similar value for W(110), which indicates greater distortions of the surface layers of an unstrained single crystal compared to a plastically deformed one (which is also indicated by the analysis of the value of $\Delta d/d$, Fig. 2).

For the W(110) sample in the initial state, the conduction-electrons' concentration calculated from the bulk plasmon energies coincides with the value calculated by the free electron model and is equal to 6 electrons per atom (this is also an argument in favour of the applicability of the Drude's model). After successive surface treatments, an increase in the conduction electron concentration is observed due to the growth of compressive deformation in the W(110) near-surface layer. A certain increase in n_b in the initial state of the W(110)-*D* sample compared to the conduction electron concentration for the unstrained W(110) is associated (as well as the behaviour of the E_b value discussed above) with the deformation of the crystal lattice and the presence of ionized water and other defects in the volume and on the surface of the samples (see Fig. 1). As a result of the interplanar-distances' increasing after surface treatments of the W(110)-*D* single crystal, the con-

TABLE 2. Values of the conduction electrons' concentrations ($n_{s,b}$), el./atom (the treatment modes one can see in Table 1).

Plasmon type	Sample	Surface treatment modes				
		0	1	2	3	4
Surface	W(110)	0.97	0.77	0.86	0.72	0.57
	W(110)-*D*	1.87	1.95	1.50	1.55	1.70
Bulk	W(110)	6.0	6.24	6.24	6.18	6.60
	W(110)-*D*	6.16	5.70	5.86	5.84	5.65

centration of conduction electrons decreases and the covalent bond weakens [15], which should lead to a decrease in the work function of electrons from the surface. The maximum effect of n_b decrease occurs after the final annealing of the W(110)-*D* single crystal at a temperature of 1750°C for 200 min.

According to Ref. [20], the work function is connected with the bulk plasmon energy by the following relationship:

$$\varphi = 1.8 + (1/9)E_b. \quad (4)$$

The results of the corresponding calculations are shown in Fig. 3. As can be seen from this figure, for the unstrained sample in the initial state, the work function of electron from the (110)W surface is equal to 4.33 eV. After annealing at a temperature of 1750°C for 540 min, the work function increases to 4.38 eV, and after exposure in oxygen and bombardment with Ar^+ ions, it practically does not change. After final annealing at 1750°C, the value of φ rises sharply to a maximum of 4.46 eV. Heat treatment at temperatures of 1700 and 1750°C obviously leads, as mentioned above, to the activation of carbon diffusion and its segregation from the bulk to the surface of the W(110) crystal, which is reflected in a consistent increase in work function after surface treatments.

The surface of the deformed W(110)-*D* single crystal (Fig. 3) in its initial state has a rather large electron work function (4.37 eV), indi-

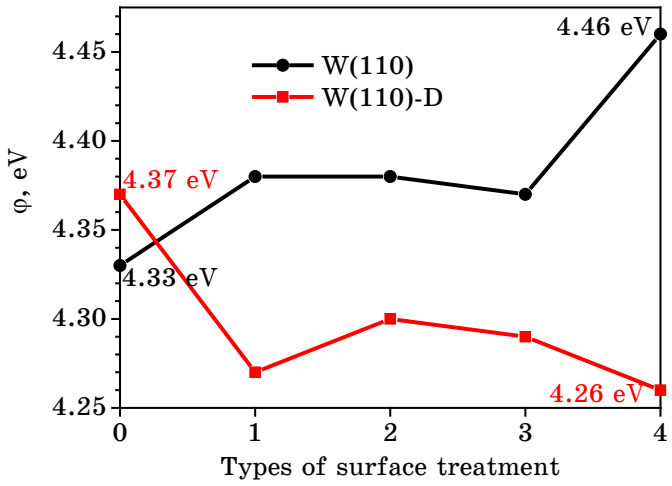

Fig. 3. Electron work function from the strained and unstrained surfaces W(110): 0—in the initial state; 1—after annealing at 1750°C for 540 minutes; 2—exposure in oxygen at 1700°C for 180 minutes; 3—bombardment by Ar^+ ions; 4—annealing at 1750°C for 200 min.

cating its non-equilibrium state and the presence of adsorbed particles on it. Annealing of the W(110)-*D* sample at a temperature of 1750°C for 540 min results in a sharp decrease of the work function to 4.27 eV. Further exposure in atomic oxygen increases the work function to 4.30 eV. Cleaning the surface with Ar^+ ions followed by annealing at a temperature of 1750°C for 200 min again leads to a decrease in the work function to a minimum value of 4.26 eV. It is important to note that after all treatments, the work function on the surface of a deformed single crystal is significantly less than the work function on the unstrained W(110) crystal. As shown above, in all modes of W(110)-*D* surface treatment, the interplanar distances are increased relative to the initial state, which, in turn, leads to a weakening of the covalent bond [15] and a decrease in the work function of electron.

Thus, the plastic deformation of the W(110) single crystal in the initial state slightly increases the electron work function for the emitting (convex) surface from 4.33 to 4.37 eV. Such increase can be caused by the non-equilibrium state of the deformed surface.

For all types of thermal, thermochemical and ionic treatments of a plastically deformed sample, the work function decreases in relation to both the initial deformed state and the unstrained sample after the same surface treatment. This is in accordance with the results of [21] regarding the general laws of the influence of deformation on the work function in metals. The maximum difference in the work function of deformed and unstrained single crystals is observed after the whole complex of successive thermal, thermochemical, and ionic treatments and is of 0.2 eV.

As can be seen from the above, the reason for the lower values of the work function at the surface of the deformed single crystal is the increase in the average value of the crystal lattice period of tungsten due to the appearance of dislocations during plastic deformation and the corresponding decrease in the interatomic interaction force. An important role in the formation of the electronic properties of an unstrained tungsten single crystal is played by the diffusion of C atoms from the volume to the surface, while the properties of a plastically deformed sample are more influenced by ionized water molecules captured by the nuclei of dislocations during the sample preparation stage.

4. CONCLUSIONS

1. Plastic deformation of the W(110) single crystal, which occurs, for example, due to its cylindrical bending during the formation of a closed TIC capsule with nuclear fuel or a thermonuclear reactor shell, slightly increases the work function of electron from the emitting convex surface (from 4.33 to 4.37 eV), despite the presence of macroscopic

tensile deformation. This growth is caused by non-equilibrium states of the deformed and unstrained surfaces of the W(110) single crystal and determines the need for thermal and other sample treatments before its practical use.

2. After all the above successive treatments, the deformed and unstrained samples pass into more equilibrium states that is accompanied by a restructuring of their surface and a change in the corresponding electronic properties. Thus, at high temperatures, carbon diffusion is activated in the unstrained sample and its segregation occurs from the bulk to the surface of the W(110) single crystal, which is reflected in a decrease of the interplanar distance in the near-surface layer leading to a local increase of the electron concentration and the work function after the selected successive surface treatments. Ion etching slightly breaks the monotony of this dependence due to the formation of additional radiation defects. For the plastically deformed sample W(110)-*D*, all successive treatments lead to a significant relaxation of macro- and microstrains. An important role in the formation of the electronic properties is played the presence of a high density of dislocations of the same sign (up to 10^9 cm^{-2}) and ionized water molecules captured by dislocations at the stage of sample preparation. All treatments lead to an increase in the interplanar distances in the near-surface layer, a local decrease in the electron concentration, and a corresponding decrease in the work function of the convex side of the plastically deformed W(110) single crystal relative to both the initial state of the W(110)-*D* sample and the unstrained sample after the same surface treatments.

3. The maximum difference in the values of work function of unstrained and deformed crystals is observed after the whole complex of sequentially performed thermal, thermochemical and ion treatments and is 0.2 eV, which is important to consider for designing thermionic energy converters with cylindrically deformed electrodes.

4. The practically absence of carbon atoms on the surface of deformed tungsten sample can be caused by the blocking of carbon segregation to the surface by ionized water molecules in the dislocation nuclei. The formation of additional dislocations during plastic deformation of a sample, together with ionized water molecules capturing by them, can become a new effective method of obtaining surfaces of single crystals of refractory metals and their alloys, which would not contain carbon impurity.

ACKNOWLEDGMENTS

This work was supported by projects Nos. 0119U001167 and 0123U102275 of the National Academy of Sciences of Ukraine, and partially by UKRAPRO scholarship program for Ukrainian researchers (Volkswagen Foundation).

REFERENCES

1. M. F. Campbell, T. J. Celenza, F. Schmitt, J. W. Schwede, and I. Bargatin, *Adv. Sci.*, **8**: 2003812 (2021).
2. A. V. Belkin and N. V. Schukin, *Phys. Atom. Nuclei*, **84**: 1522 (2021).
3. V. S. Fomenko, *Ehmissionnyye Svoistva Materialov: Spravochnik* [Emission Properties of Materials: Handbook] (Kiev: Naukova Dumka: 1981) (in Russian).
4. M. O. Vasylyev, E. G. Len, V. M. Kolesnik, I. M. Makeeva, V. I. Patoka, and S. V. Smolnik, *Metallofiz. Noveishie Tekhnol.*, **42**, No. 4: 471 (2020) (in Russian).
5. M. A. Vasylyev and V. A. Tinkov, *Surface Review and Letters*, **15**, No. 5: 635 (2008).
6. M. O. Vasylyev, V. M. Kolesnik, S. I. Sidorenko, S. M. Voloshko, V. V. Yanchuk, and A. K. Orlov, *Metallofiz. Noveishie Tekhnol.*, **40**, No. 7: 919 (2018) (in Ukrainian).
7. L. V. Demchenko, A. I. Dekhtyar, and V. A. Kononenko, *Металлофизика*, **6**, № 3: 112 (1984) (in Russian).
8. L. V. Demchenko, A. I. Dekhtyar, and A. P. Starzhinskij, *Phys. Met. Metallog.*, **80**, No. 3: 312 (1995).
9. A. I. Dekhtyar, V. N. Kolesnik, V. I. Patoka, and N. A. Shevchenko, *Metallofiz. Noveishie Tekhnol.*, **23**, No. 3: 335 (2001) (in Russian).
10. V. T. Cherepin and M. A. Vasil'ev, *Metody i Pribory dlya Analiza Poverkhnosti Materialov: Spravochnik* [Methods and Instruments for Surface Analysis of Materials: Handbook] (Kiev: Naukova Dumka: 1982) (in Russian).
11. G. G. Managadze, V. T. Cherepin, Y. G. Shkuratov, V. N. Kolesnik, and A. E. Chumikov, *Icarus*, **215**, No. 1: 449 (2011).
12. V. I. Patoka, *Doslidzhennya Parametriv Vyparovuvannya Tugoplavkykh Metaliv ta Yikh Splaviv u Nadvysokomu Vakuumi* [Study of Evaporation Parameters of Refractory Metals and Their Alloys in Ultrahigh Vacuum] (Disser. for Cand. Phys.-Math. Sci.) (Kyiv: G. V. Kurdyumov Institute for Metal Physics, N.A.S.U.: 2020) (in Ukrainian).
13. M. A. Vasil'ev and S. D. Gorodetsky, *Vacuum*, **37**: 723 (1987).
14. V. A. Tinkov, M. A. Vasylyev, and G. G. Galstyan, *Vacuum*, **85**: 677 (2011).
15. I. Ya. Dekhtyar, V. N. Kolesnik, V. I. Patoka, and V. I. Silantiev, *DAN USSR, Ser. A*, No. 12: 1124 (1975) (in Russian).
16. V. E. Korsukov, A. S. Luk'yanenok, and V. N. Svetlov, *Poverkhnost'. Fizika, Khimiya, Mekhanika*, No. 11: 28 (1983) (in Russian).
17. D. Pines, *Elementary Excitation in Solids* (New York: Benjamin Press: 1963).
18. M. A. Vasylyev, S. P. Chenakin, and V. A. Tinkov, *Vacuum*, **78**: 19 (2005).
19. V. V. Klimov, *Nanoplasmonics* (Moskva: Fizmatlit: 2010) (in Russian).
20. E. A. Bakulin and M. M. Bredov, *Fiz. Tverd. Tela*, **12**, No. 3: 891 (1977) (in Russian).
21. W. Li and D. Y. Li, *Phil. Mag.*, **84**, No. 35: 3717 (2004).

Metallophysics and Advanced Technologies
Металофіз. новітні технол.
Metallofiz. Noveishie Tekhnol.
2023, vol. 45, No. 9, pp. 1099–1107
https://doi.org/10.15407/mfint.45.09.1099
Reprints available directly from the publisher

PACS numbers: 02.30.Jr, 02.30.Nw, 05.65.+b, 61.72.Bb, 61.72.jd, 82.40.Ck, 82.40.Np

Утворення упорядковних розподілів температури та вакансій під час деформації металевих кристалів

О. Е. Засимчук, В. І. Засимчук, Т. В. Турчак, О. І. Баскова, О. С. Гаценко

Інститут металофізики ім. Г. В. Курдюмова НАН України,
бульв. Академіка Вернадського, 36,
03142 Київ, Україна

У статті розглянуто тривимірні рівняння теплопровідности та дифузії: а) за малої, але впорядкованої функції теплових джерел $f(r,t)$; б) за $f(r,t) \equiv 0$. Розглянуто як стаціонарний, так і нестаціонарний випадки та встановлено, що утворюються, як завгодно складні розподіли температури та концентрації вакансій по координатах. Показано, що всередині зразка можуть виникати нові двовимірні структури, яких не задано крайовими умовами.

Ключові слова: рівняння теплопровідности, дифузія, функція теплових джерел, вакансії, впорядкований розподіл, стаціонарний розв'язок, ряд Фур'є, самоорганізація, гідродинамічні канали.

Three-dimensional equations of heat conduction and diffusion are considered in the article: a) with a small, but well-ordered function for thermal sources $f(r,t)$; b) for $f(r,t) \equiv 0$. Stationary and non-stationary cases are discussed, and the formation of arbitrary complex distributions of temperature and concentrations of vacancies along co-ordinates is established. As shown, new two-dimensional structures not specified by the boundary conditions arise within the sample.

Key words: thermal-conduction equation, diffusion, heat-source function,

Corresponding author: Oleksandr Serhiyovych Gatsenko
E-mail: gats@imp.kiev.ua

G. V. Kurdyumov Institute for MetalPhysics, N.A.S. of Ukraine,
36 Academician Vernadsky Blvd., UA-03142 Kyiv, Ukraine

Citation: O. Eh. Zasymchuk, V. I. Zasymchuk, T. V. Turchak, O. I. Baskova, and O. S. Gatsenko, Formation of Ordering Temperature and Vacancies' Distributions During Deformation of Metal Crystals, *Metallofiz. Noveishie Tekhnol.*, **45**, No. 9: 1099–1107 (2023). DOI: 10.15407/mfint.45.09.1099

vacancies, ordered distribution, stationary solution, Fourier series, self-organization, hydrodynamic channels.

(Отримано 8 вересня 2020 р.; остаточн. варіянт — 10 січня 2023 р.)

1. ВСТУП

Питанням самоорганізації різних структурних параметрів матеріялів за енергетичних впливів займалися у багатьох роботах (див., наприклад, [1, 2]), але досі всі процеси, що відбуваються за цих умов, не було детально описано із врахуванням самоорганізації температури під час впливу на металевий кристал у механічному полі. За такого впливу кристал деформується, і за значної віддаленості від рівноваги деформується пластично. Також відомо, що за гальмування дислокаційного ковзання через розвиток деформаційної релаксаційної структури [3, 4] пластична деформація відбувається шляхом гідродинамічної течії по каналах з рідиноподібною структурою — так званих гідродинамічних каналах (ГК), яка збагачена вакансіями [5]. Цей процес супроводжується розігрівом матеріялу та складним розподілом температури кристалу в процесі навантаження [6, 7], що є наслідком деформаційного структуроутворення, зокрема утворення ГК. Враховуючи ці дані, нами було проведено аналітичні розрахунки, які показали зв'язок між розігрівом кристалу в процесі пластичної деформації та розподілом температури, що пов'язано з механізмом деформаційного структуроутворення.

Ці розрахунки проводилися за допомогою розв'язання рівняння теплопровідности, чим займалися здавна [8] й по наш час [9, 10, 11]. У нашій роботі ми знайшли розв'язки з малою чи нульовою функціями теплових джерел (ФТД) $f(r,t)$ та сильним коливанням температури $u(r,t)$. Ця робота цікава також і тим, що такий же вигляд має рівняння дифузії [12].

2. РЕЗУЛЬТАТИ РОЗРАХУНКІВ

Запишемо рівняння теплопровідности:

$$\frac{du}{dt} - a^2 \Delta u = f(r,t)\,,\ -L_x \le x \le L_x, -L_y \le y \le L_y, -L_z \le z \le L_z\,, \qquad (1)$$

де $u(r,t)$ задає температуру в точці з координатами $\mathbf{r}$ у момент часу t, a^2 — коефіцієнт теплопровідности, $f(r,t)$ — функція теплових джерел, Δ — Ляплясів оператор [8]. Такий же вигляд має й рівняння дифузії, зокрема дифузії вакансій [12].

Крайові умови див. у (12)–(14) і далі. Початкові умови див. у (44)–(46).

Нехай маємо прямокутній зразок. Тоді функція теплових джерел $f(r,t)$ має вигляд:

$$f(r,t) = A\cos(q_x x)\cos(q_y y)g(z)\,, \tag{2}$$

$$g(z) = D_1\exp(pz) + D_2\exp(-pz)\,, \tag{3}$$

де q_x, q_y, p — дійсні числа, A, D_1, D_2 — деякі константи.

Така функція може виникати, наприклад, на осях Ox й Oy за рахунок теплових коливань атомів у ґратниці [13]. Так, у роботі [13] одержано вираз для зміщення атомів у ланцюжку x_1:

$$x_1 = h\cos(qn)\sin(\omega t)\,, \tag{4}$$

де n — номер атома, h, q, ω — деякі константи. Відповідно, швидкість атома v визначається виразом

$$v = h_1\cos(qn)\cos(\omega t)\,, \tag{5}$$

де $h_1 = h\omega$.

Функція теплових джерел пропорційна кінетичній енергії атомів, тобто

$$f(r,t) = f_1 + f_2 = h_2 m v^2 = H_1\cos^2(qn)\cos^2(\omega t) = H\cos^2(\omega t)(1+\cos(2qn))\,, \tag{6}$$

де m — маса атома, h_2, H_1, H — деякі константи. Таким чином, одна зі складових $f(r,t)$, — функція $f_2(n,t)$, — визначається виразом

$$f_2(n,t) = H\cos^2(\omega t)\cos(2qn)\,, \tag{7}$$

що відповідає (2).

По осі Oz нашу ФТД одержуємо за рахунок внутрішніх напружень, які з'являються, наприклад, як результат циклічного навантаження [14].

Шукаємо u у вигляді

$$u = B\cos(q_x x)\cos(q_y y)g(z) + C_1\,. \tag{8}$$

Підставляємо (8) у (1). Маємо:

$$B = \frac{A}{a^2 c}\,, \tag{9}$$

$$c = q_x{}^2 + q_y{}^2 - p^2\,. \tag{10}$$

Тоді

$$\lim_{|c|\to 0}|B| = \infty . \tag{11}$$

Таким чином, ми бачимо, що для $|c| \to 0$ навіть за малого значення функції теплових джерел $f(r)$ маємо впорядкований розподіл температури $u(r)$ у зразку з великими амплітудами коливань.

Розглянемо зразок у формі прямокутнього паралелепіпеда. Можна записати рівняння для меж зразка:

$$|x| = L_x, \ \ |y| = L_y, \ \ |z| = L_z , \tag{12}$$

де L_x, L_y, L_z — позитивні константи. Припустимо, що ФТД $f(r,t)$ є такою, що виконуються умови

$$q_x = \left(\pi + 2\pi j_x\right)/2L_x , \ \ q_y = \left(\pi + 2\pi j_y\right)/2L_y , \tag{13}$$

де j_x, j_y — натуральні числа і 0. Тоді розв'язок (8) рівняння (1) має крайові умови:

$$u(|x| = L_x) = u(|y| = L_y) = C_1 , \tag{14}$$

тобто коливання в (1) задаються лише по осі Oz.

Визначимо

$$Bg\left(L_z\right) = C_2, \ \ Bg\left(-L_z\right) = C_3 .$$

Тоді з (8)

$$u(L_z) = C_2\cos(q_x x)\cos(q_y y) + C_1, \ u(-L_z) = C_3\cos(q_x x)\cos(q_y y) + C_1 ,$$

тобто, щоби описаний в нашій роботі ефект мав місце, обов'язкові періодичні крайові умови по осі Oz.

Розглянемо випадок

$$c \to 0 . \tag{15}$$

Тоді з (10) і (13) маємо

$$p \approx ({q_x}^2 + {q_y}^2)^{1/2} = \left(\pi^2 / 4\right)((1+2j_x)^2 / {L_x}^2 + (1+2j_y)^2 / {L_y}^2)^{1/2} . \tag{16}$$

Це означає, що чим тонше зразок, тим більше p, тобто тим швидше u спадає з глибиною проникнення у середину зразка по вісі Oz.

1. Візьмемо, наприклад, товстий зразок:

$$2L_x = 2L_y = 3{,}14 \text{ см} . \tag{17}$$

Тоді з (13) для

$$j_x = j_y = 0\,, \tag{18}$$

$$q_x = q_y = 1\ \text{см}^{-1} \tag{19}$$

із (16) маємо:

$$p \approx (2)^{1/2}\ \text{см}^{-1} = 1,41\ \text{см}^{-1}\,. \tag{20}$$

2. Розглянемо тепер тонкий зразок; наприклад,

$$2L_x = 2L_y = 94,2\ \text{мкм} = 94,2 \cdot 10^{-4}\ \text{см}\,. \tag{21}$$

Тоді з (13) із врахуванням (18)

$$q_x = q_y = \left(10^3 / 3\right)\ \text{см}^{-1} \tag{22}$$

і з (16)

$$p_1 = 10^2 \left(200 / 9\right)^{1/2} = 471\ \text{см}^{-1}, \tag{23}$$

$$p_1 / p = 334,04\,. \tag{24}$$

Таким чином, у тонкому зразку u спадає з глибиною проникнення приблизно у $\cong 334$ рази швидше, ніж у товстому.

2.1. Випадок $c = 0$

Як ми бачимо з (1), (8) і (10) при

$$c = 0 \tag{25}$$

навіть для $f(r,t) \equiv 0$ ми маємо розв'язок (1) у вигляді (8) (стаціонарний розв'язок). Це ж є слушним для аналогічного рівняння дифузії і т.д. Слушним є також розв'язок

$$u = \sum_n \sum_m B_{nm} \cos(q_{xn} x) \cos(q_{ym}) g_{nm}(z)\,, \tag{26}$$

якщо для всіх n і m слушною є умова

$$c_{nm} = q_{xn}^{\ 2} + q_{ym}^{\ 2} - p_{nm}^{\ 2} = 0\,. \tag{27}$$

Оскільки практично будь-яку функцію можна розвинути в ряд Фур'є [12], ми можемо мати у стаціонарному стані практично любу

двовимірну функцію $F_i(x,y)$. Зрозуміло, що такі функції є різними для різних z.

Коефіцієнти B_{nm}, q_{xn}, q_{ym} можна знайти з крайових умов.

2.2. Нестаціонарний випадок

Припустимо, що навантаження діє симетрично вздовж осі Oz. Тоді

$$u = \sum_n \sum_m u_{nm} = \exp(\xi t) \sum_n \sum_m A_{nm} \mathrm{ch}(p_{nm} z) \cos(q_{xn} x) \cos(q_{ym} y) . \qquad (28)$$

Будемо шукати функцію $u(x,y,z,t)$, що відповідає крайовим умовам

$$u_{|z|=L} = \omega(x,y) \exp(\xi t) . \qquad (29)$$

Тут ξ, p_{nm}, q_{xn}, q_{ym} — константи, $\omega(x,y)$ — деяка функція. (Ми вважаємо, що маємо прямокутній зразок з $-L_x < x < L_x$, $-L_y < y < L_y$, $-L_z < z < L_z$.)

З (29) одержимо

$$u = A \exp(\xi t) \mathrm{ch}(p_{00} z) \sum_n \sum_m a_{nm} b_{nm} (\mathrm{ch}(p_{nm} z) / \mathrm{ch}(p_{00} z)) f_{nm} , \qquad (30)$$

$$f_{nm} = \cos(q_{xn} x) \cos(q_{ym} y) , \qquad (31)$$

$$b_{nm} = \frac{\mathrm{ch}(p_{00} L)}{\mathrm{ch}(p_{nm} L)} , \qquad (32)$$

a_{nm} — коефіцієнти розвинення функції $u(x,y,z)$ в ряд Фур'є з прийняттям до уваги крайових умов (29) у припущенні, що для всіх n і m $p_{nm} = 0$. Тоді при $|z| \neq L$ маємо

$$u(z) = A \exp(\xi t) \mathrm{ch}(p_{00} z)(v_0 + v) , \qquad (33)$$

$$v_0 = \sum_n \sum_m a_{nm} f_{nm}(xy) , \qquad (34)$$

$$v(z) = \sum_{n=1}^{\infty} \sum_{m=1}^{\infty} a_{nm} (b_{nm} F(z) - 1) f_{nm} , \qquad (35)$$

$$F(z) = \frac{\mathrm{ch}(p_{nm} z)}{\mathrm{ch}(p_{00} z)} = \frac{\mathrm{ch}(Qz)}{\mathrm{ch}(pz)} . \qquad (36)$$

Визначимо

$$F_1(z) = \frac{1}{F(z)} . \qquad (37)$$

У нас

$$Q = p_{nm} >> p = p_{00}\,. \tag{38}$$

Тому

$$\exp(-Qz) << \exp(Qz)F_1(z) \approx \exp((p-Q)z) + \exp(-(p+Q)z)\,. \tag{39}$$

Припускаємо

$$F_1(z) \approx \exp((p-Q)z) + \exp(-(p+Q)z)\,. \tag{40}$$

Звідси

$$\frac{dF_1}{dz} < 0,\ \ \frac{dF}{dz} > 0,\ \ b_{nm}F(z) = \frac{F(z)}{F(L)} < 1\,, \tag{41}$$

оскільки $z < L$.

Таким чином,

$$v(x,y,z) \neq 0\,. \tag{42}$$

Нагадаємо , що для всіх n і m має виконуватися рівняння

$$\xi - a^2(p_{nm}{}^2 - q_{xn}{}^2 - q_{ym}{}^2) = 0 \tag{43}$$

(див. (1)). Можна побачити, що член $v_0(x,y,z)$ описує клясичний розв'язок (1), а член $v(x,y,z)$ — самоорганізований розв'язок (1), наприклад, розташування вакансій, які потім можуть перетворитися на гідродинамічні канали.

2.3. Початкові умови для (1)

1) Стаціонарний випадок. Як ми бачимо з (8),

$$u_{t=0} = B\cos(q_x x)\cos(q_y y)g(z) + C_1\,. \tag{44}$$

2) Нестаціонарний випадок. Як ми бачимо з (28),
а) при $\xi > 0$

$$u_{t=0} \approx 0\,, \tag{45}$$

б) при $\xi < 0$

$$u_{t=\infty} = 0\,. \tag{46}$$

3. ОБГОВОРЕННЯ РЕЗУЛЬТАТІВ І ВИСНОВКИ

1. Постає важливе питання: як же виникають функції теплових джерел (ФТД) вигляду (2). Ми припускаємо, що по осях *Ox* й *Oy* вони виникають за рахунок теплових коливань атомів у ґратниці [13], а по осі *Oz* — за рахунок внутрішніх напружень, які з'являються, наприклад, як результат циклічного навантаження [14]. У роботах [6, 7] спостерігалися так звані плями оксидів, які виникають за дуже високих температур. Можна зробити припущення, що в цьому випадку ФТД були такими, що набувають малих числових значень (див. (10), (11)).
2. Досі вважалося, що теплопровідність і дифузія приводять до вирівнювання температур і концентрацій вакансій по всьому об'єму зразка. Ми ж одержали стаціонарний розв'язок у вигляді як завгодно складного розподілу цих параметрів по координатах (див. (26)). В усіх випадках ми розглядали поведінку вакансій лише в механічному полі деформації, а не в опроміненому зразку (як у роботах [15, 16]).
3. Нами було одержано явний математичний вигляд опису зародків гідродинамічних каналів.

ЦИТОВАНА ЛІТЕРАТУРА

1. E. Zasimchuk, T. Turchak, and N. Chausov, *Results Mater.*, **6**: 100090 (2020).
2. E. Zasimchuk, L. Markashova, O. Baskova, T. Turchak, N. Chausov, V. Hutsaylyuk, and V. Berezin, *J. Mater. Eng. Perform.*, **22**, No. 7: 3421 (2013).
3. E. Zasimchuk, O. Baskova, O. Gatsenko, and T. Turchak, *J. Mater. Eng. Perform.*, **26**, No. 3: 1293 (2017).
4. Е. Э. Засимчук, В. И. Засимчук, Т. В. Турчак, *Успехи физ. мет.*, **14**, № 3: 275 (2013).
5. Yu. G. Gordienko and E. E. Zasimchuk, *Philos. Mag. A*, **70**, No. 1: 99 (1994).
6. Н. Д. Бега, Е. Э. Засимчук, С. Н. Каверина, С. А. Фирстов, *Металлофизика*, **2**, № 1: 71 (1980).
7. В. Т. Трощенко, Е. Э. Засимчук, Н. Д. Бега, *Физ. мет. металловед.*,**45**, № 4: 850 (1978).
8. Б. М. Яворский, А. А. Детлаф, *Справочник по физике для инженеров и студентов вузов* (Москва: Гос. изд. физ.-мат. лит.: 1963).
9. T. Blomberg, *Byggnadsfysik LTH* (Lunds Tekniska Högskola: 1996).
10. S. Ahmed, P. Singh, and S. Ekkad, *ASME. J. Heat Transfer*, **142**, Iss. 5: 051302 (2020).
11. Г. С. Карслоу, Д. С. Егер, *Теплопроводность твердых тел* (Москва: Наука: 1964) (пер. з англ.).
12. Г. Корн, Т. Корн, *Справочник по математике для научных работников и инженеров* (Москва: Наука: 1978) (пер. з англ.).
13. В. И. Засимчук, Е. Э. Засимчук, *Металлофиз. новейшие технол.*, **41**, № 6: 765 (2019).
14. В. Т. Трощенко, *Деформирование и разрушение металлов при многоцикло-*

вом нагружении (Киев: Наукова думка :1981).
15. О. В. Олійник, В. А. Татаренко, *Допов. Нац. акад. наук Укр.*, № 3: 55 (2019).
16. O. V. Oliinyk and V. A. Tatarenko, *Radiation Effects and Defects in Solids*, **174**, Iss. 5–6: 519 (2019).

REFERENCES

1. E. Zasimchuk, T. Turchak, and N. Chausov, *Results Mater.*, **6**: 100090 (2020).
2. E. Zasimchuk, L. Markashova, O. Baskova, T. Turchak, N. Chausov, V. Hutsaylyuk, and V. Berezin, *J. Mater. Eng. Perform.*, **22**, No. 7: 3421 (2013).
3. E. Zasimchuk, O. Baskova, O. Gatsenko, and T. Turchak, *J. Mater. Eng. Perform.*, **26**, No. 3: 1293 (2017).
4. E. E. Zasimchuk, V. I. Zasimchuk, and T. V. Turchak, *Uspehi Fiz. Met.*, **14**, No. 3: 275 (2013) (in Russian).
5. Yu. G. Gordienko and E. E. Zasimchuk, *Philos. Mag. A*, **70**, No. 1: 99 (1994).
6. N. D. Bega, E. Eh. Zasimchuk, S. N. Kaverina, and S. A. Firstov, *Metallofizika*, **2**, No. 1: 71 (1980) (in Russian).
7. V. T. Troshchenko, E. E. Zasimchuk, and N. D. Bega, *Fiz. Met. Metalloved.*, **45**, No. 4: 850 (1978) (in Russian).
8. B. M. Yavorsky and A. A. Detlaf, *Spravochnik po Fizike dlya Inzhenerov i Studentov Vuzov* [Handbook of Physics for Engineers and University Students] (Moskva: Gos. Izd. Fiz.-Mat. Lit.: 1963).
9. T. Blomberg, *Byggnadsfysik LTH* (Lunds Tekniska Högskola: 1996).
10. S. Ahmed, P. Singh, and S. Ekkad, *ASME. J. Heat Transfer*, **142**, Iss. 5: 051302 (2020).
11. G. S. Carslaw and J. C. Jaeger, *Teploprovodnost Tverdykh Tel* [Conduction of Heat in Solids] (Moskva: Nauka: 1964) (Russian translation).
12. G. Korn and T. Korn, *Spravochnik po Matematike dlya Nauchnykh Rabotnikov i Inzhenerov* [Handbook of Mathematics for Scientists and Engineers] (Moskva: Nauka: 1978) (Russian translation).
13. V. I. Zasimchuk and E. Eh. Zasimchuk, *Metallofiz. Noveishie Tekhnol.*, **41**, No. 6: 765(2019) (in Russian).
14. V. T. Troshchenko, *Deformirovanie i Razrushenie Metallov pri Mnogotsiklovom Nagruzhenii* [Deformation and Destruction of Metals under High-Cycle Loading] (Kiev: Naukova Dumka: 1981) (in Russian).
15. O. V. Oliinyk and V. A. Tatarenko, *Dopov. Nac. acad. Nauk Ukr.*, No. 3: 55 (2019) (in Ukrainian).
16. O. V. Oliinyk and V. A. Tatarenko, *Radiation Effects and Defects in Solids*, **174**, Iss. 5–6: 519 (2019).

Metallophysics and Advanced Technologies
Металофіз. новітні технол.
Metallofiz. Noveishie Tekhnol.
2023, vol. 45, No. 9, pp. 1109–1123
https://doi.org/10.15407/mfint.45.09.1109
Reprints available directly from the publisher

PACS numbers: 06.60.Vz, 43.35.+d, 62.80.+f,, 81.65.-b, 81.70.Bt, 81.70.Cv, 83.85.Vb

Ultrasonic Impact Treatment: Assessing the Process Energetics

S. P. Chenakin, B. M. Mordyuk, N. I. Khripta, and V. Yu. Malinin

G. V. Kurdyumov Institute for Metal Physics, N.A.S. of Ukraine,
36 Academician Vernadsky Blvd.,
UA-03142 Kyiv, Ukraine

A comparative study of process energetics is carried out for two loading schemes being used in ultrasonic impact treatment of materials, namely, a single-pin normal impacting mode and a multipin sliding/shearing impacting mode involving a low-frequency reciprocating motion of the sample. The maximum kinetic energy (or velocity) and frequency of stochastic oscillations of pins are measured experimentally for both loading modes at ultrasonic horn amplitudes varying in the range from 16 μm to 28 μm. Accordingly, a number of impact parameters such as impact time, maximum impact force, maximum impact stress, energy density and power density injected per impact in the contact area, total energy and power densities deposited in the sample (ZrTiNb alloy in this case) during treatment time are assessed. Variation of these impact characteristics is considered for both modes as a function of the ultrasonic horn amplitude, number of pins in the impact head (in sliding mode), pins' dimensions and material of the sample. The effect of amplitude and frequency of reciprocating sample holder in sliding impact mode on the total energy density deposited across the sample surface is analysed. The evaluated parameters are expected to be helpful in understanding the impact treatment-induced changes in physicochemical characteristics of various materials.

Key words: ultrasonic impact treatment, pin velocity, pin impact frequency, impact parameters, ZrTiNb alloy

Проведено порівняльне дослідження енергетики процесу для двох схем навантаження, які використовуються в ультразвуковому ударному обробленні матеріялів, а саме, для: нормального ударного режиму з одним биком і режиму ковзного/зсувного удару кількома биками із низькочас-

Corresponding author: Sergiy Petrovych Chenakin
E-mail: chenakin@imp.kiev.ua

Citation: S. P. Chenakin, B. M. Mordyuk, N. I. Khripta, and V. Yu. Malinin, Ultrasonic Impact Treatment: Assessing the Process Energetics, *Metallofiz. Noveishie Tekhnol.*, **45**, No. 9: 1109–1123 (2023). DOI: 10.15407/mfint.45.09.1109

тотним зворотньо-поступальним рухом зразка. Експериментально виміряно максимальну кінетичну енергію (або швидкість) і частоту стохастичних коливань бияків для обох режимів навантаження за амплітуд коливання ультразвукового концентратора в діяпазоні від 16 мкм до 28 мкм. Відповідно, проведено оцінку ряду параметрів удару, таких як час удару, максимальна сила удару, максимальне ударне напруження, густина енергії та густина потужности, що акумулюються під час удару у зоні контакту, та загальні густини енергії й потужности, що передаються зразку (стопу ZrTiNb в даному випадку) за час ударного оброблення. Розглянуто варіяції цих ударних характеристик для обох режимів оброблення в залежності від амплітуди ультразвукового концентратора, кількости бияків в ударній голівці (у режимі ковзного удару), розмірів бияків і матеріялу зразка. Проаналізовано вплив амплітуди та частоти зворотньо-поступального руху утримувача зразка в режимі ковзного удару на загальну густину енергії, що акумулюється на поверхні зразка. Очікується, що оцінені параметри уможливлять зрозуміти зміни фізико-хемічних характеристик різних матеріялів, спричинені ударним обробленням.

Ключові слова: ультразвукове ударне оброблення, швидкість бияка, частота ударів бияка, енергетичні параметри удару, стоп ZrTiNb.

(Received 27 April, 2023; in final version, 25 May, 2023)

1. INTRODUCTION

To date, a number of various techniques for modifying the surface of materials have been proposed, in particular, methods that provide surface severe plastic deformation (SSPD). These methods inducing grain refinement, generating compressive residual stresses, affecting the surface roughness and modifying the surface chemical state are being leveraged to produce materials with superior surface integrity and excellent properties, which have found their application in different fields. In order to opt for an appropriate method to be employed for surface modification, it is necessary to understand the similarities and differences as well as the limitations and advantages of the processes underlying the SSPD methods by comparing the effect of treatment parameters on the materials' structure and properties.

A comparative study [1] of effects of conventional shot peening (SP) and surface mechanical attrition treatment (SMAT) of a 316L stainless steel performed with the same Almen intensity and the same coverage revealed that SP resulted in a higher fatigue life under low strain amplitude, but lower fatigue life under high strain amplitude as compared to the SMATed samples. A numerical simulation of the SP and SMAT processes [2] shows that under the same impact kinetic energy, the SP-induced plastic strain rate is larger than that of SMAT and, for the same coverage, the grain refinement caused by severe SP (SSP) is, accordingly, stronger than that by SMAT, whereas SMAT induces

larger compressive residual stresses and much smaller surface roughness than SP. SMAT with multiple shot incidence angles and shot oblique impacts is found to be more efficient for surface compressive residual stresses and grain refinement as compared to SP with shot incidence angle of 90°. When compared to laser shock peening (LSP), SP of a 316L steel was observed [3] to bring about larger work hardening, surface roughening and residual compressive stress levels because of a more severe surface loading; at the same time, LSPed sample exhibited a better pitting corrosion resistance. Ultrasonic impact peening (UIP) of a 316L stainless steel with a peening needle having a semi-ellipsoid tip [4] and UIP of an AISI 321 stainless steel with a disk-shaped flat pin [5] was shown to also produce a much higher level of the compressive residual stress, appreciably stronger work hardening and much smaller grain size than LSP.

Gill *et al.* [6] employed LSP, cavitation peening (CP) in air and water and ultrasonic nanocrystal surface modification (UNSM) with a WC ball tip under different loads to improve properties of Inconel 718 superalloy. UNSM was found to provide the highest increase in hardness and the highest level of residual compressive stress due to higher plastic deformation as compared to CP and LSP. The observed differences in roughness, hardness, residual stresses and microstructure induced by all three peening techniques were shown to be dependent on the way the plastic deformation takes place. Maleki *et al.* [7] also found UNSM to be the most efficient method in improving the mechanical properties of Inconel 718 in comparison with SSP and LSP, giving rise to the strongest increase in the surface hardness, largest average depth of the affected layer, highest level of residual compressive stress, longest fatigue life and strongest grain refinement followed by SSP and LSP. By comparing the effects of LSP, water jet cavitation peening (WjCP), water jet shot peening (WjSP), and multipin ultrasonic impact treatment (UIT) on AISI 304 stainless steel, Lesyk *et al.* [8] determined the optimal treatment regime for each technique that provided maximum surface hardness and compressive residual stress along with minimum surface roughness. The strongest work hardening and maximum reduction in roughness parameter attained by each method were obtained to decrease in the sequence UIT > WjSP > WjCP > LSP. Soyama demonstrated [9] that treatment of a 316L stainless steel by using water jet peening (WjP), CP, SP, and LSP with an optimum coverage improved the fatigue performance of the steel, with the highest fatigue strength/fatigue life being obtained with CP/SP followed by SP/CP, LSP and WjP and closely related to Vickers hardness/residual stress and the surface roughness. The effects of SP, SMAT, LSP, UNSM and surface mechanical rolling treatment (SMRT) on the fatigue properties of metals and their dependence on the surface finish, microhardness, residual stress and microstructure of the treated materials were reviewed

and compared by Rui Chen *et al.* [10]. To understand comprehensively the effects caused by the various peening methods and compare quantitatively their effectiveness, impact velocities/energies and strain rates were assessed for SMAT [11], SP and SMAT [2], SP, CP and LSP [12].

As distinct from other ultrasonically assisted peening techniques such as UIP (using a needle-shaped striker connected to an ultrasonic horn) [4], UNSM (using WC, Al_2O_3 or Si_3N_4 ball tip pressed by a horn) [6, 7] or SMAT (using a large number of steel balls as strikers) [2, 11], UIT devices convert ultrasonic energy into multiple stochastic impacts of an intermediate element (pin or pins) freely oscillating with a high velocity in the gap between the ultrasonic horn tip and the treated surface. In our laboratory, two different loading schemes are being used for UIT of materials, namely, single-pin normal impact mode and sliding/shearing multipin mode [13]. The energy of pins in the UIT process is a key parameter determining the strain rate, which plays a crucial role in the plastic strain-induced phenomena occurring both on the surface (*e.g.*, oxidation [14], nitriding [15], hardening [14, 16], *etc.*) and in the subsurface layers (residual stress accumulation and grain refinement [13, 16]). However, in previous UIT-related papers only tentative values of energy parameters based on some general conceptions were used. In a recent work [17], we performed a comparative study of the impact energy effects of the two UIT loading schemes on the structural state, surface chemical and phase composition, roughness, microhardness, and corrosion properties of a Zr–31Ti–18Nb alloy. In the present work, we explore the energetics of both UIT loading modes and evaluate a number of energy parameters as a function of experimental conditions that can affect the treatment process and can be useful for understanding the differences in the UIT-induced alterations.

2. EXPERIMENTAL

The instrument for UIT comprises a piezoceramic transducer with an ultrasonic horn. The ultrasonic horn driven by a 1 kW ultrasonic generator and vibrating with a frequency of 21 kHz transfers its kinetic energy to the sample via repetitive impacts by the pin/pins positioned between the horn flat tip and the sample surface. Before processing, the ultrasonic system is typically pressed against the sample at a static load of 50–90 N. In this case, the total energy applied to the material is the sum of the static energy imposed by the pressed ultrasonic device and the dynamic energy resulting from the ultrasonic vibration [6].

In one loading scheme, a single disk-shaped pin obtaining its energy from the ultrasonic horn produces repetitive normal impacts on the unconstrained sample placed in the holder on a supporting disk, so that the sample experiences mainly compressive (axial) deformation, with the radial expansion being small (Fig. 1, *N*). We call this scheme the

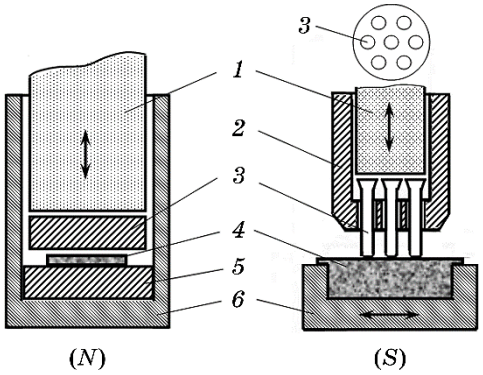

Fig. 1. Ultrasonic impact treatment schemes: single-pin normal impact loading mode (*N*) and sliding/shearing multi-pin impact loading mode (*S*): *1*—vibrating ultrasonic horn, *2*—impact head, *3*—pins, *4*—sample, *5*—bearing steel disk support, *6*—sample holder.

single-pin normal impact-loading mode (denoted for brevity *N*). This mode was used, *e.g.*, for UIT of AISI 321 stainless steel [5, 18] and Zr–Ti–Nb alloy [19]. In a modified version of this loading scheme [14, 15, 20], the (constrained) sample is fitted into a cylindrical pit in the sample holder and experiences only axial deformation.

In the other loading scheme [8, 13, 16, 21], a special impact head with seven rod-like pins is mounted on the horn tip (Fig. 1, *S*). When the ultrasonic vibrations are switched on, the pins start to oscillate stochastically in the gap formed between the horn tip and sample surface. Besides, during UIT in this mode, the sample holder reciprocates with a frequency f_s and amplitude A_s, which can be independently adjusted. Under such conditions, the pins would produce repetitive sliding impacts on the sample surface. Accordingly, we call this processing scheme the sliding/shearing multipin impact-loading mode (for brevity, referred to as mode *S*).

To assess the energetics of the impact treatment process, we need to know the kinetic energy/velocity of the pin/pins and the frequency of its/their oscillations. The vibration frequency f_{uh} and amplitude A_{uh} of ultrasonic horn tip are the main parameters that determine the maximum vibration velocity ($V_{uh} = 2\pi f_{uh} A_{uh}$) and acoustic pressure, which is created nearby the horn tip and is considered the main driving force to propel pins to a maximum velocity.

For measuring kinetic energy acquired by the pin, we used an approach similar to that employed for evaluation of the maximum impact velocities of balls during SMAT [11] and SP [12] processes. Accordingly, we mounted an experimental set-up with an acoustic system that was positioned vertically, and the pins which are being used in modes *N* and *S* were placed on the top of the horn tip (Fig. 2, *a*). Upon switching

on the ultrasonic vibration, the pin leapt up to a certain attitude. These leaps were filmed by a high-speed camera (Nickon Coolpix 4500) to capture the upward motion of the pins. By choosing an appropriate frame, we could measure the maximum height h reached by the pin. As an example, Fig. 2 shows the frames fixing the highest attitude attained by one (Fig. 2, *b*) and three rod-like pins (Fig. 2, *c*) being used for UIT in sliding (S) mode and by a disk-shaped pin (Fig. 2, *d*) being used in normal (N) mode. Since the maximum height of the pin rise depended on the ultrasonic horn amplitude setting, prior to the experiments, the actual amplitude of the ultrasonic horn tip was measured by using a non-contact piezoceramic vibrometre AVM-4M. The maximum kinetic energy acquired by the pin from the vibrating horn tip at different A_{uh} was determined from its equality to the potential energy of the pin at the highest attitude $E = mgh$, where m is the mass of the pin, g the acceleration of gravity.

In order to evaluate the frequency of impacts of oscillating pins, we performed additional experiments in which the gaps between the sample surface and vibrating ultrasonic horn produced by oscillating pins were measured for different A_{uh}. As an example, Figs. 2, *e* and *f* show frames of the loading unit with marked gaps formed during UIT processing of the sample in modes S and N, respectively. Actually, the gap size should correspond to the maximum path of the pin striking the sample surface. However, the pin might fly a shorter distance than the established gap since the pins' path would depend on occasional collisions between the vibrating horn tip and the rebounding pin (horn tip may either accelerate or decelerate the pin). Despite the random char-

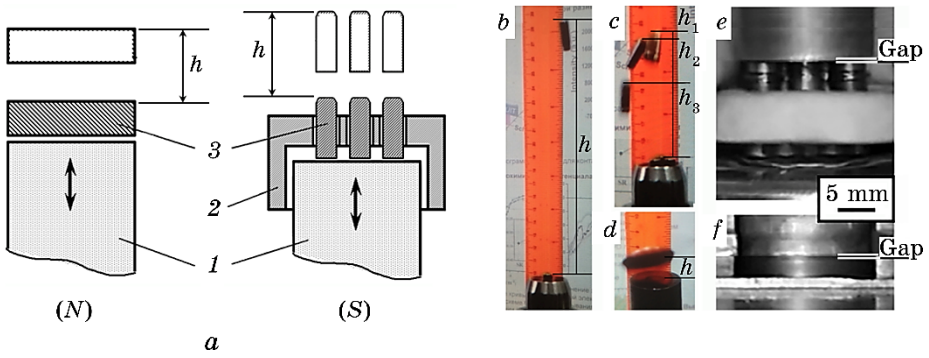

Fig. 2. Schematics (*a*) of the experimental setup for measuring the kinetic energy of pins in modes N and S. The frames taken by a high-speed camera show the maximum height h of rise of the pins upon switching on the vibrations of the horn tip in modes S (*b*—one-pin set, *c*—three-pin set) and N (*d*). The gaps formed by oscillating pins between the sample surface and vibrating ultrasonic horn are shown in frames for modes S (*e*) and N (*f*).

acter of the energy obtained by the pin from the horn and regardless of the pins' rebound distance, the energy transfer efficiency at any moment of the horn–pin collision and, accordingly, the magnitude of the acquired kinetic energy of the pin are expected to be always high due to the high vibration frequency of the horn tip (21 kHz). In a stationary process, the frequency f_p of stochastic oscillations of the pin can be estimated from the size A_g of the formed gap and the maximum velocity V_p of the pin as $f_p = V_p/2\pi(A_g/2)$.

A foil of a Zr–31Ti–18Nb alloy 4 mm thick served as a sample for a comparative study of the effect of impact treatment energy deposited in two loading modes N and S. In the present experiments, a disk-shaped pin used for UIT in mode N had a mass of 6.04 g and was 17.5 mm in diameter and 2.8 mm thick. All rod-like pins used for impact processing in mode S had a mass of 2.2 g and were 4.9 mm in diameter and 14.9 mm long. All the pins were made of hardened bearing steel ШХ-15 (analogue of AISI52100) with the composition in wt.%: 1.5 Cr, 1 C, 0.5 Cu + Ni, 0.3 Mn, 0.25 Si, < 0.02 S, balance Fe, $HB \cong 195$.

3. RESULTS AND DISCUSSION

As can be seen in Fig. 3, *a*, with increasing amplitude of the ultrasonic horn from 16 to 28 μm, the maximum kinetic energy E_p of the disk-shaped pin measured as described above (see Fig. 2, *a*, *d*) strongly increases from 0.89 ± 0.14 mJ to 3.55 ± 0.22 mJ (curve *1N*). Accordingly, the derived maximum velocity of the pin V_p changes from 0.54 to 1.08 m/s. The maximum kinetic energy of a rod-like pin measured in a set of one, three (see Fig. 2, *a*–*c*), five and seven pins increases with increasing A_{uh} more slowly than E_p (*1N*) and decreases with increasing the number of pins in the impact head (Fig. 3, *a*, curves *1S*–*7S*). In particular, E_p of the pin in the one-pin set increases with amplitude from 2.27 ± 0.09 to 3.09 ± 0.12 mJ (curve *1S*), and E_p imparted to one pin in a seven-pin set changes from 0.26 ± 0.07 to 0.36 ± 0.08 mJ (V_p changes from 0.49 to 0.57 m/s) (curve *7S*). Note that in the range of A_{uh} from 16 to 23 μm the kinetic energy of one pin (or total E_p of all pins) being used in mode S is higher than E_p of the pin being used in mode N, whereas at an amplitude of 28 μm E_p of the pin in mode N exceeds that in mode S (Fig. 3, *a*).

The variation of the size of the gap A_g between the sample surface and vibrating ultrasonic horn measured for the set of three, five and seven pins in mode S and for one pin in mode N is presented in Fig. 3, *b* as a function of the horn amplitude. It shows that, at A_{uh} greater than $\cong 10$ μm, the gap produced in mode N becomes larger than that in mode S. The most probable frequency f_p of impacts of oscillating pins in modes N and S derived from the gap size A_g and the maximum pin velocity V_p is shown in Fig. 3, *c* as a function of A_{uh}. It can be seen that in

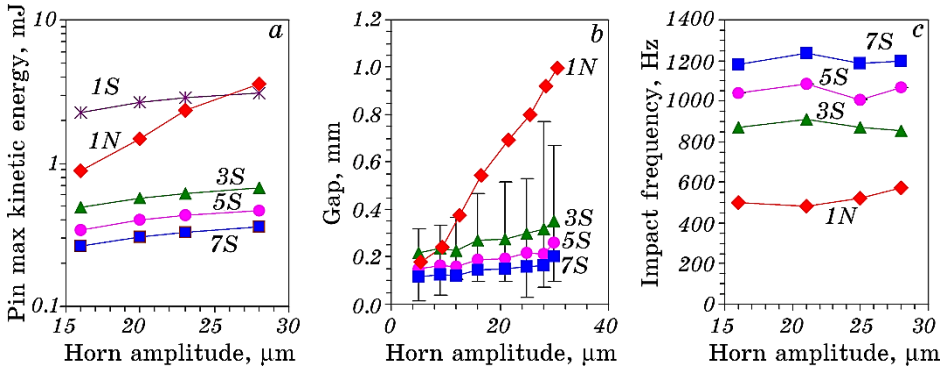

Fig. 3. Variation of maximum kinetic energy of pins (*a*), size of the gap formed between the ultrasonic horn tip and the sample (*b*) and frequency of impacts of oscillating pins (*c*) being used for processing in the normal impact mode (*N*) and sliding impact mode (*S*) as a function of amplitude of the ultrasonic horn. The labelling of the curves indicates the number of pins and the processing mode.

the range of amplitudes from 16 to 28 μm, the average f_p is practically independent of A_{uh} and is estimated to be 520 ± 64 Hz for the pin in mode *N* and 875 ± 192 Hz, 1050 ± 233 Hz, and 1200 ± 267 Hz for three, five and seven pins, respectively, in mode *S*. The obtained frequencies of impacts suggest that the mechanical processing with the given UIT devices can actually be specified as ultrasonically driven high-frequency mechanical impact (HFMI) treatment.

By making use of the experimentally determined values of E_p, V_p and f_p, we evaluated a number of energy parameters that can affect the treatment process and can be suitable for comparison of the UIT-induced alterations under both loading schemes.

Let us define the quantity E_r [J·s^{-1}] $= E_p f_p$ as the energy deposition rate. Then the total maximum mechanical energy transferred to the sample during UIT for time t amounts to E_m [J] $= E_r t = E_p f_p t$.

Under the same impact kinetic energy E_p, the intensity of impact load and, accordingly, its effect will depend on the contact area between the pin and the target surface [2]. The expression E_0 [J/cm^2] $= E_p/S$, where S is the impact spot area, represents the specific peak energy density deposited in an impact. Then, E_i [J·s^{-1}·cm^{-2}] $= E_0 f_p = E_r/S = E_p f_p/S$ will describe the impact energy intensity in the contact area or the specific energy deposition rate in the impact spot area, with the total energy deposited in the impact area during UIT being E_t [J/cm^2] $= E_i t = E_0 f_p t$.

The peak power density injected per impact in the contact area can be defined as P_0 [W/cm^2] $= E_p/(\tau S)$, where τ is the duration of a single impact. Then, the total mechanical power applied to the contact area of

the material during UIT is described as $P_t\,[\mathrm{W/cm^2}] = P_0 f_p t$.

The impact time can be derived from Newton's second law as $\tau = m_p \Delta V_p / F$, where m_p is the mass of a pin, ΔV_p the change of the pin velocity during impact (from max to 0), F the maximum impact force of a pin. The latter can be evaluated according to an energy model of impact [22] as $F = V_p (m_p k_s / (1 + k_s/k_p))^{1/2}$; here, $k_s = E(\mathrm{s}) S_s / l_s$ and $k_p = E(\mathrm{p}) S_p / l_p$ stand for the stiffness of the sample and the pin, respectively, with E(s), E(p) being the elastic moduli (59 GPa for the Zr31Ti18Nb sample and 211 GPa for the ШХ-15 bearing steel pins), S_s, S_p the cross-sectional areas and l_s, l_p the lengths of the sample and the pin. For a given set of pins and a sample, the maximum impact force in the normal impact mode in the range of A_{uh} from 16 to 28 μm was estimated to grow from 1468 ± 581 to 2936 ± 949 N. This is significantly larger than F in the sliding impact mode, which decreases with increasing number of pins and changes, *e.g.*, from 466 ± 53 to 544 ± 62 N, when using 3 pins, and from 341 ± 39 to 398 ± 45 N for 7 pins. Accordingly, the impact time τ was evaluated to be 2.13 ± 1.05 μs in mode N and 3.83 ± 1.31 μs in mode S (for any number of pins).

As can be seen in Fig. 4, *a*, the evaluated energy deposition rate E_r increases with increasing A_{uh} and with increasing number of pins in mode S, in this mode, E_r is significantly larger than that in mode N. The impact energy density E_0 deposited in the contact area also increases with increasing horn amplitude but, on the contrary, decreases with increasing number of pins in mode S, in mode N, E_0 is higher than that in 7-pin mode S in the entire range of A_{uh} (Fig. 4, *b*). Like E_0, the

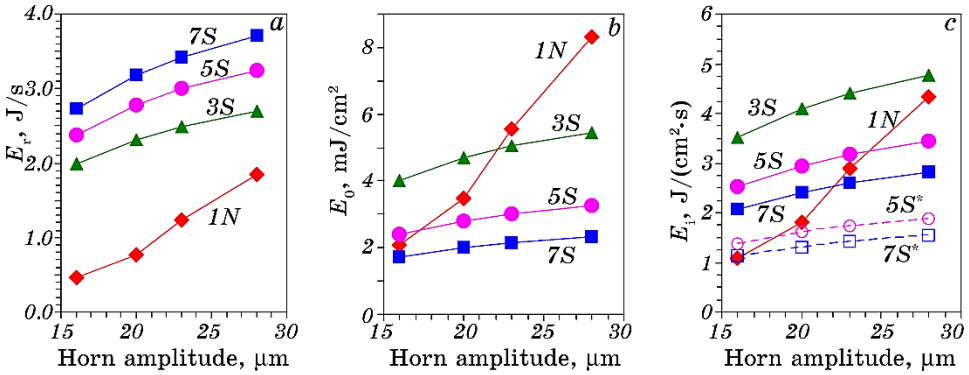

Fig. 4. Variation of energy deposition rate E_r (*a*), peak energy density deposited in an impact spot area E_0 (*b*) and impact energy intensity in the contact area E_i (*c*) during processing in the normal impact mode (N) and sliding impact mode (S) as a function of amplitude of the oscillating ultrasonic horn. The labelling of the curves indicates the number of pins and the processing mode. The dashed-line curves $5S^*$ and $7S^*$ shown in (*c*) represent the impact intensity E_i corrected for reciprocating motion of the sample in 5- and 7-pin mode S.

impact load intensity in the contact area E_i increases with A_{uh} and decreases with number of pins but in mode N; E_i appears to be larger that this is in 7-pin mode S only at amplitudes above 23 μm (Fig. 4, *c*).

The specific power density P_0 injected per impact in the contact area rises with A_{uh} and decreases with increasing number of pins in mode S, at amplitudes above 16 μm, P_0 in mode N appreciably exceeds that in mode S for 3, 5 and 7 pins (Fig. 5, *a*). Specifically, P_0 rises from 0.98 to 3.91 kW/cm^2 in mode N and from 0.45 to 0.61 kW/cm^2 in 7-pin mode S. As compared to P_0, the total power density P_t evaluated for the impact treatment time $t = 2$ min (which was found [14, 15, 17, 19] to be optimal in UIT of different materials) demonstrates enhanced values in mode S (due to a higher f_p) so that P_t in mode N becomes larger than that in 3-, 5- and 7-pin mode S only at $A_{uh} > 23$ μm (Fig. 5, *b*). Specifically, in mode N, P_t rises with A_{uh} from 61.0 to 244.2 MW/cm^2 and in 7-pin mode S from 64.7 to 88.1 MW/cm^2. Note that the total mechanical energy E_m transferred to the sample and the total energy density E_t deposited in the impact area evaluated for $t = 2$ min change with A_{uh} qualitatively in the same way as E_r and E_i, respectively (*cf.* Fig. 4, *a* and *c*), differing from E_r and E_i by a factor of t.

The maximum impact stress arising in the sample section, $\sigma_{max} = F/S$, can be estimated [22] as $\sigma_{max} = V_p\{3\rho_s E(s)\}^{1/2}$, where ρ_s is the sample density (6346 kg/m^3 for Zr31Ti18Nb alloy). It can be seen in Fig. 5, *c* that σ_{max} increases with increasing A_{uh}, and decreases with increasing number of pins in mode S, at $A_{uh} > 16$ μm, σ_{max} in mode N exceeds that in 7-pin mode S.

In evaluating the energy characteristics such as P_t and E_t integrated

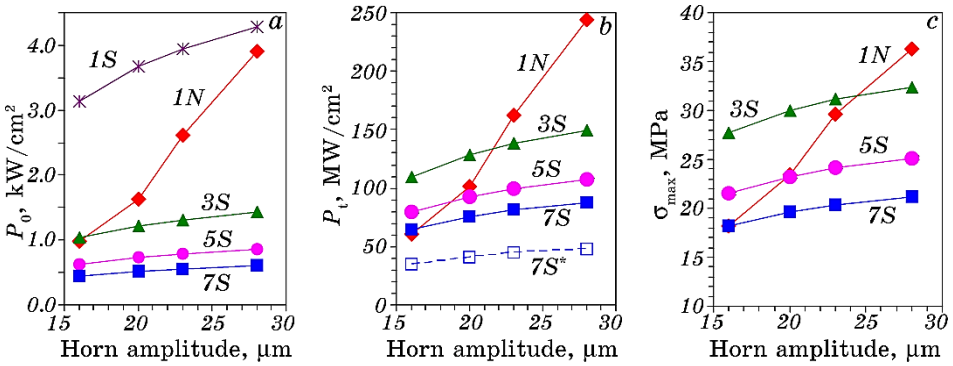

Fig. 5. Variation of impact power density P_0 injected in the contact area (*a*), total power density P_t deposited during UIT for 2 min (*b*) and maximum impact stress σ_{max} in the sample section (*c*) produced in the normal impact mode (*N*) and sliding impact mode (*S*) as a function of amplitude of the ultrasonic horn. The labelling of the curves indicates the number of pins and the processing mode. The dashed-line curve $7S^*$ shown in (*b*) represents P_t corrected for reciprocating motion of the sample in 7-pin mode S.

over the treatment time t, reciprocating motion of the sample holder during UIT in mode S has to be taken into account. Figure 6 shows an ideal model representation of imprints produced by impacts of oscillating pin ($f_p = 1200$ Hz) across the sample during a half-period of its reciprocating displacement with $f_s = 20$ Hz and amplitude A_s of 8 mm (*a*) and 12 mm (*b*). One can see that within the sample boundaries, the number Y_n of overlapped areas S_n of the pin imprints with a particular number n of impacts in the area as well as the number of impacts n in a particular overlapped area decrease with increasing A_s (*e.g.*, $Y_n = 22.5$, $n_{max} = 9$ for $A_s = 8$ mm and $Y_n = 15$, $n_{max} = 6$ for $A_s = 12$ mm).

Sample reciprocation results in a decrease in the density of deposited energy and its non-uniform distribution, with the E_t and P_t decreasing from the central part to the periphery (*cf.* Fig. 6). Besides, due to sample displacement, the just-impacted area would not be hit again in $1/f_p$ seconds and would have more time for relaxation. To correct the energy parameters for reciprocating motion of the sample, we evaluated the total energy densities E_t^* and P_t^* deposited across the sample surface by taking into account the number Y_n of overlapped areas S_n of the pin imprints and the number n of impacts in these overlapped areas as:

$$E_t^* = 2f_s t \sum_{n=1}^{n_{max}} \frac{S_n}{S_p} nE_0 Y_n = 2E_0 Y_{n_{max}} f_s t\,, \quad P_t^* = 2f_s t \sum_{n=1}^{n_{max}} \frac{S_n}{S_p} nP_0 Y_n = 2P_0 Y_{n_{max}} f_s t\,.$$

The dashed line curves $5S^*$ and $7S^*$ in Fig. 4, *c* and curve $7S^*$ in Fig.

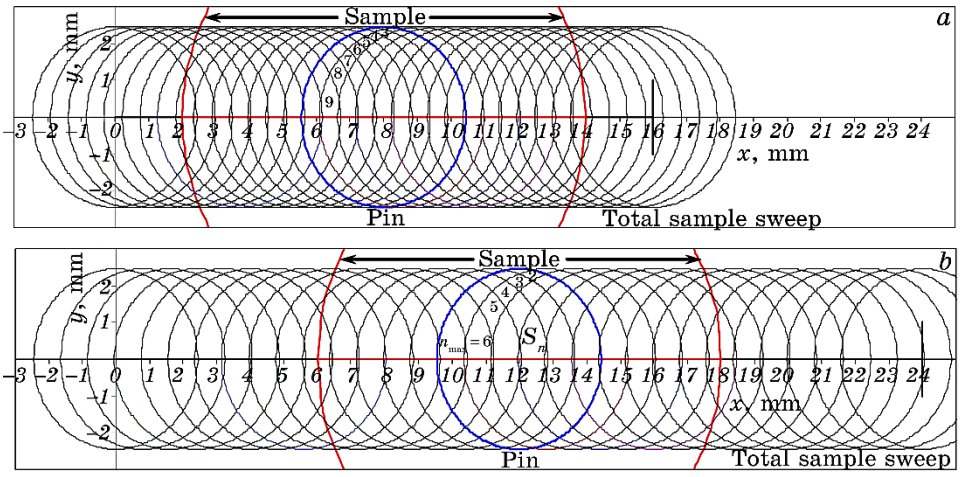

Fig. 6. Ideal representation of imprints produced in mode S by the pin impacts on the sample during a half-period of its reciprocating displacement with $f_s = 20$ Hz and amplitude A_s of 8 mm (*a*) and 12 mm (*b*) for $f_p = 1200$ Hz. Numerical characters (in italic) indicate the number n of impacts in particular overlapped areas S_n.

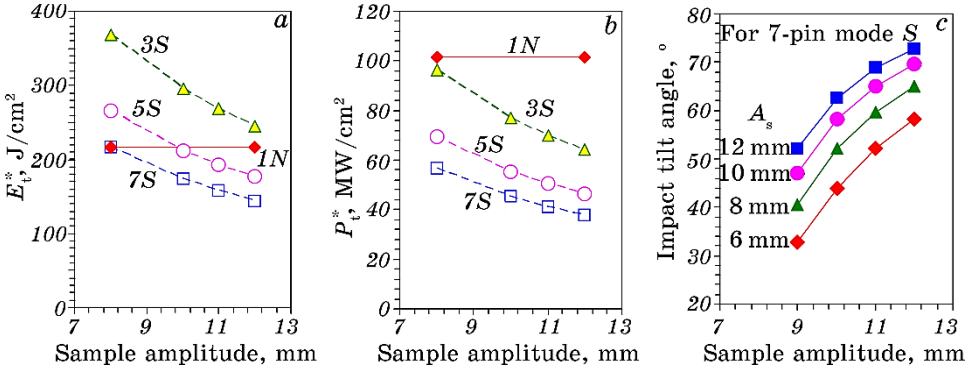

Fig. 7. Variation of corrected total energy density E_t^* (*a*) and corrected total power density P_t^* (*b*) deposited during UIT for 2 min as a function of the sample shift amplitude A_s at $A_{uh} = 20$ μm. The labelling of the curves indicates the number of pins and the processing mode. Variation of the pin impact tilt angle (*c*) as a function of the sample shift frequency f_s for different sample shift amplitudes A_s in 7-pin mode at $A_{uh} = 20$ μm.

5, *b* represent the variation of respectively impact energy density E_i^* and total power density P_t^* corrected for reciprocating motion of the sample in 5- and 7-pin mode with $f_s = 20$ Hz and $A_s = 11$ mm as a function of horn amplitude. Note that the sample shift frequency f_s do not affect the impact energy parameters, whereas the sample shift amplitude A_s does. As can be seen in Fig. 7, the total energy density E_t^* (*a*) and the total power density P_t^* (*b*) deposited across the sample during $t = 2$ min decrease with increasing A_s.

Note also that a pin impinging normally on a reciprocating sample would experience a tilt by an angle determined by the ratio between the normal (pin) and lateral (sample) velocity components. Accordingly, the impact tilt angle β (with respect to the surface normal) will decrease with increasing A_{uh} (or pin kinetic energy) and increase with increasing number of pins. Specifically, with increasing A_{uh} from 16 to 28 μm the evaluated tilt angle of the pin in a 7-pin set striking the sample reciprocating with $f_s = 10$ Hz and $A_s = 10$ mm changes from 49 to 45°, at $A_{uh} = 20$ μm, β amounts to 35, 42 and 47° for 3-, 5- and 7-pin set, respectively. Besides, β will increase with increasing the sample shift frequency f_s and amplitude A_s (Fig. 7, *c*). One can speculate that tilting of the pin would decrease the impact contact area and thus increase the deposited energy and power densities E_t^*, P_t^*. On the other hand, the decrease in the contact area would decrease overlapping of the pin imprints, thus reducing E_t^* and P_t^* so that the possible effect of pin tilting on the actual energy density deposition cannot be definitely specified.

The impact energy parameters can be adjusted by changing not only the amplitude of ultrasonic horn and the treatment time but also the

pin dimensions (diameter, length, mass, material), which define the pin energy/velocity as well. The data presented in Table 1 show that the magnitudes of P_0 and σ_{max} evaluated, as an example, for two types of pins being typically used in UIT are smaller and impact time τ is longer for larger (heavier) pins impacting the same ZrTiNb sample in both modes at the same $A_{uh} = 20$ μm. One can also see that the impact parameters evaluated for different samples (ZrTiNb, TiAlV, steel) of the same size are also dependent on the target material.

Ultrasonic impact treatment of a CrCoNi coating performed for 2 min with different amplitudes (0, 10, 15 and 20 μm) has shown [23] that depth of the impacted layer, microhardness, refinement of the top grains and wear resistance of the coating increase with increasing horn amplitude that can be related with a corresponding augmentation of different energy parameters evaluated in our study (*cf.* Figs. 4, 5). A greater extent of deformation-induced oxidation, stronger structural alterations, higher microhardness and corrosion resistance observed for ZrTiNb alloy after UIT for 2 min at $A_{uh} = 20$ μm in mode *N* as compared to 7-pin mode *S* were shown [17] to also correlate well with parameters E_0, P_0, E_t, P_t, and σ_{max} which were evaluated to be larger for mode *N*. Such a correlation implies that the treatment-induced enhancement of different properties of materials is greatly determined by the energy density accumulated in the impact area during UIT.

By definition, integral parameters E_t and P_t should increase linearly with processing time *t*. However, in practical UIT, the dependence of physicochemical characteristics of materials on *t* generally is not linear. In particular, both monotonic (but non-linear) and non-monotonic variation of microhardness, surface roughness, residual stress level,

TABLE 1. Evaluated impact treatment parameters of different alloys for two loading schemes (single-pin normal '*N*' and multi-pin sliding '*S*') and two pins' dimensions at $A_{uh} = 20$ μm. Pins' dimensions in mode *N*: *a*—dia = 17.5 mm, $l = 2.8$ mm, $m = 6.035$ g, *b*—dia = 19.0 mm, $l = 5.0$ mm, $m = 10.444$ g, pins' dimensions in mode *S*: *c*—dia = 4.9 mm, $l = 14.9$ mm, $m = 2.203$ g, *d*—dia = 5.2 mm, $l = 15.0$ mm, $m = 2.632$ g.

Energy parameter	Impact power density P_0, kW/cm^2 (τ, μs)				Impact stress σ_{max}, MPa			
Pins-Mode/Sample	1-*N*	3-*S*	5-*S*	7-*S*	1-*N*	3-*S*	5-*S*	7-*S*
Zr31Ti18Nb[a, c]	1.63[a] (2.13)	1.22[c] (3.83)	0.73[c]	0.52[c]	23.5	30.0	23.2	19.6
AISI-321 steel, [c]	1.90 (1.83)	1.38 (3.39)	0.83	0.59	47.7	61.0	47.3	39.9
Ti6Al4V[a, c]	1.79 (1.94)	1.32 (3.55)	0.79	0.57	27.3	34.8	27.0	22.8
Zr31Ti18Nb[b, d]	1.01[b] (3.42)	1.04[d] (4.0)	0.62[d]	0.45[d]	17.8	27.4	21.3	18.0

α-martensite fraction, corrosion resistance and oxide layer thickness was observed in the range of impact treatment times up to 150, 240 and 360 s for different materials such as Zr–2.5%Nb [24], Ti6Al4V [14, 15], α-Ti, AISI 321 steel [16, 18], AISI 304 steel [8], AISI D2 tool steel [21]. Therefore, when comparing the effectiveness of different treatment methods and effects of different treatment parameters, it appears reasonable to consider 'instantaneous' impact energy characteristics (E_0, E_i, P_0, σ_{max}) rather than integral ones (E_t, P_t), unless a linear variation of some materials characteristics in the studied processing time interval is obtained.

4. CONCLUSIONS

The maximum kinetic energy E_p (or velocity V_p) and frequency f_p of stochastic oscillations of pins being used in impact treatment of materials under two loading schemes (single-pin normal N and multipin sliding/shearing S impact loading modes) have been experimentally assessed for ultrasonic horn amplitudes ranging from 16 to 28 μm. By making use of the determined values of E_p, V_p and f_p, a number of impact parameters, such as impact time τ, maximum impact force F, maximum impact stress σ_{max}, impact energy density E_0 and impact power density P_0 injected in the contact area, impact energy intensity in the contact area E_i, total energy density E_t and power density P_t deposited during treatment time, were evaluated. It was found that F, σ_{max}, E_0, E_i, E_t, P_0 and P_t increase with increasing horn amplitude and decrease with increasing number of pins used in mode S. The sample reciprocation in mode S was demonstrated to result in a decrease in the density of deposited energy and its non-uniform distribution across the sample, with the E_t and P_t decreasing with increasing the amplitude of the sample reciprocating motion. The evaluated impact parameters characterizing the energetics of treatment process appear to be suitable for comparison of UIT-induced alterations under different conditions and understanding of impact-induced changes in physicochemical characteristics of various materials.

REFERENCES

1. J. Zhou, D. Retraint, Z. Sun, and P. Kanouté, *Surf. Coat. Technol.*, **349**: 556 (2018).
2. C. Wang, C. Wang, L. Wang, Y. Lai, K. Li, and Y. Zhou, *Int. J. Adv. Manuf. Technol.*, **108**: 505 (2020).
3. P. Peyre, X. Scherpereel, L. Berthe, C. Carboni, R. Fabbro, G. Béranger, and C. Lemaitre, *Mater. Sci. Eng. A*, **280**: 294 (2000).
4. Z. D. Wang, G. F. Sun, Y. Lu, M. Z. Chen, K. D. Bi, and Z. H. Ni, *Surf. Coat. Technol.*, **385**: 125403 (2020).
5. B. N. Mordyuk, Yu. V. Milman, M. O. Iefimov, G. I. Prokopenko, V. V. Silberschmidt,

M. I. Danylenko, and A. V. Kotko, *Surf. Coat. Technol.*, **202**: 4875 (2008).
6. A. Gill, A. Telang, S. R. Mannava, D. Qian, Y.-S. Pyoun, H. Soyama, and V. K. Vasudevan, *Mater. Sci. Eng. A*, **576**: 346 (2013).
7. E. Maleki, O. Unal, M. Guagliano, and S. Bagherifard, *Mater. Sci. Eng. A*, **810**: 141029 (2021).
8. D. A. Lesyk, H. Soyama, B. N. Mordyuk, V. V. Dzhemelinskyi, S. Martinez, N. I. Khripta, and A. Lamikiz, *J. Mater. Eng. Perform.*, **28**: 5307 (2019).
9. H. Soyama, *J. Mater. Process. Technol.*, **269**: 65 (2019).
10. R. Chen, H. Xue, and B. Li, *Metals*, **12**: 642 (2022).
11. H. L. Chan, H. H. Ruan, A. Y. Chen, and J. Lu, *Acta Mater.*, **58**: 5086 (2010).
12. S. Kanou, O. Takakuwa, S. R. Mannava, D. Qian, V. K. Vasudevan, and H. Soyama, *J. Mater. Process. Technol.*, **212**: 1998 (2012).
13. B. N. Mordyuk and G. I. Prokopenko, *Handbook of Mechanical Nanostructuring* (Ed. M. Aliofkhazraei) (Wiley-VCH Verlag GmbH & Co: 2015), p. 417.
14. M. A. Vasylyev, S. P. Chenakin, and L. F. Yatsenko, *Acta Mater.*, **103**: 761 (2016).
15. M. A. Vasylyev, S. P. Chenakin, and L. F. Yatsenko, *Acta Mater.*, **60**: 6223 (2012).
16. B. N. Mordyuk and G. I. Prokopenko, *J. Sound Vibration*, **308**: 855 (2007).
17. S. P. Chenakin, B. N. Mordyuk, and N. I. Khripta, *Vacuum*, **210**: 111889 (2023).
18. B. N. Mordyuk, G. I. Prokopenko, M. A. Vasylyev, and M. O. Iefimov, *Mater. Sci. Eng. A*, **458**: 253 (2007).
19. S. P. Chenakin, B. N. Mordyuk, and N. I. Khripta, *Appl. Surf. Sci.*, **470**: 44 (2019).
20. S. P. Chenakin, V. S. Filatova, I. N. Makeeva, and M. A. Vasylyev, *Appl. Surf. Sci.*, **408**: 11 (2017).
21. D. A. Lesyk, S. Martinez, V. V. Dzhemelinskyy, A. Lamikiz, B. N. Mordyuk, and G. I. Prokopenko, *Surf. Coat. Technol.*, **278**: 108 (2015).
22. V. K. Manzhosov, *Modeli Prodol'nogo Vozdeystviya* [Models of Longitudinal Impact] (Ul'yanovsk: UlGT: 2006) (in Russian).
23. C. Wang, R. Li, X. Bi, W. Yuan, J. Gu, J. Chen, M. Yan, and Z. Zhang, *J. Mater. Res. Technol.*, **22**: 853 (2023).
24. B. N. Mordyuk, O. P. Karasevskaya, and G. I. Prokopenko, *Mater. Sci. Eng. A*, **559**: 453 (2013).

Metallophysics and Advanced Technologies
Металофіз. новітні технол.
Metallofiz. Noveishie Tekhnol.
2023, vol. 45, No. 9, pp. 1125–1139
https://doi.org/10.15407/mfint.45.09.1125
Reprints available directly from the publisher

PACS numbers: 06.60.Vz, 61.66.Dk, 61.72.Ff, 62.20.Qp, 81.07.Bc, 81.40.Cd, 83.60.Np

Impact of MHD-Processing on Technological Properties of High-Strength Casting Al–Cu Alloys

O. M. Smirnov, O. D. Rud*, V. N. Fikssen, Yu. P. Skorobagatko, T. O. Monastyrska*, M. S. Goryuk, A. Yu. Semenko, O. V. Yashchenko

Physico-Technological Institute of Metals and Alloys, NAS. of Ukraine,
34/1 Academician Vernadsky Blvd.,
UA-03142 Kyiv, Ukraine
**G. V. Kurdyumov Institute for Metal Physics, NAS. of Ukraine,*
36 Academician Vernadsky Blvd.,
UA-03142 Kyiv, Ukraine

Among many aluminium alloys, high-strength casting 'aluminium–copper' alloys are ones of the main structural materials in aircraft construction. According to the results of the latest research by specialists from different countries of the world, these alloys also have a perspective for application at manufacturing of parts (hulls and pistons) of engines for the aviation and automotive equipment. However, presence of toxic (cadmium) or expensive (silver) components in the composition of such alloys as strengthening additives limits significantly the potential of their industrial production and practical application. We propose using the energy of electromagnetic fields and magnetohydrodynamic (MHD) effects to process the alloy in liquid state. Implementation of such actions takes place in specialized casting magnetodynamic installation. The developed MHD processing of melts ensures refining of the structure and increasing main mechanical properties of aluminium alloys in the solid state. Actually, it is some kind of physical modifying without reagents. Regarding high-strength casting 'aluminium–copper' alloys, their MHD-processing in the liquid state in a foundry magnetodynamic installation allows to ensure quite high level of strength and plasticity even without application of strengthening additives. At the same time, the stand-

Corresponding author: Oleksiy Mykolayovych Smirnov
E-mail: alexey.smirnov55@gmail.com

Citation: O. M. Smirnov, O. D. Rud, V. N. Fikssen, Yu. P. Skorobagatko, T. O. Monastyrska, M. S. Goryuk, A. Yu. Semenko, and O. V. Yashchenko, Impact of MHD-Processing on Technological Properties of High-Strength Casting Al–Cu Alloys, *Metallofiz. Noveishie Tekhnol.*, **45**, No. 9: 1125–1139 (2023).
DOI: 10.15407/mfint.45.09.1125

ard-compliant level of the main technological properties (mainly fluidity and hot cracking susceptibility) is ensured. This indicates the possibility of obtaining thin-walled parts of complicated geometry from such alloys by casting methods. Further research will be focused on improving the mechanical and operational properties of experimental 'aluminium–copper' alloys due to the introduction of non-toxic and relatively cheap strengthening and modifying additives.

Key words: high-strength casting 'aluminium–copper' alloys, magnetohydrodynamic (MHD) processing, structure, strength, elongation, fluidity, hot cracking susceptibility.

Серед багатьох алюмінійових стопів саме високоміцні ливарні стопи системи «алюміній–мідь» є одними з основних конструкційних матеріялів у авіабудуванні. За результатами новітніх досліджень фахівців з різних країн світу ці стопи також мають перспективу щодо застосування для виготовленні корпусів і деталів двигунів авіаційної й автомобільної техніки. Однак наявність у складі таких стопів у якості зміцнювальних добавок токсичних (кадмій) або дорогих (срібло) компонентів істотно обмежує потенціял промислового виробництва їх і практичного застосування. Запропоновано використовувати енергію електромагнетних полів і магнетогідродинамічні (МГД) ефекти для оброблення стопу в рідкому стані. Реалізація таких дій відбувається у спеціялізованій ливарній магнетодинамічній установці. Розроблене МГД-оброблення розтопів забезпечує подрібнення структури та зростання основних механічних властивостей алюмінійових стопів у твердому стані та є фактично фізичним модифікуванням їх. Стосовно високоміцних ливарних стопів системи «алюміній–мідь», то МГД-оброблення їх у рідкому стані у ливарній магнетодинамічній установці уможливлює забезпечити достатньо високий рівень міцнісних і пластичних властивостей навіть без застосування зміцнювальних добавок. Цим способом забезпечується відповідний стандартам рівень основних технологічних властивостей (передусім рідкоплинности та схильности до утворення гарячих тріщин). Це свідчить про можливість одержання з таких стопів методами лиття тонкостінних деталів складної конфіґурації. Подальші дослідження будуть орієнтовані на підвищення механічних і експлуатаційних властивостей експериментальних стопів системи «алюміній–мідь» за рахунок введення нетоксичних і відносно дешевих зміцнювальних і модифікувальних добавок.

Ключові слова: високоміцні ливарні стопи системи «алюміній–мідь», магнетогідродинамічне (МГД) оброблення, структура, міцність, відносне видовження, рідкоплинність, схильність до утворення гарячих тріщин.

(Received 27 July, 2023; in final version, 5 August, 2023)

1. INTRODUCTION

The development of various branches of mechanical engineering necessitates the need to enhance the levels of mechanical, physical, techno-

logical, operational, and other properties of existing materials, particularly aluminium alloys widely used in the structures of modern machines and mechanisms for the production of high-tech equipment, primarily in aerospace, automotive, transportation, energy, and other industries. Therefore, the development of new technologies and equipment that will enable the practical implementation of these tasks is a relevant and promising direction for the advancement of science, technology, and industrial production.

Principal features of casting aluminium alloys are the unique combination of their physical properties (relatively low density), mechanical properties (high strength), and technological properties (for example, comparatively low preparation and casting temperatures), as well as their preference for operational temperature-time parameters (including cyclic strength). Most importantly, they offer the capability of obtaining complex-shaped parts through casting methods.

A special place is occupied by high-strength casting Al–Cu alloys, as they can compete with steels and titanium alloys in terms of specific strength (the strength-to-density ratio) can compete with steels and titanium alloys, and due to their significantly lower specific gravity, they have long been one of the main structural materials in the aircraft industry. On average, the total mass components from high-strength casting Al–Cu alloys in an aircraft amount to 300 kg, and in large aircraft, it can reach 2000 kg. Moreover, in recent years, developers, manufacturers, and consumers of such materials have been unsuccessfully striving to expand the scope of their application to the production of aircraft engine parts, both hull [1] and piston group [2, 3].

However, on this path, researchers and production workers have to solve a number of complex problems. For instance, the most common high-strength casting Al–Cu alloys include either the toxic element cadmium (AM4.5Cd alloy according to GOST 1583–93) [4, 5] or the expensive element silver [6] as a strengthening additive. Meanwhile, alloy counterparts without such additives exhibit significantly lower strength characteristics [6]. Moreover, due to the specific composition of these alloys (strict regulation of copper content within 4–5.5% by weight and silicon content not exceeding 0.2%) and in accordance with the state diagram of the Al–Cu system [7, 8], these materials have a wide solidification range. This leads to unsatisfactory casting properties, primarily low fluidity, and increased susceptibility to hot cracking during solidification, significantly limiting the ability to produce casings, especially thin-walled and critical components.

Therefore, experts worldwide strive to address these issues while ensuring environmental safety, economic feasibility, and relative technical and technological simplicity. These efforts are based on the development of new alloy compositions, melt preparation and out-of-furnace processing in the liquid state, the application of external phys-

ical effects, special casting methods, and heated modes [2, 3, 9–11].

In Ukraine, scientists from the Physical and Technological Institute of Metals and Alloys (PTIMA) and G. V. Kurdyumov Institute for Metal Physics (IMP) of the National Academy of Sciences of Ukraine have accumulated significant experience application of the energy of electromagnetic fields for processing casting aluminium alloys (both silumins and high-strength ones), with subsequent improvement of their structure and mechanical properties in the as-cast and heat-treated states [12–14].

2. EXPERIMENT PROCEDURE

At the first stage, the authors concentrated their efforts on the following research directions: 1) preparation of an experimental high-strength casting Al–Cu alloy, including the use of electromagnetic fields and magnetohydrodynamic (MHD) effects; 2) investigation of the structure and basic mechanical properties of the experimental alloy, comparing them with the properties of analogous alloys and requirements of the standards; 3) study of the main casting properties of the experimental alloy, particularly fluidity and susceptibility to hot cracking.

2.1. Features of Preparing the Experimental Alloy Using a Casting Magnetodynamic Installation

To verify the developed scientific approaches and technical solutions, an experimental batch (up to 100 kg) of an Al–Cu alloy was prepared, with its chemical composition in terms of major elements matching that of the most common high-strength aluminium casting alloys: AM4.5Kd (Ukraine) and A201 (USA) [6]. However, at this stage of the research, the experimental alloy did not include the strengthening additives typically present in standard alloys, such as the toxic cadmium or expensive silver. It should be noted that alloy analogues without such additives are known, such as AC1B (Japan) and A-U5GT (France) [6].

For the preparation of the experimental alloy, an experimental-industrial casting magnetohydrodynamic installation MDI-6A (Fig. 1) was used [12, 15].

The main function of the MDI is to provide the desired temperature of the liquid metal bath in the channel through adjustable induction heating, electromagnetic stirring by creating various modes of melt circulation (Fig. 2), perform controlled electromagnetic pouring of the liquid alloy into different metal receptacle, and, thus, technologically, the MDI functions as a mixer-batcher for liquid metal.

In obtaining the experimental alloy, two fundamentally new techno-

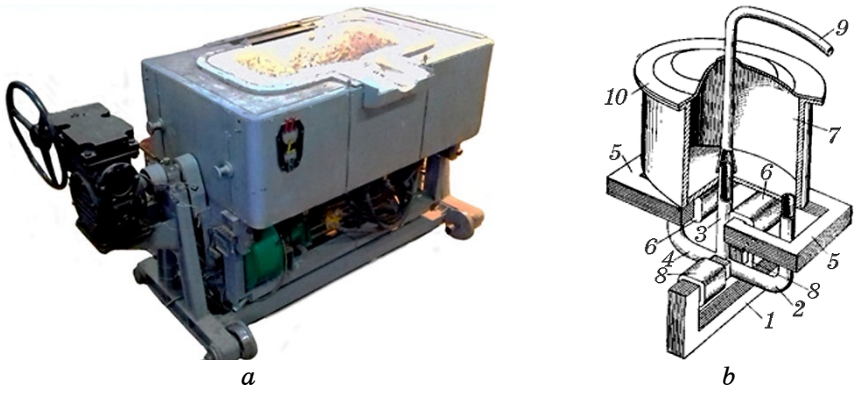

Fig. 1. External view (*a*) and general scheme (*b*) of the magnetohydrodynamic installation MDI-6A: *1*—crucible; *2*, *3*, *4*—branches of the induction channel; *5*—closed magnetic cores of the inductors; *6*—inductor coils; *7*—open magnetic core of the electromagnet; *8*—electromagnet coils; *9*—detachable metal duct; *10*—crucible cover.

logical schemes for processing aluminium melt in the MDI were employed. The first type of processing, the complex MHD thermal & forced one, is realized through physical factors, while the second type (complex refining) involves the use of refining reagents and corresponding technological equipment.

In the liquid metal filling the induction channel of the MDI, a variable electric current is generated (with a density of up to $20 \cdot 106$ A/m^2), as well as a variable magnetic field (up to 0.3 T) and a volumetric electromagnetic force (up to $60 \cdot 10^3$ N/m^3), which moves the molten metal in the form of a submerged jet from the channel into the liquid metal bath in the crucible. Electromagnetic pressure is also created in the channel (up to $2.5 \cdot 10^5$ Pa) and electromagnetic vibration at a frequency of 100 Hz, can occur a controlled pinch effect, which is the compres-

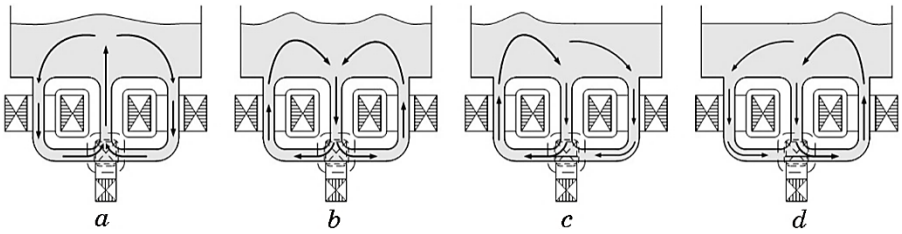

Fig. 2. Main schemes of melt circulation in the MDI under the influence of electromagnetic forces and MHD-effects: melt outflow mode from the central branch of the channel (*a*); melt suction mode into the central branch of the channel (*b*); mirror-symmetrical modes of lateral mixing (*c*, *d*).

sion of the liquid metal conductor with its own magnetic field, accompanied by local overheating and rarefaction in the melt. Additionally, vortex motion of the molten metal occurs in the channel itself and its outfalls due to MHD effects. The movement of the melt in the MDI bath influences predominantly by purely hydrodynamic effects.

Thus, during the residence time in the MHDU, the liquid alloy is subjected to sequential and multiple thermal and force effects, which, according to the theory of the liquid state of metallic melts, lead to dispersion of microneighbourhood regions within them and subsequently to the refinement of the structural components of solidified alloys [16–19].

In the continuation of the research previously conducted at the Institute for PTIMA NAS of Ukraine [20], it has been demonstrated that thermal&forced MHD processing of liquid aluminium alloys in the MDI can exert a physical impact on the liquid state of the metallic medium, comparable to the effect of modification, but without the use of substances-modifiers. This is manifested in the destruction of areas of microinhomogeneities caused by negative metallurgical inheritance of the charge and the technology of alloy preparation. These effects are further observed in the solid state of the alloy, leading to changes in its structure and primarily the improvement of plastic properties, which are more structurally sensitive characteristics compared to strength indicators. According to previous research conducted on hypo- and hypereutectic silumins, such MHD processing provides a certain increase in strength (up to 15–20%) and a significant increase (up to 2–4 times) in elongation compared to the standard requirements, including international standards, for aluminium alloys obtained through traditional melting technologies, processing, and pouring techniques [12, 21].

In addition, to ensure a high level of purity of the experimental alloy from hydrogen and non-metallic inclusions, a comprehensive refining scheme developed at the PTIMA NAS of Ukraine was applied. The complex t processing in MDI includes argon blowing of the aluminium melt in a controlled atmosphere with simultaneous multiple circulation of the current-carrying liquid metal through a ceramic foam filter installed on one of the outfalls of the induction channel [12, 22, 23]. By implementing this scheme on silumins, the hydrogen content in the processed alloy was significantly reduced to a level of 0.05 $cm^3/100$ g of alloy, which corresponds to the levels achieved during vacuum processing, and it was possible to remove up to 80% of non-metallic inclusions from the alloy.

2.2. Study of the Structure and Mechanical Properties of the Experimental Alloy

After the preparation of the alloy in the MDI, samples were cast from it

to investigate the structure and key mechanical properties. These investigations were carried out using standard techniques. From the obtained alloy, samples were cast into a cast iron mould for mechanical testing and metallographic analysis (Fig. 3, *a*). The cast samples (Fig. 3, *b*) after machining took the form of rods, 230 mm in length and 25 mm in diameter, after removing the excess material. The cooling rate of the solidifying melt did not exceed 10^2 K/s.

A portion of the obtained cast samples underwent mechanical testing using break strength testing method. The remaining samples underwent standard heat treatment, typical for high-strength casting Al–Cu alloys, specifically the T6 heat treatment mode. This process involves quenching (heating up to 545°C, holding for 10–14 hours, and water cooling at 20–100°C) followed by complete artificial aging (heating up to 170°C, holding for 6–10 hours). After the heat treatment, the samples were subjected to mechanical testing and metallographic analysis of their structure using standard accepted methods for such alloys.

2.3. Investigation of the Main Casting Properties of the Experimental Alloy

2.3.1. Study of the Fluidity of the Experimental Alloy

During the development of an experimental analogue of a high-strength casting Al–Cu alloy, it was necessary to achieve the required mechanical properties and a level of technological characteristics for the alloy that would allow the production of cast products. Special attention was given to the study of fluidity and susceptibility to hot cracking in the conducted research. These are the main indicators that directly affect the feasibility and quality of the castings produced.

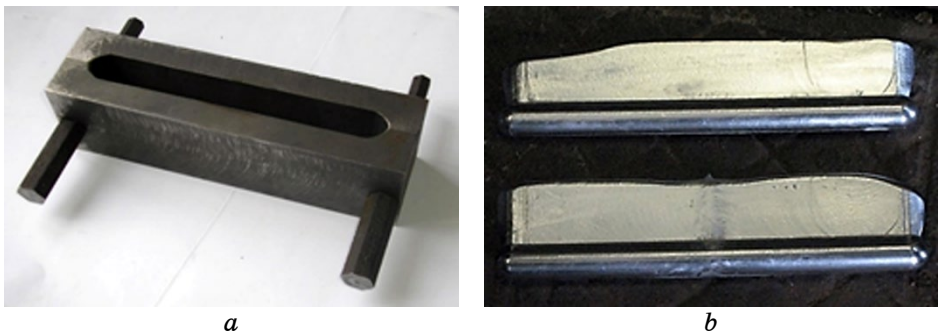

a *b*

Fig. 3. Casting chill mould (*a*) and the cast samples of the alloy with excess material obtained in it (*b*).

a *b*

Fig. 4. Scheme of the U-shaped fluidity test sample (*a*) and the casting chill mould (*b*) for its production.

The study of fluidity utilized a standard U-shaped sample, as shown in Fig. 4, *a*, with the corresponding mould for its production depicted in Fig. 4, *b*. The sample has a channel of constant cross-section with a curved shape, which allows for the evaluation of the alloy's fluidity. Due to the complex configuration of the sample cavity, it is possible to assess qualitatively the alloys' susceptibility to hot cracking.

To determine the fluidity using such test samples, the length of the channel and the cross-sectional area of the mould are selected in a way that the metal, upon solidification, does not completely fill the entire cavity. The fluidity is measured by the length of the obtained rod under specified casting and cooling conditions. During the casting process, the following parameters need to be observed in accordance with the standard:

the temperature of the mould before casting should be $(100 \pm 10)^\circ$C;

the temperature of the melt should exceed the liquidus temperature of the alloy by $(10 \pm 0.5)\%$;

the same hydraulic parameters for casting should be maintained when collecting the entire series of samples.

2.3.2. Study of the Susceptibility of the Experimental Alloy to Hot Cracking during Solidification

The susceptibility of alloys to hot cracking during solidification is a complex property influenced by various parameters, including linear shrinkage and its onset temperature, mechanical properties (strength, ductility and elasticity) of the alloy at high temperatures, rate and nature of solidification, mould compliance, *etc*.

To obtain quantitative assessments of the occurrence of hot cracks

in castings, special samples are used. In the study, a ring-shaped sample (Fig. 5, *a*) was employed. It is a disassembled structure consisting of a bottom plate, a ring for forming the outer part of the cast sample, and a cone that shapes the inner diameter. The plate has a hole for the installation of an internal cone, and has a groove made around it, the diameter of which corresponds to the outer diameter of the ring. Therefore, all the components have a precise positioning on the plate relative to each other, enabling the production of castings with consistent dimensions and the creation of identical conditions for braking linear shrinkage.

However, since identifying the primary cause of hot crack formation is challenging for each specific alloy, the tendency to form defects is determined through a comparative method. For this purpose, another ring-shaped sample was manufactured, having the same outer ring dimensions but an increased cone diameter. By reducing the cross-section of the solid sample, it imposes an additional restriction on linear shrinkage and allows the more accurate detection of defects during casting. Figure 5, *b* illustrates the schematics of the two forms used in

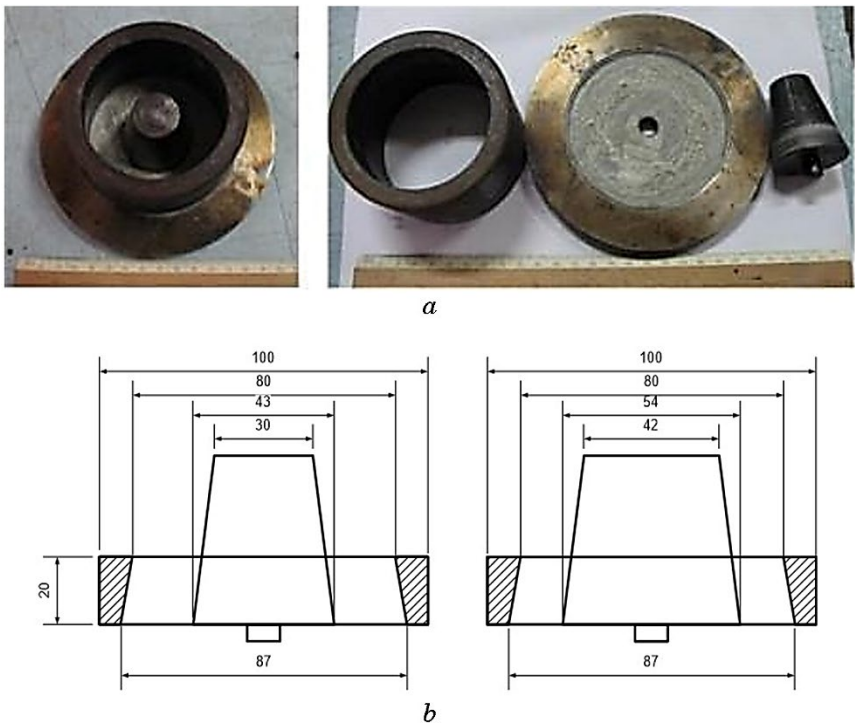

Fig. 5. The ring-shaped samples for assessing hot cracking susceptibility (*a*). Schematics of the two forms of the ring-shaped samples used in the experiments (*b*).

the experiments. The ratio of the cross-sectional areas of the obtained samples is approximately 1:1.5. Figure 5, *b* illustrates the schematics of the two forms used in the experiments. The ratio of the cross-sectional areas of the obtained samples is approximately 1:1.5.

3. RESULTS AND DISCUSSION

Using the MDI, an experimental alloy was prepared, the composition of which, as well as the compositions of analogues alloys, are given in Table 1. The base aluminium melt was initially obtained in a resistance furnace, and then the necessary alloying components, primarily copper and manganese, were introduced into the MDI.

Immediately after the preparation of the initial alloy, samples were poured for the investigation of the structure, basic mechanical, and casting properties (see Figs. 3, 4, 5). Then, the alloy underwent MHD processing in the MDI according to the previously developed regimes for 30 minutes, and corresponding samples were again selected [12]. Subsequently, a comprehensive refining processing of the liquid alloy was carried out for 20 minutes, including argon blowing with simultaneous filtration through a foam ceramic filter under MHD influence, and experimental samples were cast again.

Metallographic examinations and mechanical tests of the produced samples were conducted at the G. V. Kurdyumov Institute for Metal Physics (IMP) of the National Academy of Sciences of Ukraine. It was found that MHD processing of the experimental Al–Cu alloy, which does not contain cadmium and silver, had an effective modifying effect

TABLE 1. Chemical composition of the experimental alloy and its analogues [6].

Alloy	The chemical composition (Al–base), mass %:													
	Cu	Mn	Ti	Cd	Ag	Mg	Ni	Fe	Zn	Si	Zr	Pb	Sn	Cr
Experimental	4.65	0.43	0.19	–	–	0.01	<0.01	0.06	<0.01	0.18	–	–	–	–
AM4.5Kd (GOST 1583-93)	4.50–5.10	0.35–0.80	0.15–0.35	0.07–0.25	–	0.05	–	0.15	0.10	0.20	0.15	–	–	–
A201 (USA)	4.60	0.35	0.15–0.35	–	0.70	0.35	–	<0.15	–	<0.10	–	0.70	–	–
AC1B (Japan)	4.00–5.00	0.10	0.05–0.30	–	–	0.15–0.35	–	0.35	0.10	0.20	–	0.05	0.05	0.05
A-U5GT (France)	4.20–5.00	0.10	0.05–0.30	–	–	0.15–0.35	0.05	0.35	0.10	0.20	–	0.05	0.05	–

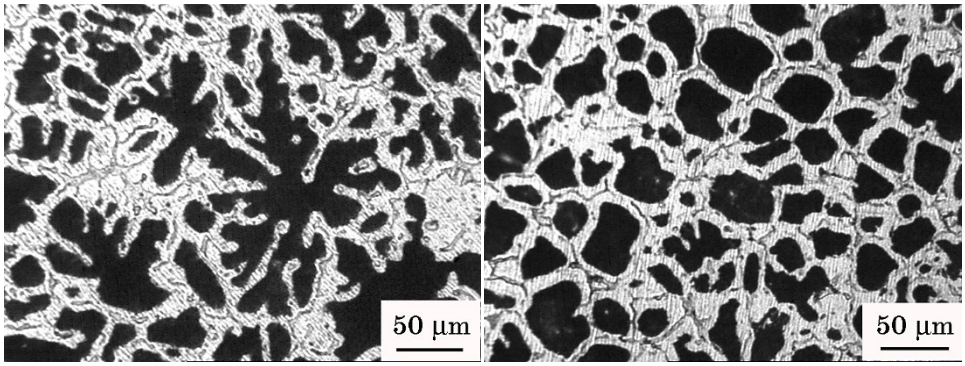

a *b*

Fig. 6. Microstructure of the experimental Al–Cu alloy in the as-cast state: without external processing (*a*); after MHD processing in the MDI (*b*).

on its structure (Fig. 6). In the absence of processing, the alloy exhibits a dendritic structure (Fig. 6, *a*). After MHD processing, the dendrites acquire a cellular structure, almost globular (Fig. 6, *b*).

The research revealed the presence of $CuAl_2$ phase inclusions along the boundaries of globular dendrites, which negatively affect the strength properties. After the conducted heat treatment, these formations transformed into an oversaturated solid solution.

Tests were conducted to determine the main mechanical properties of the experimental alloy and compare them with the values of the alloy analogues (Table 2). It was found that the experimental alloy exhibited higher values of elongation compared to the considered analogues, including those containing toxic and expensive strengthening additives. At the same time, the strength characteristics of the experimental alloy were lower than those characteristics of standard alloys containing cadmium and silver are, but exceeded the properties of analog alloys without these additives.

Further, using the obtained technological samples, the casting

TABLE 2. Key mechanical properties of the experimental Al–Cu alloy and standard analogue alloys after T6 heat treatment.

Alloy	Tensile strength $\sigma_в$, MPa	Elongation δ, %
Experimental alloy	400	10.5
AM4.5Kd (GOST 1583-93)	490	4.0
A201 (USA)	448	8.0
AC1B (Japan)	304	3.0
A-U5GT (France)	340–360	8.0–11.0

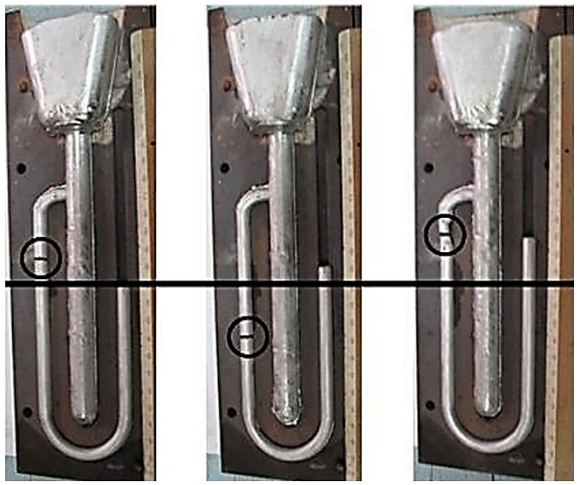

Fig. 7. Fluidity samples of the experimental Al–Cu alloy: in the as-cast state (*a*); after MHD processing in the MDI (*b*); after complex refining and MHD processing in the MDI (*c*).

TABLE 3. Fluidity of the experimental and standard Al–Cu alloys.

Alloy		Fluidity, mm	Density, kg/m^3
Experimental alloy	In the as-cast condition	287	2691
	After MHD processing in the MDI	299	2693
	After complex refining and MHD processing in the MDI	316	2750
AM4.5Kd (GOST 1583-93)		245	2800

properties of the experimental Al–Cu alloy were studied in comparison with the standard AM4.5Kd alloy.

The results of fluidity tests are presented in Fig. 7 and Table 3. It can be observed that the comprehensive and refining MHD processing of the experimental alloy in the MDI allows for improved density and tightness, as well as an increase in fluidity by 10% compared to the initial value (and by 30% compared to the standard AM4.5Kd alloy, which contains toxic cadmium).

As for the investigation of the experimental alloys' susceptibility to hot cracking during solidification, the results of such studies are presented in Fig. 8 and Table 4. It can be seen that the experimental alloy has a narrower solidification range (by 13°C) compared to the standard alloy containing cadmium. This leads to a slight increase in the samples' section before the occurrence of cracks.

a *b*

Fig. 8. Samples for studying the susceptibility of Al–Cu alloys to hot cracking during solidification: experimental alloy (*a*); standard A201 alloy (USA) (*b*).

TABLE 4. Study of the susceptibility of the experimental and standard Al–Cu alloy to hot cracking during solidification.

Alloy	Solidification range, °C	Hot cracking susceptibility (Ring width), mm
Experimental alloy after complex refining and MHD processing in the MDI	642–551	28
AM4.5Kd (GOST 1583-93)	650–548	27.5

4. CONCLUSIONS

In conclusion, the conducted research has established the following.

1. In order to enhance the properties of high-strength casting Al–Cu alloys, expand their applications, reduce production costs, and ensure environmental safety, there is a need for the development of new scientific approaches and technical solutions. This includes the exclusion of toxic (cadmium) and expensive (silver) components from the alloy composition, as well as the utilization of efficient equipment and technologies.

2. The utilization of complex refining processing, electromagnetic field energy, and magnetohydrodynamic effects implemented in magnetodynamic casting installations has facilitated the production of the experimental Al–Cu alloy with increased ductility compared to standard alloys in the same group. The strength characteristics of the experimental alloy only lag behind alloys additionally reinforced with cadmium or silver.

3. The investigation of the casting properties of the experimental alloy has confirmed the potential for manufacturing critical compo-

nents, including thin-walled and complex configuration, from this material. Further research is intended to be carried out in the following directions:
to improve the basic mechanical properties of the alloy to the level of standard high-strength casting Al–Cu alloys, the selection of alloying components that promote the formation of the desired alloy structure needs to be conducted;
due to potential changes in the chemical composition of high-strength alloys, attention should be given to some changing the heat treatment modes of cast products to achieve maximum strengthening effects;
the characteristics of introducing alloying and modifying components into the melt (both in pure form and as part of master alloys) need to be studied, particularly under the impact of electromagnetic effects; if necessary, solutions for obtaining special master alloys should be proposed.

In order to explore the possibility of expanding the application range of the experimental alloy, in-depth investigations into its special, physical, and operational properties are required.

The work is being carried out within the framework of competitive research programs of the National Academy of Sciences of Ukraine.

REFERENCES

1. I. F. Kravchenko, *Visn. Nac. Acad. Nauk Ukr.*, No. 6: 47 (2021) (in Ukrainian).
2. L. Kniewallner, M. Rafetzeder, B. Stauder, M. Djurdjevic, und F. J. Feikus, *Enwicklung und Anwendung einer AlCu basirten Hochleistungsgusslegierung für Zylinderkupfe*, VDI Berichte 2254., Giesstechnik im Motorenbau 2015, Magdeburg, 10–11. February 2015, p. 115.
3. M. Rafetzeder, B. Stauder, M. B. Djurdjevic, L. Kniewallner, und F. J. Feikus, *Potential einer AlCu-basierten Gusslegierung für Hochleistungs-Zylinderkupfe*, 59 Östereichische Giessereitagung, 23/24 April 2015, Leoben, Giesserei Rundschau 62 (2015) Heft 5/6, p. 147.
4. *GOST 1583-93. Casting Aluminium Alloys. Specifications* (in Russian).
5. *Mechanical Engineering: V. II-3: Non-ferrous Metals and Alloys. Composite Metallic Materials* (Ed. I. N. Friedlander) (Moskva: Mechanical Engineering: 2001) (in Russian).
6. E. A. Chernyshov, *Casting Alloys and their Foreign Analogues* (Moskva: Mechanical Engineering: 2006), p. 336 (in Russian).
7. *Conditions Diagrams of Binary Metallic Systems* (Ed. N. P. Lyakishev) (Moskva: Mechanical Engineering: 1996–2000) (in Russian).
8. *Encyclopedia of Aluminum and Its Alloys. Two-Volume Set* (Print) (Eds. George E. Totten, Murat Tiryakioglu, Olaf Kessler) (CRC Press Taylor and Francis Group: 2018).
9. J. M. Silcock and H. M. Flower, *Scripta Materialia*, **46**: 389 (2002).
10. Sanjib Banerjee, P. S. Robi, A. Srinivasan, and Praveen Kumar Lakavath, *Materials and Design*, **31**: 4007 (2010).

11. Laure Bourgeois, Christian Dwyer, Matthew Weyland, Jian-Feng Nie, and Barrington C. Muddle, *Acta Mater.*, **60**: 633 (2012).
12. V. I. Dubodelov, V. Fikssen, M. Slazhniev, M. Goryuk, Yu. Skorobagatko, A. Berezina, T. Monastyrska, O. Davydenko, and V. Spuskanyuk, *Magnetohydrodynamics*, **48**, No. 2: 379 (2012).
13. V. I. Dubodelov, V. N. Fikssen, A. V. Yashenko, N. A. Slazhnev, Yu. P. Skorobagatko, and M. S. Goryuk, *Protsessy Litya*, No. 6: 48 (2013) (in Russian).
14. V. I. Dubodelov, V. N. Fikssen, A. L. Berezina, M. S. Goryuk, T. A. Monastyrskaya, A. V. Yashenko, N. A. Slazhnev, Yu. P. Skorobagatko, and A. V. Kotko, *Protsessy Litya*, No. 4: 62 (2014) (in Russian).
15. V. P. Polishchuk, M. R. Tsin, and R. K. Horn, *Magnetodynamic Pumps for Liquid Metals* (Kiev: Naukova Dumka: 1989) (in Russian).
16. J. R. Morris, *Mater. Trans.*, **48**, No. 7: 1729 (2007).
17. F.-Q. Zu, *Metals*, **5**: 395 (2015).
18. O. S. Roik, O. M. Yakovenko, V. P. Kazimirov, O. O. Bilovodska, N. V. Golovataya, and V. E. Sokol'skii, *J. Molec. Liq.*, 220: 155 (2016).
19. M. Calvo-Dahlborg, P. S. Popel, M. J. Kramer, M. Besser, J. R. Morris, and U. Dahlborg, *J. Alloys Comp.*, **550**: 9 (2013).
20. V. P. Polishchuk and B. A. Melnik, *Liteynoe Proizvodstvo*, No. 7: 6 (1989).
21. A. L. Berezina, T. A. Monastyrskaya, A. A. Davidenko, V. I. Dubodelov, V. Z. Spuskanyuk, and V. N. Fikssen, *Metallofiz. Noveishie Tekhnol.*, **31**, No. 10: 1417 (2009) (in Russian).
22. V. N. Fikssen, *Metallurgiya Mashinostroeniya*, No. 6: 24 (2012) (in Russian).
23. V. N. Fikssen, *Magnetodynamics*, **58**, Nos. 1–2: 151 (2022).

Засновник: Національна академія наук України, Інститут металофізики ім. Г. В. Курдюмова НАН України
Видавець: ВД «Академперіодика» НАН України
Передплатний індекс/Subscription index: 74312 ISSN 1024-1809

Інформація для передплатників журналу
«МЕТАЛОФІЗИКА ТА НОВІТНІ ТЕХНОЛОГІЇ»

Редакція журналу МНТ повідомляє читачів про передплату (що починається з будь-якого місяця випуску). Журнал МНТ входить за індексом **74312** до «Каталогу видань України». Рекомендуємо оформити передплату
1) у відділеннях поштового зв'язку через централізоване аґентство ДПРПВ «ПРЕСА» (вул. Георгія Кирпи, буд. 2[a], 03999 Київ, Україна; телефакси: +380 44 2890774 / 2480377 / 2480384 / 2487802 / 2480406); e-mail: pod_ukr@presa.ua, rozn@presa.ua, info@presa.ua) або
2) через Internet:

http://presa.ua/metallofizika-i-novejshie-tehnologii.html?___SID=U

(передплатний індекс МНТ: 74312) або ж
3) безпосереднім перерахуванням від **170 грн.** за один випуск до **2040 грн.** за один том (12 випусків на рік):
«ОТРИМУВАЧУ»: Інститут металофізики ім. Г. В. Курдюмова НАН України
на розрахунковий рахунок № UA058201720313291001201001901 в банку ГУДКСУ в м. Києві
Код банку: 820172
Код єдиного державного реєстру підприємств і організацій України (ЕДРПОУ): 05417331
Для «ПОСТАЧАЛЬНИКА» — Інституту металофізики ім. Г. В. Курдюмова НАН України
Свідоцтво платника податку на додану вартість (ПДВ) № 36283185, індивідуальний податковий номер (ІПН) 054173326066
Код призначення платежу: 25010100
ПРИЗНАЧЕННЯ ПЛАТЕЖУ: за журнал «Металофізика та новітні технології» (том(и), номер(и), рік(роки)) для РВВ ІМФ НАНУ
ПІДСТАВА: передоплата 100%.

INFORMATION FOR FOREIGN SUBSCRIBERS

Editorial Board of a Monthly Research Journal 'Metallophysics and Advanced Technologies' (transliteration: '**Metallofizika i Noveishie Tekhnologii**') (CODEN: MNTEEU; ISSN: 1024-1809) advertises the subscription on an annual basis. Orders should be placed through one of the methods described below. Besides the subscription *via* the centralized service by State Enterprise 'PRESA' (2[a] Georgiy Kyrpa Str., UA-03999 Kyiv, Ukraine; faxes: +380 44 2890774 / 2480377 / 2480384 / 2487802 / 2480406 / 2487809; e-mail: pod_ukr@presa.ua, rozn@presa.ua, info@presa.ua) or *via* Internet:

http://presa.ua/metallofizika-i-novejshie-tehnologii.html?___SID=U

the Editorial Board will take orders sent directly to the Editorial Board. To obtain our journal, the persons and institutions, interested in this title, should made the definite payment sent, according to the order, to the account of the Publisher—G. V. Kurdyumov Institute for Metal Physics of the N.A.S. of Ukraine.
The journal frequency is 12 issues per year. The annual subscription rate for 'Metallophysics and Advanced Technologies' is 156 USD (or 132 EUR), including airmail postage, packing and handling charges. All other-currency payments should be made using the current conversion rate set by the Publisher (subscribers should contact the Editorial Board).
Subscription is valid after obtaining by the Editorial Board of banker's order. Banker's order should be sent to the address:
G. V. Kurdyumov Institute for Metal Physics, N.A.S. of Ukraine,
currency account No. UA603223130000025308000000067, MFO 322313,
in the Kyiv's Branch of JSC 'The State Export-Import Bank of Ukraine' (Public Joint Stock Company 'Ukreximbank') (11[b] Bulvarno-Kudryavska Str., UA-04053 Kyiv, Ukraine)
simultaneously with written notice providing the Editorial Board with a copy of banker's order for subscription and detailed address for mailing.
Prepayment is 100%.
Address of the Editorial Board: G. V. Kurdyumov Institute for Metal Physics, N.A.S. of Ukraine, 36 Academician Vernadsky Blvd., UA-03142 Kyiv, Ukraine.
E-mail: mfint@imp.kiev.ua (with subject beginning by word 'mfint')
Fax: +380 44 4242561. Phone: +380 44 4249042.
After receiving of banker's order, the Editorial Board will send the guarantee letter to the subscriber's address for mailing the journal for a corresponding term.

The Editorial Board of this journal hopes for effective co-operation with its present and future readers and requests to promote the maximum information about its contents to persons and organizations concerned.